Microwave Cavity Lattices for Quantum Simulation with Photons

Devin Lane Underwood

A Dissertation
Presented to the Faculty
of Princeton University
in Candidacy for the Degree
of Doctor of Philosophy

Recommended for Acceptance
by the Department of
Electrical Engineering
Adviser: Professor Andrew Houck

March 2015

ProQuest LLC.
789 East Eisenhower Parkway
P.O. Box 1346
Ann Arbor, MI 48106 - 1346

Abstract

Historically our understanding of the microscopic world has been impeded by limitations in systems that behave classically. Even today, understanding simple problems in quantum mechanics remains a difficult task both computationally and experimentally. As a means of overcoming these classical limitations, the idea of using a controllable quantum system to simulate a less controllable quantum system has been proposed. This concept is known as quantum simulation and is the origin of the ideas behind quantum computing.

In this thesis, experiments have been conducted that address the feasibility of using devices with a circuit quantum electrodynamics (cQED) architecture as a quantum simulator. In a cQED device, a superconducting qubit is capacitively coupled to a superconducting resonator resulting in coherent quantum behavior of the qubit when it interacts with photons inside the resonator. It has been shown theoretically that by forming a lattice of cQED elements, different quantum phases of photons will exist for different system parameters. In order to realize such a quantum simulator, the necessary experimental foundation must first be developed. Here experimental efforts were focused on addressing two primary issues: 1) designing and fabricating low disorder lattices that are readily available to incorporate superconducting qubits, and 2) developing new measurement tools and techniques that can be used to characterize large lattices, and probe the predicted quantum phases within the lattice.

Three experiments addressing these issues were performed. In the first experiment a Kagome lattice of transmission line resonators was designed and fabricated, and a comprehensive study on the effects of random disorder in the lattice demonstrated that disorder was dependent on the resonator geometry. Subsequently a cryogenic 3-axis scanning stage was developed and the operation of the scanning stage was demonstrated in the final two experiments. The first scanning experiment was conducted on a 49 site Kagome lattice, where a sapphire defect was used to locally perturb

each lattice site. This perturbative scanning probe microscopy provided a means to measure the distribution of photon modes throughout the entire lattice. The second scanning experiment was performed on a single transmission line resonator where a transmon qubit was fabricated on a separate substrate, mounted to the tip of the scanning stage and coupled to the resonator. Here the coupling strength of the qubit to the resonator was mapped out demonstrating strong coupling over a wide scanning range, thus indicating the potential for a scanning qubit to be used as a local quantum probe.

Acknowledgements

Completing a PhD is no easy task, but what they do not tell you at the beginning of graduate school is how much one will rely on the help of others to finish. It goes without saying that my success would not have been possible without the contributions of my teachers, my friends and most importantly my family.

First and foremost, I would like to thank my adviser Professor Andrew Houck. My first interaction with Andrew was during visitation day for new graduate students. He had recently joined the faculty at Princeton, and was still in the process of building his laboratory. At the time I was drawn to Andrew's charismatic personality and his enthusiasm about his research; he inspired me to want to learn more. After the visit day, I emailed Andrew to see if he had any availabilities for summer research assistants, and he responded quickly saying that there was an opening. The next day I mailed in my commitment letter to Princeton.

To me he, has always provided the intellectual support that is necessary to excel in research. I have always admired his intellectual capacity, and it has been an honor to work with such a brilliant scientist. When I would be stressed with a problem, we would have open physics discussions while playing a game of bumper pool. It amazed me that he was capable of understanding and solving difficult problems even before the game would finish. He was an endless fountain of good ideas, but he often encouraged me to pursue my own methods of problem solving. Although I was given the freedom to pursue my own ideas, he always followed my ideas and kept me on track. Andrew's enthusiasm and his passion for new physics have always resonated with me, and those traits are among the most important things I will take with me.

I would like to extend a special thanks to Professor Jens Koch at Northwestern University. It was an honor to get the opportunity to work closely with Jens. He is a patient teacher, a talented writer, and an incredible theoretical physicist. Over the course of five years he has helped me analyze data, he has provided me with a deeper

understanding of my devices, he has been an amazing source for feedback on papers and abstracts, and much of the work in this thesis is a direct result of his influence. Simply put, words cannot do justice for how grateful I am for all your help.

I will never forget the hours spent conducting liquid analysis with Professor Steve Lyon. In fact, I based many of my important decisions in graduate school off of horror stories that were shared during this time. In addition to teaching me what not to do, he was an excellent source for all questions related to experimental physics. To me he was my unofficial advisor. He was always available and enjoyed open discussions about physics. He also provided me with useful career advice. My decision to pursue a position at HRL laboratories is in part due to his advice. Steve's guidance will be missed.

My field of research focused on bridging difficult ideas between condensed matter physics, and quantum optics; however, most of the research focused on ideas developed from quantum optics. Without Professor Hakan Tureci's guidance on this subject, I would have been lost in a sea of incomprehensible journal articles. His enthusiasm for this subject and his availability for discussion have always been a constant source of comfort, and I am honored to refer to him as my teacher.

To the readers of my thesis Professor Claire Gmachl, and Professor Jason Fleischer, they took time out of their busy schedules to read and digest a thesis that was not directly within their realm of expertise. In the end, the feedback they provided has helped to make my thesis more readable and more accessible to a wider audience. Thank you both.

While working in Andrew's lab, I was fortunate enough to get to work with some wonderful postdocs. First and foremost, I would like to recognize Will Shanks. To me Will is more than a colleague: he is a mentor and a friend. His patience with me seemed to be unlimited, and my early success would not have been possible without his guidance. He is one of the most detailed, organized, and thoughtful scientists

I know. Not to mention his abilities for data analysis are second to none. All of Will's work is completed with a very high standard of excellence, and I will always try to meet the standards he set. Darius Sadri was my human Wikipedia source for all physics related questions. I am so fortunate to have been able to work with someone with so much physics knowledge. Our discussions have helped me grow as a physicist, and my only regret is that I was not able to comprehend all the physics he so eloquently described. My time with Anthony Hoffman was limited to the early stages of graduate school, but his dedicated work ethic and his high-intensity approach to research left a lasting impression on me.

Much of Andrew's success is related to his ability to recruit the best graduate students. As a result, I was fortunate to get to work with some of Princeton's brightest minds. Srikanth Srinivasan was the first student in the lab, and together we worked to build the foundation of Andrew's research program. As a lab mate, James Raftery was incredible sounding board. He has an amazing ability to comprehend difficult concepts and simplify them in a way that is both understandable and meaningful. In addition to being an incredible scientist James is a good friend, and I look forward to future APS adventures.

My lab mates Yanbing Liu, and Gengyan Zhang were also strong sounding boards, and I am thankful for all the positive feedback provided over the past few years. From the time Neereja Sundaresan entered the lab as a summer researcher she displayed a sense of curiosity and diligence that have made her into a talented researcher. Her good nature and her dedication to research will take her far. Although, Mattias Fitzpatrick entered into the lab as I was leaving he definitely had a strong impact on me. His never-ending stream of questions and his passion for learning new physics helped to motivate me during challenging times when writing my thesis. I am happy that he will be carrying the torch, and I am confident in the success of this project with him at the reigns.

I was also fortunate to have the opportunity to mentor many bright Princeton undergraduates while working in Andrew's lab. Their energy and endless curiosity were always a source of relief from the stressful grind of graduate school. They are all now graduated and either pursuing graduate degrees, or working successful jobs. I am thankful for Arthur Safira, Alexander Pease, Laszlo Szocs, Momo Ong, and Marius Constantin. As a mentor, I was forced to understand in order to explain.

I would also like to acknowledge my theory collaborator, Andy C.Y. Li from Northwestern University. Our many conversations over the past couple years helped inspire new ideas, and new experiments. Your availability and your helpfulness were very appreciated.

My friends and fellow graduate students outside of the research group were as much responsible for my success and well being as those I worked closely with. To my good friend Ryan Jock, we started the struggle that is graduate school together, and then we shared in many great adventures in this country and many others. More than anybody else Ryan understood my difficulties in graduate school because we went through them together. To my good friend Curt Schieler, we also shared in many great adventures together. Although our research didn't overlap, it was always a valuable exercise to try to describe to him my research. Also his spontaneous distractions, by stopping by to say hello were always well received. As a friend Curt helped to keep me grounded, and I cherish our friendship. Wednesday nights will never be the same without board games.

To Bhadrinariyana Lalgudi Visweswaran (aka Bhadri). He has an amazing ability to understand and simplify difficult concepts, and he was the reason for my success in device physics. More importantly than that, I value our experiences outside of the University. I found his passion for learning about new things and new cultures inspiring, and I always enjoyed experiencing these things with him. With his intelligence coupled with his adventurous personality, he is sure to find success.

To my future sister Loan Le. We first met as fellow students, and then she welcomed me in as family. Over the past few years she has always been a source of encouragement and support when things were challenging. She took time from her schedule to read my thesis, and corrected many hard to find grammatical errors. Not to mention my stomach is forever grateful for the many delicious meals that were so willingly prepared. She has an amazing work ethic, she is a talented researcher, and I know she will be successful in what ever path she chooses. I am so proud to be able to call her my sister. Love you.

I would also like to acknowledge my good friends Ken Nagamatsu, Andrew Shu, Stefan Muenzel, Jimmy Belasco, and Ross Kerner. They helped to make my experiences at Princeton unforgettable.

To the staff that maintain the Micro and Nano fabrication facilities. Their hard work and efforts to keep important equipment maintained and working often go unappreciated. Although with out their efforts I would still be trying to get devices working. Many thanks to Pat Watson, Bert Harrop, Yong Sun, and Joe Palmer.

Finally I would like to thank my family. For many years their support and encouragement has helped to motivate me to pursue my dreams. To my Dad, he never letting me settle when he knew I could do better. To my Mom, her never ending love has always been a comfort during my difficult times. To my sister Dara and her husband Ray, they have always been incredible role models, and I am so proud of the amazing family that they have raised: Alex, Cody, Camden, and Avrie. To my brother Derek, when life had me down, he was always there to support me and lift my spirits.

Last but not least, I would like to thank my future bride Winnie. We met shortly after I arrived at Princeton, and she has been a constant in my life ever since. She is my muse, and a never ending source of positive encouragement in my life. The results in this thesis are as much hers as they are mine. Thank you, and I love you.

"If you can picture it, then you can build it."

Darrell Underwood

For Winnie. With you all things are possible.

Contents

List of Tables

List of Figures

Chapter 1

Introduction

It is common in physics that theoretical proposals precede experimental observations. Oftentimes the observed phenomena is the result of years of work and experimental efforts. A popular example is the recent discovery of the Higgs boson at Cern. The mass particle was predicted to exist by Peter Higgs in 1964 [44], then it took an additional 48 years to develop the technology necessary to observe the existence of the Higgs [19, 20]. Similar to the case of the Higgs Boson the work in this thesis was motivated by theoretical proposals, and arduous experimental efforts are also necessary to observe such phenomena. The calculations in these proposals provide evidence of different quantum phases of light in an array of electromagnetic cavities, where each cavity is coupled to a two-level quantum system. While no quantum phase transitions were observed during the course of this thesis, a great deal has been learned and the necessary framework has been laid for the success of future experiments.

This chapter serves as an introduction to the ideas that have motivated the experimental efforts. To begin, section 1.1 provides an introduction to the concept of a quantum simulator. Subsequently, section 1.2 presents highlighted discussions of the

different platforms for realizing a quantum simulator, and why each of these platforms is unique. Finally, in section 1.3 an over of the rest of the thesis will be presented.

1.1 Quantum Simulation

Figure 1.1: "Nature isn't classical, dammit, and if you want to make a simulation of nature, you'd better make it quantum mechanical, and by golly it's a wonderful problem, because it doesn't look so easy." Richard Feynman, 1982 [30].

Quantum mechanics is a beautiful theory which is capable of describing the microscopic world with incredible accuracy. The theories that formulate modern quantum mechanics are a combined effort of many generations of physicists, all of which started in 1900 with Max Planck's "act of desperation" [83]. As the result of so many great minds it can be argued that the theory of quantum mechanics is one of mankind's greatest scientific developments. For example, many of the luxuries that exist today are a direct result of developments in quantum mechanics, two notable examples being the modern computer, and the laser. Regarding the computer, the advent of quantum mechanics was crucial for the discovery of the device that single-handedly revolutionized computers: the transistor.

Following the development of the transistor, digital computers were soon made with the computational capacity large enough to significantly impact scientific

progress, and yet despite tremendous advances of modern computers, these classical devices are not well suited to tackle problems in quantum mechanics. This was first brought to attention by Feynman, when he showed the difficulty of simulating quantum systems with classical computers. He demonstrated that the computational time of a classical computer for even the simplest states will scale exponentially with the number of particles [30]. For example, a system of N spin 1/2 particles will require 2^N coefficients to be stored in memory, and also a 2^Nx 2^N matrix must be exponentiated in order to compute the time evolution. For systems of large N, this becomes computationally intractable for even the most advanced computers. As an alternative approach, Feynman proposed using a controllable quantum system with comparable degrees of freedom in order to simulate quantum systems that were difficult to model classically, or too complicated to study in a lab setting.

It is worth mentioning that a quantum simulator is not unlike a quantum computer, but the focus of a quantum computer is slightly different than that of a quantum simulator. Most quantum computing research is more focused on solving difficult computational problems by implementing quantum algorithms, rather than simulating difficult problems from physics or chemistry. The best known example of the motivation for quantum computation is Peter Shor's quantum factoring algorithm [96]. Shor's algorithm demonstrated an exponential speedup for factoring large prime numbers. With even the most sophisticated classical algorithms, factoring large prime numbers is a computationally expensive task; "public-key" cryptography based on RSA exploits this fact [86]. While fear of exposing a weakness in RSA has been a motivator for quantum computation, other quantum algorithms, such as Grover's search algorithm [40] have been developed, which further demonstrates the utility of a quantum computer. Although a quantum computer would also have a significant impact in other fields of science, it poses formidable experimental challenges and in the short term a quantum simulator is more amenable to experimental efforts because

it does not require explicit quantum gates or error correction, and less accuracy will be needed [14].

For most current experimental efforts there are two flavors of quantum simulation: an analogue quantum simulator and a digital quantum simulator. In an analogue quantum simulator, a controllable Hamiltonian H_{sim} is engineered and then mapped to the Hamiltonian of a hard-to-study system H_{sys}, and for accurate simulations it is critical that H_{sim} be very similar to H_{sys}. Indeed, due to this constraint, there are many different experimental platforms of analogue quantum simulators because different systems are capable of realizing different Hamiltonians.[11, 9, 5, 47]. Much of the focus for these types of quantum simulators has been guided by simulating many-body quantum systems, which is what Feynman originally envisioned. Despite the development in powerful classical computational methods; such as Monte-Carlo and coupled-cluster methods, density functional theory, dynamical mean-field theory, density matrix renormalization group theory and others, there are still entire classes of problems that cannot be solved by these methods [17]. While it is has not been proven that these problems cannot be simulated by classical means, a quantum simulator could provide a means to develop new models and methods for studying these difficult problems.

A digital quantum simulator is more closely related to a quantum computer, and would be capable of simulating a wider range of Hamiltonians. It is essentially a quantum circuit that is composed of one and two-qubit gates, which could in principle simulate two body interactions. Such a system is well suited for studying time evolution of a Hamiltonian. For example, such a system could be used to obtain the solution to the Schrödinger equation $|\Psi(t)\rangle = e^{-i\hbar H_{sys}t}|\Psi(0)\rangle$ for a time-independent Hamiltonian H_{sys} [14]. The unitary time evolution of H_{sys} can be determined by expanding H_{sys} into a the sum of many local interaction Hamiltonians, known as the

Trotter formula [64]

$$e^{-i\hbar H_{sys}t} \approx \left(e^{-i\hbar H_1 t/n} e^{-i\hbar H_2 t/n} \dots e^{-i\hbar H_l t/n}\right)^n \tag{1.1}$$

where $H_{sys} = \sum_i^l H_i$ is satisfied. The simulation can be made more accurate by taking finer time slices, the equivalent of making n larger. Much like a quantum computer, a digital quantum simulator is going to be more prone to experimental difficulties than an analogue quantum computer, but the long term goal of an all mighty universal quantum simulator is worth the effort.

1.1.1 Criteria for quantum simulation

The requirements to successfully implement a quantum information processor have been defined and are known as the DiVincenzo criteria [26]. In DiVincenzo's paper he enumerated five necessary criteria of a physical system in order to process quantum information more efficiently than a classical computer. More recently a similar set of requirements has been defined for a quantum simulator capable of simulating many-body physics. Given the diversity of quantum simulators, the listed criteria address analogue quantum simulators with the focus of simulating quantum many-body problems [17].

1. **A quantum system.**

   An obvious requirement, nonetheless the system must be composed of a system of bosons or fermions with a large number of degrees of freedom. The particles must be confined to a lattice or a finite region of space in order to initiate particle-particle interactions.

2. **Initialization of the system.**

   In order to understand how a system evolves it must be possible to initialize the system into a known quantum state. The most practical initialization is a

pure state, but initializing into a mixed state would provide a means to study how entanglement propagates in many-body systems [54].

3. **Hamiltonian engineering**

   In order to design a system capable of simulating another system, it must be possible to engineer a distinct set of adjustable interactions between particles. Furthermore, in the spirit of a true quantum simulator, the Hamiltonians that are engineered should not be accessible by classical methods.

4. **Measurement/Detection**

   It must be possible to perform measurements on the system. These measurements could be performed locally or collectively. For example, it is reasonable to address individual sites on a lattice, or the collective state of the particles within the lattice.

5. **Result Verification**

   By definition, there is no direct way to verify the results of a measurement if the system is computationally intractable by classical means. However, it should be possible to develop a comparison for the results by benchmarking the system with solutions of known problems. Presumably new theoretical models could be also developed in order to describe the observed phenomena; the original objective of a quantum simulator.

1.2 Implementations of quantum simulators

There are many different platforms researchers are using in order to implement a quantum simulator. The implementations presented in this section are by no means an exhaustive list. Each platform described in this section is physically unique and is well suited for solving different set of physically difficult problems. Additionally

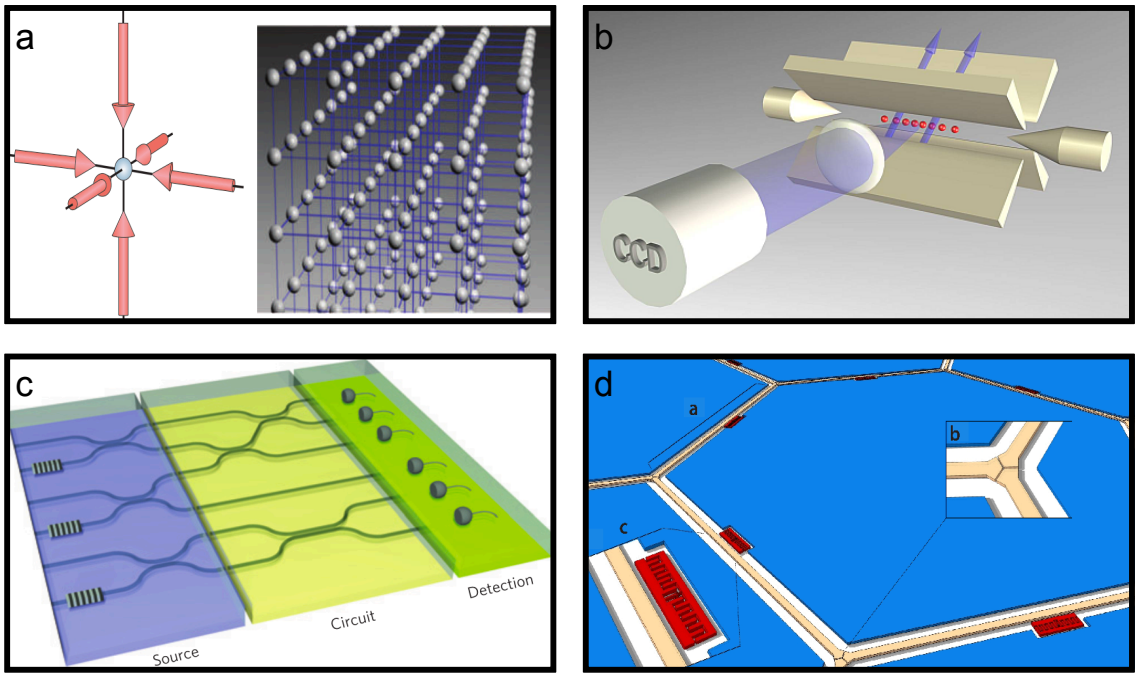

Figure 1.2: Different quantum simulation platforms. **a**, Ultracold atoms trapped in a three dimensional optical lattice [10]. **b**, A linear string of ions confined to a linear Paul trap (Image from quantum optics group at Innsbruck). **c**, Linear optics integrated photonic quantum simulator [5]. **d**, Lattice of superconducting transmission line resonators, each coupled to a transmon qubit [88].

each platform has its own set of advantages and limitations that must be overcome. A major benefit to developing different platforms simultaneously is that results for two different platforms could be compared as a means of verification. This would be ideal as experimental systems start to push the computational limits. Here a physical description of each platforms will be introduced, and followed by a brief discussion of the types of problems these they are designed to solve.

1.2.1 Ultracold quantum gases

While each system is unique and has advantages and disadvantages, it goes without saying that some systems are better suited than others. Of the systems reviewed here, ultracold atomic gases have had the greatest quantum simulation success story [11]. They are naturally well suited because of the implicit quantum nature of single atoms.

Ultracold atomic gases are so rich with physics that different classes of problems can be simulated by modifying the experimental setup or changing type of atomic gas. Two notable examples of the experiments with ultracold atomic gases are: observation of Bose-Einstein condensation [1, 4, 21] and observing a Mott insulator to superfluid phase transition [39]. More recently experiments have been focused on the studying systems of interacting fermions by implementing a fermionic gas [11, 36].

Indeed, there are so many interesting experiments that have been realized that highlighting each is not feasible. For this thesis the experiment of greatest interest is the Mott-insulator to superfluid transition [39]. This quantum phase transition is observed by trapping atoms in periodic potentials of light (figure 1.2), formed by intersecting free-space light [10]. In these optical lattices an onsite interaction energy U between atoms manifests, but is subdued when the nearest neighbor tunneling rate J is small. This system is described very well by the Bose-Hubbard model

$$H = -J \sum_{\langle i\ j \rangle} a_i^\dagger a_j + \frac{1}{2} U \sum_i n_i(n_i - 1) \tag{1.2}$$

where $n_i = a_i^\dagger a_i$ is the number of atoms at the i^{th} site. By tuning the intensity of the lasers forming the optical lattice, the effective tunneling rate J can be adjusted, thereby changing the energy landscape of the system. The competition between U and J will give rise to different quantum phases of the atoms. When $U/J \ll 1$ the atomic wave function spreads homogeneously across the lattice, given by $|\Psi_{SF}\rangle_{U=0} \propto \left(\sum_i^M a_i^\dagger\right)^N |0\rangle$, for M being the number of lattice sites, and N being the total number of atoms, and the ground state of the system is a superfluid. When $U/J \gg 1$ a new ground state is realized in which the number of atoms per site n becomes fixed and does not fluctuate. This is known as a Mott-inuslator and the many body wave function describing this state is the product of Fock states for each lattice site $|\Psi_{SF}\rangle_{J=0} \propto \prod_i^M (a_i^\dagger)^n |0\rangle$. The accuracy at which the experimental system is described

by the Bose-Hubbard model is shockingly good, and is a testament to the utility of ultracold atomic gases for quantum simulation experiments.

1.2.2 Trapped Ions

Conventionally the focus of trapped ion experiments is for development of a quantum information processor. What's more, they are one of the most successful quantum computing platforms. The success of trapped ions is due to the remarkable degree of control of internal and external degrees of freedom of individual ions confined within an electromagnetic trap [9, 52]. Ion control stems from a combination of UV and RF control pulses on the ions while they are trapped inside a larger electromagnetic potential. A common trap is the linear Paul trap as illustrated in figure 1.2. Within the trap the ions can be Doppler cooled to the motional ground state and then controlled with RF pulses [50]. Additionally, the internal states of the ions can be controlled with UV light.

Trapped ions are particularly well suited as a system for studying interacting spin systems. The internal hyperfine levels for a single trapped ion can be used to create an effective spin 1/2. Then by applying an external field, the Coulomb repulsion between adjacent ions will force them away from their equilibrium position. The result is that nearest neighbor ions are forced to interact, thus engineering a spin-spin interaction. By using the motional degrees of freedom to engineer a system of interacting spins ion traps make an ideal candidate for quantum simulation of the quantum Ising model

$$H = \sum_{i<j} J_{i,j}\sigma_i^x\sigma_j^x + B_y \sum_i \sigma_i^y \tag{1.3}$$

where $J_{i,j}$ is the nearest neighbor spin coupling strength, σ^x is the Pauli spin operator, and B_y is the transverse magnetic field. This transverse Ising model is one of the simplest spin models that has been shown to reveal interesting properties of quantum

magnetism. Furthermore, in more than two dimensions the transverse Ising model falls under the class of "NP-complete problems", and is therefore an ideal model for quantum simulation experiments [9, 52, 56, 82].

1.2.3 Photonic systems

One of the most significant features of photons is that they do not easily interact. For this reason photonic systems are both advantageous and disadvantageous. This is an advantage because it means photons are excellent carriers of quantum information, and can travel long distances in either free space or via waveguide. For example, teleportation of entangled photons has been demonstrated between two Canary Islands, a distance of 143 kilometers away [65]. There are many different ways to encode quantum information within a photon: phase, angular momentum, path and polarization; all of which are robust against sources of decoherence, thus making them an ideal candidate for qubits [58]. However for these same reasons it is difficult to generate entanglement between different qubits.

Due to the quantum nature of photons, photonic systems are well suited for quantum simulation, but in contrast to other implementation systems reported, photonic systems are better suited for simulating quantum phenomena of small sized systems [5]. They have already started to have an impact in quantum chemistry calculations which consume a significant amount of supercomputing resources. Notable experiments include: a linear optics setup that has been used to help calculate the properties of a hydrogen molecule with up to 20 digits of precision [63] and an experiment in which a two photon entangled pair was use to simulate frustrated valence-bond states by simulating the ground-state wavefunction of a Heisenberg spin system [66]. For on chip photons, a series of beam splitters can be used to simulate quantum walks of entangled photon pairs [79], and more recently experiments with quantum walks have given rise to topological bound states [57]. The diversity of recent experiments

is a testament to the utility of using photonic systems as an architecture for both quantum simulation and studying quantum information.

1.2.4 Superconducting Circuits

The section touches on the focus of this thesis, realizing a quantum simulator based on a superconducting circuit architecture. These systems are photonic systems, but unlike the photonic systems highlighted in section 1.2.3, here photons can be easily made to interact because of the presence of a nonlinear element; a superconducting qubit. Furthermore the proposed quantum simulators are lattice based quantum simulators where each lattice site is composed of a microwave resonator coupled to a superconducting qubit. The photons within these lattices have been predicted to exhibit interesting quantum phase transitions, such as a Mott insulating to superfluid phase transition[3, 38, 43, 47, 61]. The predicted phase transitions are not unlike the physics observed in ultracold atomic gases trapped in periodic optical lattices described in section 1.2.1; however, systems of interacting photons open a new door to studying these quantum phases because photonic systems are intrinsically open. Making these systems an ideal platform in which to study the physics of non-equilibrium systems [47, 75, 88]. Additionally recent experiments have already demonstrated such non equilibrium behavior by observing a photon number dependent cross-over in a two site lattice [84].

Superconducting circuits are an ideal choice for realizing a lattice based quantum simulator because of significant advances in the field of circuit quantum electrodynamics (cQED), in which a superconducting transmon qubit is capacitively coupled to a transmission line resonator [89]. Much of the success with cQED stems from the easily obtainable strong coupling regime [103], and the fact that cQED devices can be fabricated using standard lithography techniques. These devices are describe very accurately by the Jaynes Cummings Hamiltonian, H_{JC}, which describes fundamental

interactions between photons coupled to a two level atom (section 2.2.1). It is truly remarkable that these macroscopic objects containing billions of atoms can exhibit coherent quantum behavior comparable to that of a single atom. In fact, these systems have such amazing quantum properties, they are now recognized as a leading platform for a quantum information processor.

The aforementioned lattices are a natural extension of these cQED devices because all the same fabrication processes apply, only on a larger scale. The lattices can be describe by what is known as the Jaynes Cummings lattice Hamiltonian, which is simply the sum of single Jaynes Cummings sites plus a coupling Hamiltonian, H^{hop},

$$H^{JCL} = \sum_j H_j^{JC} + H^{hop} - \mu N \tag{1.4}$$

where μN is the energy conserving chemical potential times the number of photons in the system. It is true that a chemical potential implies equilibrium physics, but calculations using this Hamiltonian provide valuable intuition about the behavior of these systems, and was used to predict the different quantum phases of light within the lattice. Also, this Hamiltonian is considered to be valid on timescales faster than loss mechanisms within the lattice. Since these lattices are intrinsically non-equilibrium, it is impossible to completely isolate them from the environment. Although this is not necessarily a limitation because it is possible to engineer quantum reservoirs [72]; paving a new way to study non-equilibrium systems. Whats more, a recent theoretical proposal has outlined a method of experimentally creating a chemical potential of light [41]. Using superconducting circuits as a platform for quantum simulation is still in its early stages, but the rapidly increasing experimental progress in cQED coupled to the abundance of theoretical proposals makes the future of these systems very promising.

1.3 Thesis Overview

The focus of this thesis is the experimental study of a lattice of superconducting transmission line resonators that can be used for a photonic quantum simulator. The significant contributions to this field are the design and fabrication of lattices, and measurement techniques that use a new type of scanning probe microscopy that was developed.

Chapter 2 explores the concept of using a lattice of circuit quantum electrodynamics elements for an analogue quantum simulator. The chapter begins by highlighting some of the important concepts of the fundamental element of these lattices; a superconducting qubit capacitively coupled to a transmission line resonator. The particle of interest in the theoretical proposals is a hybridized photon called a polariton, therefore a brief discussion will be presented about how polaritons are formed. The model used to describe a lattice of cQED sites is the Jaynes Cummings Lattice model. In this chapter it will be presented and discussed in two different limits. Subsequently the primary result from recent theoretical proposals will be presented and discussed; the Mott insulator to superfluid quantum phase transition.

Chapter 3 transitions into the realm of experiment and begins by introducing the concepts of a coplanar waveguide resonator, along with some important microwave engineering techniques that are used to calculate relevant device parameters. Following the introduction of well known microwave techniques, two different circuit analysis approaches to a coplanar waveguide (CPW) resonator will be presented. The first approach is a lumped element analysis and provides an intuitive picture of the CPW resonator near resonance, and the subsequent approach is a distributed element analysis that is used to derive resonator eigenmode frequencies. The distributed element analysis is then extended to lattices of CPW resonators and the interior photon hopping rates and the exterior photon escape rates are derived. Following the derivation

of the hopping rates, a discussion of how a lattice of microwave resonators is designed, fabricated and packaged will be presented.

Chapter 4 introduces the experimental realization of a Kagome lattice of microwave resonators. The chapter begins with a derivation of the band structure for a Kagome lattice beginning with a tight binding hamiltonian. Transport measurements are the primary method measuring lattices. These measurements are discussed, and then a measurement for a lattice consisting of 219 sites is presented and contrasted with the expected band diagram. For successful quantum simulation experiments it is necessary to have low disorder cavity lattices. The effects of disorder were studied in the smallest realizable lattice; the Kagome star. The results from these experiments will be presented, and it will be demonstrated that the effects of disorder are likely due to fluctuations in the kinetic inductance of the coplanar waveguide. Fluctuations in the inductance are shown to be consistent with fluctuations in the device features that result from the fabrication process.

Chapter 5 demonstrates a perturbative scanning probe microscopy method on a 49 site Kagome lattice. This perturbative scanning method allows for imaging the distribution of microwaves within the lattice, and demonstrates the first experimental results of a frustrated flatband within a Kagome lattice. The chapter begins by discussing the experimental setup, and then goes into detail about a characterization experiment conducted to understand the effects of perturbing a superconducting coplanar waveguide resonator. The main result is presented last, and discusses how the different lattice modes are measured and how the analysis is conducted.

Chapter 6 presents results on a scanning transmon qubit experiment; a 'qubit on a stick'. A proof of concept experiment in order to demonstrate the potential of such scanning experiments to be used as a local quantum probe of interior lattice sites within a cQED lattice. Here the main result that is presented is the characterization of the coupling strength between the qubit and the cavity is characterized as a function

of qubit position. A detailed discussion of the experimental techniques and data analysis is also presented.

Chapter 7 begins by making some suggestions for future directions and also some ideas for future experiments. Finally a summary of the work that was completed within this thesis will be presented, along with some closing remarks.

Chapter 2

Circuit QED lattices

2.1 Introduction

A system of interacting photons has generated a great deal of theoretical attention as a potential platform for quantum simulation. While different experimental systems exist in which to realize such a quantum simulator, superconducting circuits are a leading candidate due to the long coherence times, ease of fabrication, potential for scalability, and easily obtainable strong coupling regime. For these reasons, this work has focused on the superconducting circuit architecture, and this chapter serves as a theoretical introduction to the physics associated with a lattice based quantum simulator using the superconducting circuit architecture.

Starting with section 2.2, a presentation will be given on the fundamental building block of these systems; a transmon qubit capacitively coupled to a superconducting transmission line resonator. The success that has resulted from this coupled system has had tremendous impact in quantum information physics. As a result this has developed into a field of physics coined circuit quantum electrodynamics (cQED). There have been many comprehensive studies of this topic published in both journal articles and theses [7, 60, 90, 91], so here only the most relevant topics will be reviewed. The

topics include: an introduction to Jaynes Cummings physics, some relevant regimes that arise when tuning the system parameters of the Jaynes Cummings Hamiltonian, and subsequent discussion on the type of superconducting qubit used within these systems; the transmon qubit.

In section 2.3, a discussion on polaritons will be presented. In all of the theoretical proposals, the particle of interest is the cavity polariton. In much of the literature, it is implied that photons are the particle of interest, and that different quantum phases of photons exist. While this is not entirely false, it is somewhat misleading. The actual particle of interest in these proposals is the polariton, which has both photonic and matter like components that result from interactions with a two level system.

In section 2.4, the model that has been used to describe the proposed quantum simulator will be presented. This model is a a straightforward extension of the Jaynes Cummings hamiltonian presented in 2.2. Subsequent analysis of the lattice model will be presented in sections 2.4.1 and 2.4.2. In these sections different limits within parameters space are considered, and shown to provide significant intuition about the different extremes of the system. Finally in section 2.5, a discussion on the main result from theoretical proposals will be presented. This result is a calculation of the mean field phase diagram, calculated using the hamiltonian presented in section 2.4. This result will be contrasted with similar results from a system of ultracold atoms trapped in optical lattices.

2.2 Circuit quantum electrodynamics

The focus of this work is developing large lattices of superconducting elements, in order to observe the physics of interacting photons; however, before it is possible to make headway on such a complicated subject it is necessary to learn the basics.

With that in mind, the physics of a single site will be presented in order to develop a necessary intuition for designing and understanding the physics of larger systems.

In cQED superconducting circuits are macroscopic objects that are capable of displaying coherent microscopic quantum behavior. For example, a transmission line resonator capacitively coupled to a superconducting qubit behaves analogously to an atom coupled to light in an optical cavity. Remarkably both systems are fundamentally different physically, operate in different energy spectrums, and yet are described very accurately by the Jaynes Cummings Hamiltonian (JCH) . Superconducting circuits are limited to the microwave region of the light spectrum because of the energy gap between normal electrons and Cooper pairs of electrons; excitations of higher energy will destroy the effects of superconductivity and result in destroying the coherent quantum state.

2.2.1 Single site Jaynes Cummings

The Jaynes Cummings Hamiltonian model is the preferred method for describing interactions between light trapped in a cavity and a single atom. It is a well understood, and exactly solvable model that was first introduce in 1963 by Edwin Jaynes and Fred Cummings [51]. It is a simple three part Hamiltonian that describes the fundamental interactions between an atom and the light field $H^{JC} = H_{field} + H_{atom} + H_{int}$. Here the light field is described as a simple harmonic oscillator at energy $\hbar\omega_r$, the atom by a two level system at energy $\hbar\omega_q$ (subscript q for qubit), and with a coupling strength between the light field and the atom as $\hbar g$. The common form of this hamiltonian is given as

$$H^{JC} = \omega_r a^\dagger a + \frac{\omega_q}{2}\sigma^+\sigma^- + g(a^\dagger\sigma^- + a\sigma^+) \tag{2.1}$$

where $\hbar = 1$ (this is the convention for the rest of this thesis), $a^\dagger$ and a are the photon creation and annihilation operators, and σ^+ and σ^- are the Pauli spin operators for a two level system; which act to create and annihilate atomic excitations.

In equation 2.1 the rotating wave approximation was made by ignoring the counter rotating terms $(a^\dagger\sigma^+ + a\sigma^-)$. This is a valid approximation in the limit when $\omega_r \gg g$, as these are not energy conserving terms. These terms correspond to the simultaneous creation or annihilation of an excitation and a photon within an atom and cavity mode; which is not physical in this limit. However, when $\omega_r \propto g$ then the counter rotating terms cannot be ignored, and H^{JC} takes the form of the Rabi model hamiltonian [13]. In the large g limit the system is considered to be in the ultra-strong coupling limit when [73].

2.2.2 Strong coupling limit

A limit well captured by the Jaynes Cummings hamiltonian is known as the resonant strong coupling limit; when $\omega_r \approx \omega_q$. When the resonance condition is met, the allowed energies of the system are hybridized eigenstates separated by $2g\sqrt{n}$, where n is the number of photons inside the cavity (figure 2.1). The anharmonicity afforded by the $\sqrt{n}$ is a result of the quantum two level system inside the cavity. When a system is coupled, excitations coherently oscillate between photons inside the cavity and excitations of the qubit; an effect known as vacuum Rabi oscillations. These oscillations occur at a rate $2g$, and when many oscillations take place before a photon escapes or qubit excitation decoheres the system is said to be in the strongly coupled; which implies $\omega_r > g > \kappa, \gamma$.

For cQED experiments the strong coupling limit is easily obtainable due to the large dipole moment attributed from the macroscopic size of the superconducting circuits. A paper by Devoret et al. [23] provides a beautiful discussion for the physics

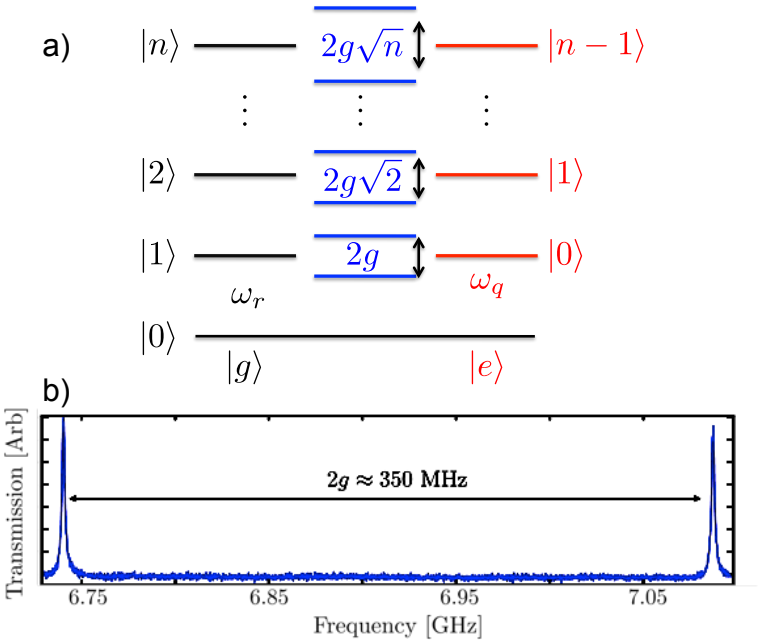

Figure 2.1: **a)**, Energy level diagram for the the resonant strong coupling limit $\omega_r = \omega_q > g > \kappa, \gamma$. The left ladder corresponds to the state of the cavity with the qubit in its ground state $|g\rangle$, and the right ladder corresponds to the qubit in its excited state $|e\rangle$. Each outside rung represents the number of photons $|n\rangle$ inside the cavity, with fewer photons in the cavity when the qubit is excited. When the qubit is in resonance with the cavity, the system hybridizes to form the upper and lower polariton bands $|n, \pm\rangle$. This is the photon number dependent vacuum Rabi splitting, where the separation between the two eigenmodes is related to the number of photons in the cavity $2g\sqrt{n}$. **b)**, An example measurement of the vacuum rabi splitting for a cQED device well into the resonant strong coupling regime.

of the strong coupling limit, and discusses the limitations on capacitive coupling in superconducting circuits.

The system is in the dispersive limit when the qubit and cavity are detuned in energy, $|\omega_r - \omega_q| = \Delta \neq 0$. For quantum information processing it is often preferable to operate within this limit because the qubit will not directly absorb cavity photons [12], furthermore the Purcell effect on the qubit is weaker when the qubit is energetically far away from the cavity [85]. Here the Purcell effect is when the qubit radiatively decays through the cavity rather than emitting a photon back into the cavity; limiting the lifetime of the qubit.

In this limit a perturbative treatment on the hamiltonian can be used when the detuning is greater than the coupling strength $g/\Delta \ll 1$. By expanding the Jaynes Cummings hamiltonian in powers of g^2/Δ that hamiltonian takes the form

$$H^{JC} \approx \omega_r \left(a^\dagger a + \frac{1}{2}\right) + \frac{1}{2}\left(\omega_q + \frac{2g^2}{\Delta}a^\dagger a + \frac{g^2}{\Delta}\right)\sigma_Z \ , \tag{2.2}$$

where σ_Z is the Pauli spin operator for the state of the qubit; which returns ± 1 depending on the qubit state. When dispersively shifted the qubit will not absorb cavity photons, but from this expansion it can be seen that the state of the qubit directly effects the cavity frequency. Two relevant effects can be noticed from this expansion: the photon number dependent Stark shift $g^2/\Delta a^\dagger a$, and the qubit state dependent Lamb shift g^2/Δ. A consequence of these results is that the state of the qubit can be determined by observing the frequency of the cavity. Furthermore, quantum non demolition measurement of the photon number are possible as a result of the photon number dependence in the Stark shift [53].

A particularly interesting regime within the dispersive limit is the strong coupling dispersive regime. This is a narrow range of energies when the dispersive shift is large compared to other decay mechanisms ($g^2/\Delta > \kappa, \gamma$). In this regime the qubit is more strongly coupled and higher order terms must be considered in the expansion

$$H^{JC} \approx H^0 + \frac{g^2}{\Delta}\left(2a^\dagger a + \frac{1}{2}\right)\sigma_Z - \frac{g^4}{\Delta^3}\left(\left(a^\dagger a\right)^2 + 2a^\dagger a + \frac{1}{2}\right)\sigma_Z - \frac{g^4}{\Delta^3}a^\dagger a \ , \tag{2.3}$$

where H^0 represents the hamiltonian for the uncoupled cavity and qubit from equation 2.1. In the second term the dependence on photon number is quadratic, $((a^\dagger a)^2)$, making the dispersive shift of the cavity more sensitive to small changes in photon number (figure 2.2). This nonlinear dependence on photon number is due to the presence of the qubit in the cavity, and gives rise to interacting photon phenomena

that is mediated by the qubit. An example of such phenomena is the photon blockade effect [45].

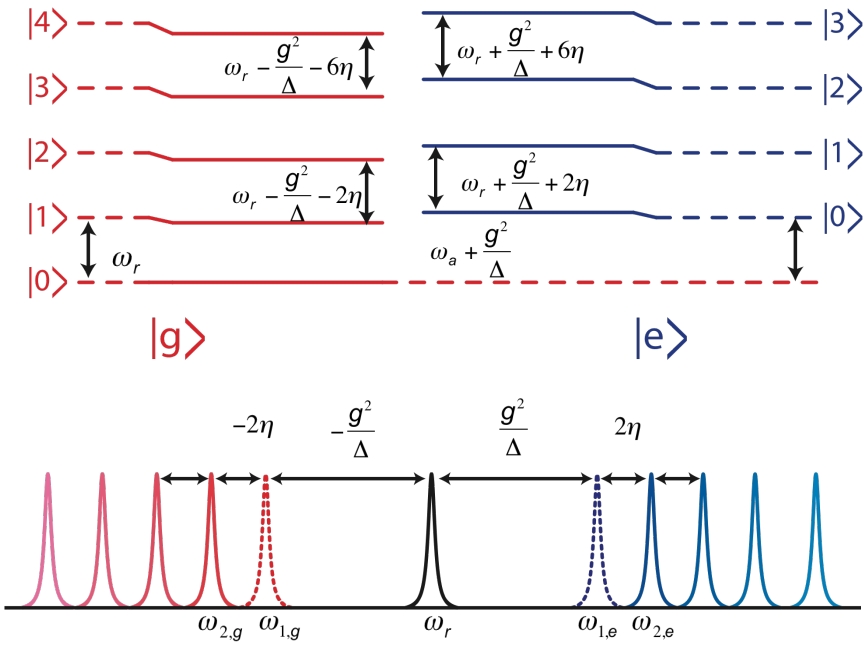

Figure 2.2: A ladder diagram showing the strong dispersive limit $\frac{g^2}{\Delta} > \kappa, \gamma$, and $\frac{g^4}{\Delta^3} > \kappa, \gamma$. The nonlinear dependence on the photon number can be observed in the ladder diagram where the magnitude of the shift increases with photon number n, and the higher order shift $\eta = \frac{g^4}{\Delta^3}$. The lower diagram illustrates how a measured spectrum would be shifted with respect to the photon number dependent dispersive shift. Note that when not in the strong dispersive regime, the nonlinear photon number dependence is small and can be neglected; only the dispersive cavity shift proportional to g^2/Δ is considered.

2.2.3 Loss mechanisms

The aforementioned decay rates κ and γ represent the different loss mechanisms in these circuits. The cavity decay rate κ is determined by the capacitive coupling of the coplanar waveguide resonator to a transmission line at each end of the cavity. For these transmission line resonators, capacitors serve the purpose of semitransparent mirrors, and the decay rate can be engineered in fabrication by varying the size of the capacitance. A more detailed discussion on these cavities and the photon escape rate will be presented in section 3.2.3.

The qubit decay rate $\gamma = \Gamma_1 + \Gamma_2$ is the sum of the different qubit loss mechanisms; the qubit decay $\Gamma_1 = 1/T_1$ and qubit dephasing $\Gamma_2 = 1/T_2$. Here T_1 is often referred to as the excited state lifetime, or relaxation time of a superconducting qubit, and T_2 is the spin dephasing time. Theoretically $T_2 \leq 2T_1$, but for superconducting qubits this has not been the case and measurements have consistently shown $T_2 \leq T_1$. Apart from the limited T_2 measurements, much of the success of superconducting qubits has been due to long coherence times, and in recent years coherence times have seen an almost Moore's law type exponential growth [24]. Removing sources of decoherence constitutes a great deal of effort in superconducting qubit research, and a notable method of increasing T_1 is using a 3-D superconducting cavity; in which coherence times of over 60μs have been observed [78].

2.2.4 The transmon

More than any other qubit, the transmon has impacted the success of cQED. In this work the transmon qubit is the preferred qubit for a lattice based quantum simulator, but since it is not the focus of this research only the main ideas behind the transmon will be presented here. The discussions presented in this section outline results from references [60, 91]. The name stems from *transmission-line shunted plasma oscillation qubit*, and was first proposed by Koch et al. [60], and then experimentally observed a year later by Schreier et al. [90]. A transmon is derived from a cooper pair box (CPB) qubit that falls under a class of qubits called charge qubits; from which the number of cooper pairs ($\hat{n}$) is the good quantum number. The other two classes of qubits are flux qubits, and phase qubits [18], but hard to eliminate sources of decoherence have presented significant challenges for these qubits.

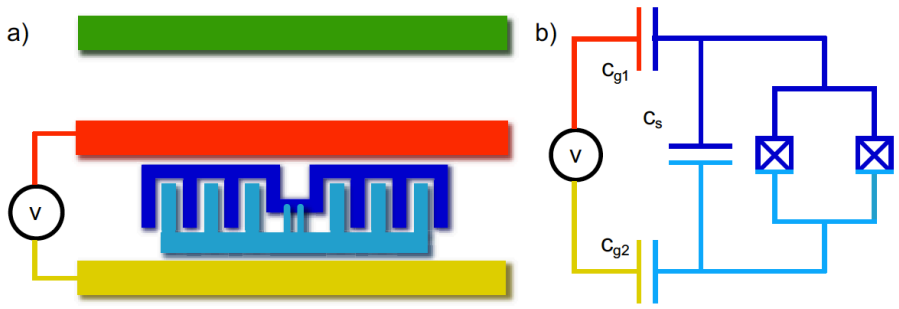

Figure 2.3: **a)** A cartoon illustration of a transmon qubit capacitively coupled to a coplanar waveguide resonator. Here finger capacitors are introduced to the two islands to increase the capacitive coupling and lower E_c. The voltage drop across the trasnmon is related to the number of photons stored within the resonator. **b)** The simplified circuit representation for the transmon qubit. Here C_{g1} is the capacitive coupling to the resonator, C_{g2} is the capacitive coupling to the ground plane, and C_s, is the capacitive coupling between transmon islands. The charging energy is reduced by increasing $C_\Sigma = (C_{g1} + C_{g2} + C_s)$. This figure is from the thesis of David Schuster [91].

For cooper pair box, the hamiltonian is the sum of the electrostatic charging energy E_c and the Josephson energy E_j,

$$H = 4E_c(\hat{n} - n_g)^2 - E_j\cos(\hat{\phi}) \ . \tag{2.4}$$

The charging energy $E_c = e^2/2C_\Sigma$, accounts for the capacitive coupling energy between the two islands. If not for the Josephson tunnel junction, the number of cooper pairs ($\hat{n}$) on each island would be fixed and it would not be possible to change the charge state. The addition of the tunneling barrier allows for cooper pairs to coherently tunnel from one island to another, forming excited charge states. The original cooper pair box operated in a limit where $E_c \approx E_j$, but in this limit it was very sensitive to charge noise, causing fluctuations in the number of excess cooper pairs n_g on the superconducting islands. Early results with the CPB were made possible by operating the qubit in the "sweet spot" (figure 2.4 a), where the the charge dispersion $\partial E_c/\partial n_g \approx 0$, and the spacing between levels is $\approx E_j$.

The transmon is essentially a CPB that operates in a parameter regime where $\mathrm{E}_j \gg \mathrm{E}_c$. This is accomplished by increasing the capacitive coupling between the two superconducting islands. By operating in this different parameter regime, the transmon is made less sensitive to charge dispersion (figure 2.4). In Koch et al. [60], it was shown that the charge dispersion of the m^{th} energy level is exponentially sensitive to the quantity $\sqrt{E_j/E_c}$.

$$\epsilon_m \simeq (-1)^m E_c \frac{2^{4m+5}}{m!}\sqrt{\frac{2}{\pi}}\left(\frac{E_j}{2E_c}\right)^{\frac{m}{2}+\frac{3}{4}} e^{-\sqrt{8E_j/E_c}} \tag{2.5}$$

This exponential sensitivity is the key factor to the success of the transmon, although the cost is the suppression of anharmonicity between levels. However, it turns out that this is not a deal breaker because the anharmonicity decreases linearly for increasing E_j/E_c while charge dispersion decreases exponentially [60]. The absolute anharmonicity is defined as $\alpha = E_{01} - E_{12}$, is observed to be reduced for large values of E_j/E_c.

For a qubit in the transmon regime, unlike the CPB there is no need to operate in a charge "sweet spot", which means that it is much easier to experimentally characterize the qubit. For example the relevant energies E_c and E_j can be obtained from a simple two photon spectroscopy measurement. By monitoring the cavity frequency ω_r with a drive photon, a second photon applied at the transition frequency ω_{01} will cause the cavity frequency to shift resulting in a change in measurement amplitude. Due to the anharmonicity it is also possible to excite the higher transition frequency ω_{12}, in the same way. Using the observed values of ω_{01} and ω_{12} the relevant energies E_c and E_j can be backed out

$$\mathrm{E}_j \approx \hbar\frac{(\omega_{12}-\omega_{01})^2}{8(\omega_{01}-\omega_{12})} \tag{2.6}$$

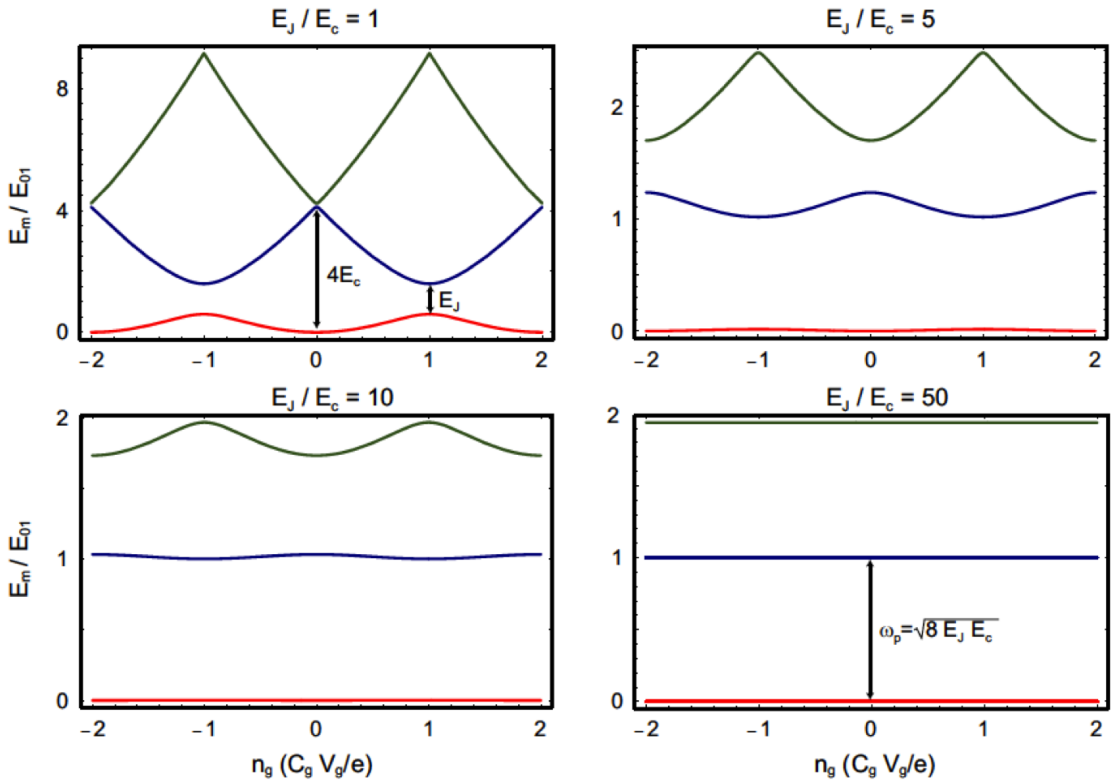

Figure 2.4: Charge dispersion curves for different parameter regimes of the CPB. For ratios of $E_j/E_c > 10$ the sensitivity due to charge noise is significantly reduced and the CPB is considered to be in the transmon regime. Here the anharmonicity is also shown to decrease, but for values of $100 > E_j/E_c > 50$, the absolute anharmonicity is proportional to E_c, as observed in [90]. This figure is from the thesis of David Schuster [91].

$$\mathrm{E}_c \approx -\hbar\alpha \approx \hbar(\omega_{01} - \omega_{12}) \tag{2.7}$$

2.3 Polaritons

A polariton is a boson that manifests from a photon coupled to an electric dipole. When a photon interacts with a dipole it will hybridize to form new energy levels. These new eigenstates are the upper and lower polarition branches, and each branch has both a photonic component and an matter component. Polaritons have been realized many different physical systems, and two notable examples are: surface plasmon

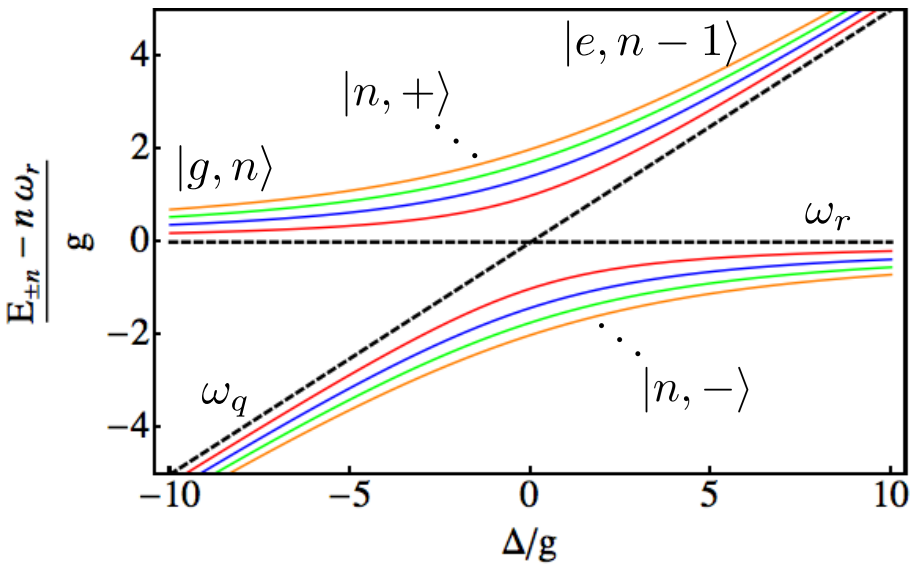

Figure 2.5: The hybridized eigenenergies of the Jaynes Cummings hamiltonian as a function of the detuning, plotted for the first four excitation manifolds. The dashed black line along the equator is the cavity resonance frequency, and the dashed black line along the diagonal is the change in qubit frequency. When $\omega_r = \omega_q$, the system is fully hybridized and the new eigenstates are half photon and half qubit excitation. For increasing or decreasing Δ the hybridization becomes suppressed and the polariton will become more photon in a cavity, or more qubit excitation. For example, when $\Delta > 0$ the upper polariton branch asymptotically approaches a state that is pure qubit excitation, and the lower branch asymptotically approaches a state that is pure cavity photon with the qubit in its ground state.

polaritons [81], and exciton polaritons [22]. Surface plasmons manifest when light is incident on a metal, causing classical excitations of free electrons near the surface of a metal. The field of plasmonics looks to harvest plasmon polaritons using nano fabrication techniques in order to create better waveguides, study near-field optics, and develop new types of sensors [107]. Exciton polaritons are a quantum phenomena and are more closely related to the polaritons of interest in this thesis. The polaritons form when photons are forced to interact with excitons confined within a quantum well. When many excitons exist within the quantum well, many polaritons will form and have been shown to form bose einstein condensates within solids [55].

In cQED the upper and lower polariton branches can be solved for by diagnolizing the JC hamiltonian. One of the most convenient features with the JC hamiltonian is

that only nearest neighbor excitations are connected. As result the hamiltonian can be written in a block diagonal form, which makes the solutions for the n^{th} excitation manifold spanned by $|e, n-1\rangle$ and $|g, n\rangle$ exactly solvable. Explicitly written out, H^{JC} takes the form

$$\begin{pmatrix} (0) & & & & 0 \\ & \begin{pmatrix} \omega_r & g \\ g & (\omega_r + \Delta) \end{pmatrix} & & & \\ & & \begin{pmatrix} 2\omega_r & g\sqrt{2} \\ g\sqrt{2} & (2\omega_r + \Delta) \end{pmatrix} & & \\ & & & \ddots & \\ 0 & & & & \begin{pmatrix} n\omega_r & g\sqrt{n} \\ g\sqrt{n} & (n\omega_r + \Delta) \end{pmatrix} \end{pmatrix} , \tag{2.8}$$

where $\Delta = \omega_q - \omega_r$ is the frequency detuning between the qubit and the resonator. For additional convenience the matrix has been shifted by the vacuum state energy $\omega_r/2$ to make the ground state zero (i.e. $E_{g,0} = 0$). By simply diagnolizing a $2x2$ matrix the exact eigenvalues of the n^{th} sub matrix are

$$E_{n_j\pm} = n_j\omega_r + \frac{\Delta}{2} \pm \sqrt{\left(\frac{\Delta}{2}\right)^2 + n_j g^2} \, . \tag{2.9}$$

which correspond to the allowed energies for the photon number dependent upper and lower polariton branches (figure 2.5). The corresponding eigenstates are referred to as the dressed state solutions and can be solved to give

$$|n, +\rangle = sin\theta_n \, |n, g\rangle + cos\theta_n \, |(n-1), e\rangle \, ,$$

$$|n, -\rangle = cos\theta_n \, |n, g\rangle - sin\theta_n \, |(n-1), e\rangle \, . \tag{2.10}$$

where θ_n is the photon number dependent mixing angle, given as

$$\theta_n = \frac{1}{2} arctan\left(\frac{2g\sqrt{n}}{\Delta}\right) \, . \tag{2.11}$$

These dressed state solutions show that a polariton is indeed a quasi-particle with weight in both of the bare states of the system. They are photon number dependent particles (figure 2.5), and for the photonic component, $|g, n\rangle$, the qubit is in its ground state and there are n photons in the cavity. For the matter component, $|e, (n-1)\rangle$, the qubit is in an excited state, and there is one less photon in the cavity.

2.4 Jaynes cummings lattice

In recent years the Jaynes-Cummings lattice (JCL) model has received a significant amount of theoretical attention as a model for studying strongly correlated many-body systems. Although the JCL model does not directly address the computational challenges associated with quantum many-body systems, it provides a theoretical foundation for developing and realizing a physical system that could be used to simulate quantum many-body problems; i.e. a quantum simulator. This section, and the ensuing subsections present the JCL model, and two limits in which it is analytically solvable. The greater foundation of the subsequent theoretical work follows references [61, 74].

The physical system the JCL model describes is a lattice of photonic cavities where each lattice site is coupled to its own atom (or qubit). Theoretically this simply expressed by a lattice of harmonic oscillators each coupled to its own two-level system. To date, theoretical proposals have considered many different implementations of this model, such as: atoms trapped in optical cavities [3], quantum dots in photonic crystals [38], and the model considered in this thesis; a cQED based architecture where each site consists of a transmission line resonator capacitively coupled to a transmon qubit [47, 61, 74].

The JCL model hamiltonian is ($\hbar = 1$)

$$H^{JC} = \sum_j H_j^{JC} + H^{hop} - \mu N \tag{2.12}$$

where,

$$H_j^{JC} = \omega_r a_j^\dagger a_j + \frac{\omega_q}{2}\sigma_j^+\sigma_j^- + g(a_j^\dagger\sigma_j^- + \sigma_j^+ a_j) \tag{2.13}$$

is the exactly solvable Jaynes Cummings hamiltonian described in section 2.2.1. Here the index j denotes the lattice site that contains the coupled resonator-qubit subsystem, and the part of the hamiltonian that governs the hopping of photons between nearest-neighbor lattice sites is described by

$$H^{hop} = \sum_{\langle i,j\rangle} t_{i,j}\left(a_i^\dagger a_j + a_j^\dagger a_i\right), \tag{2.14}$$

where the hoping rate is $t_{i,j}$. For the rest of this section it is assumed that $t_{i,j} = t$, and in most experimental energy regimes this assumption is correct. In this thesis equation 2.14 has been rigorously studied experimentally, and subsequent sections will discuss the interesting physics associated with this hamiltonian, and how it is engineered with low disorder.

The chemical potential μ in equation 2.12 couples to the total polariton number $N = \sum_j n_j = \sum_j (a_j^\dagger a_j + \sigma_j^+\sigma_j^-)$, and is in accordance with the grand canonical ensemble from statistical mechanics. In the grand canonical ensemble the total number of particles of the system N is allowed to fluctuate with a fixed chemical potential μ, volume V and temperature T, but the mean particle number $\langle N\rangle$ is fixed.

The JCL model presented represents an equilibrium physics model, but the photonic systems of interest are intrinsically non-equilibrium. The inclusion of a chemical potential is an assumption that is not physical because photons are naturally dissipative, and the photon number cannot be conserved. Since the electromagnetic field

of the photon interacts with matter, matter-like excitations will occur and result in absorption; a form of non-radiative decay. Furthermore, photons will naturally escape from the photonic systems as a rate κ.

While the model does not include the physics of dissipation, the equilibrium physics described is expected to exist on timescales much less than the decay mechanisms of the system (i.e κ, γ). Furthermore, a recent theoretical proposal has suggested that it is possible to engineer an artificial chemical potential with the use of a Josephson parametric amplifier [41].

2.4.1 Atomic limit

Unlike the single site JC Hamiltonian, the JCL model does not support exact analytical solutions. It is therefore intuitive to examine the JCL model in the different physical limits [61]. In the atomic limit, the nearest neighbor hopping rate is small compared to the onsite interaction rate ($g \gg t$). To leading order the system becomes decoupled from it's nearest neighbors, and the hamiltonian can then be reduced to the sum of single site JC Hamiltonians offset by the chemical potential.

$$H = \sum_j \left(h_j^{JC} - \mu n_j \right) \tag{2.15}$$

For negligible hopping, excitations will stay in their respective lattice sites, and the resulting ground state wave function can be expressed as a product of states for each individual lattice site $|\Psi\rangle^{\otimes j} = |\Psi\rangle_1 \otimes \cdots \otimes |\Psi\rangle_j$. As a decoupled system each lattice site can be evaluated with the single site JC Hamiltonian. For a fixed polariton number at each site n_j, the system Hamiltonian will become a sum of block diagonal

Hamiltonians of the form.

$$h_j^{JC} = \begin{vmatrix} n_j\omega_r & \sqrt{n_j}g \\ \sqrt{n_j}g & (n_j-1)(\omega_r)+\omega_q \end{vmatrix} \tag{2.16}$$

The resulting energy spectrum for $n \geq 1$ is given as

$$E_{n_j\pm} = n_j\omega_r + \frac{\Delta}{2} \pm \sqrt{\left(\frac{\Delta}{2}\right)^2 + n_j g^2}\,, \tag{2.17}$$

with $E_0 = 0$ for $n = 0$, and qubit resonator detuning given as $\Delta = \omega_q - \omega_r$. It is worth noting, that this is a computationally difficult problem even in the weak hopping/atomic limit. For computations the total size of the Hilbert space will be determined by the size of the lattice and the polariton number n. The single site Hilbert space for the lattice is given as $\mathcal{H}_j = 2^n$ and the total size of the hilbert space becomes $\mathcal{H} = (\mathcal{H}_1 \otimes \cdots \otimes \mathcal{H}_j) = \mathcal{H}_1^{n\times m}$, where m is the number of lattice sites.

The trivial ground state of the system is when $n = 0$, but for non-zero polariton numbers n and a fixed chemical potential μ, the ground state is found by minimizing the single site eigenenergies $E^{\mu}_{n,\pm} = min\{E^{\mu}_0, E^{\mu}_{1,\pm}, \cdots\}$. It is obvious that $E^{\mu}_{n,+} > E^{\mu}_{n,-}$, so this means the ground state will either be the vacuum state $|0\rangle$, or the lower polariton state $|n,-\rangle$.

In the atomic limit, when the polariton number n is an integer number of the lattice sites; the system is expected to be in a state that is analogous to the Mott-insulator from Bose-Hubbard physics [39]. However, by tuning the quantity $(\omega_r - \mu)$ the system reaches a degeneracy point when $E^{\mu}_{n-1,-} = E^{\mu}_{n,-}$; marking the onset of superfluidity. The full set of degeneracy points is given by

$$(\mu - \omega)/g = \sqrt{n + (\Delta/2g)^2} - \sqrt{n + 1 + (\Delta/2g)^2} \tag{2.18}$$

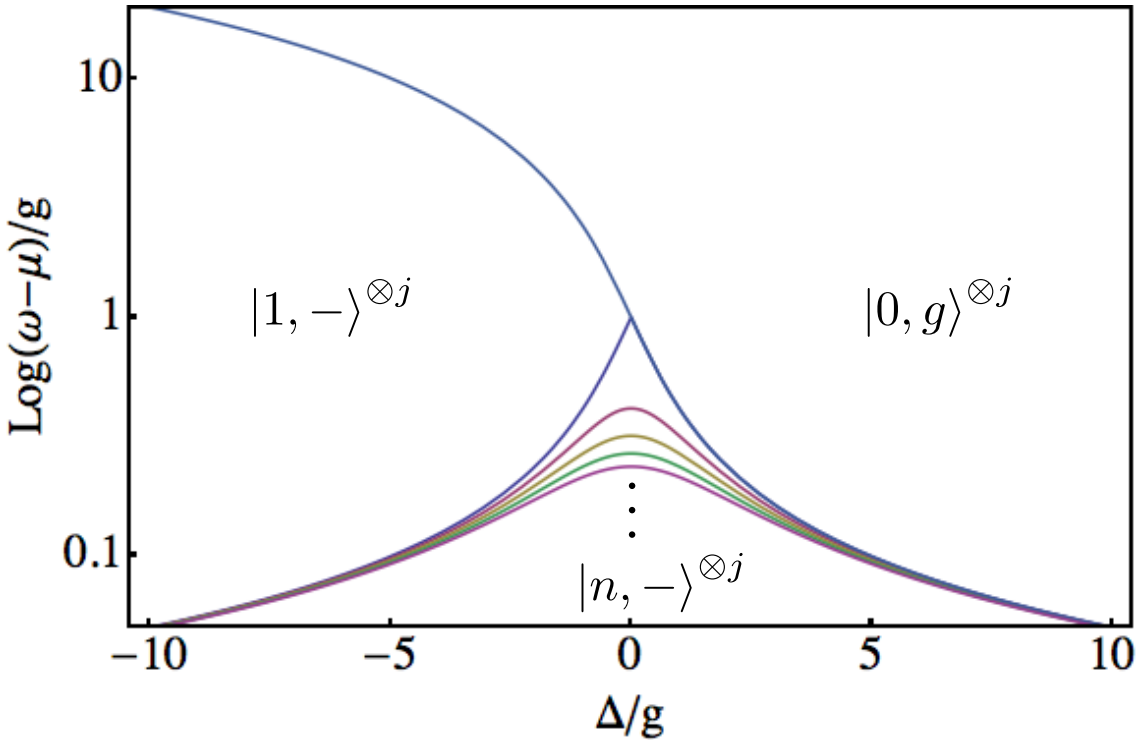

Figure 2.6: Stable ground state solutions for the JCL model in the atomic limit ($g \gg t$). Decreasing the quantity $\mu - \omega$ the system will transition between stable states in which it is energetically favorable to have the same number of polaritons at each site. As the number of polaritons in the system increases (i.e. $\mu - \omega$ decreases), the size of the stable regions shrinks until the system reaches an unstable region when $\mu > \omega$. This is not a stable region because the process of adding more polaritons will effectively lower the total energy of the system, which is not physical.

As seen in figure 2.6 the size of the ground state regions will decrease as the quantity $(\mu - \omega)$ decreases. This implies that the range in parameter space for the atomic limit will get smaller for larger photon numbers.

2.4.2 Hopping limit

This section is meant to examine the ground state in the limit when the nearest neighbor coupling is much larger than the onsite interaction strength $t \gg g$. When the atom-cavity coupling g is very small, it is safe to assume that qubits will remain in their ground state [61]. Consequently when considering the ground state of the system the atomic contribution to the hamiltonian can be ignored and the hamiltonian will

only have a photonic contribution given from the bosonic tight binding hamiltonian

$$H^{TB} = (\omega - \mu) \sum_i a_i^\dagger a_i - t \sum_{\langle i,j \rangle} \left(a_i^\dagger a_j + a_j^\dagger a_i \right). \tag{2.19}$$

This hamiltonian can now be diagnolized in terms of single-particle bloch waves; which is done by Fourier transforming the creation and annihilation operators, and analyzing the momentum space hamiltonian. The result of this treatment will be an expression for the energy dispersion $\epsilon(k)$, and will provide insight to the bosonic ground state of the hopping lattice.

The Fourier transform of the the annihilation operator is given as

$$a_i = \frac{1}{\sqrt{N_s}} \sum_k a_k e^{-(\imath k \cdot r_i)} \tag{2.20}$$

where N_s is the total number of lattice sites, the sum is over all k's in the first Brilloun zone, and the creation operator $a_i^\dagger$ is the hermetian conjugate of a_i. Inserting the annihilation and creation operators the momentum space hamiltonian becomes

$$H^{TB} = \frac{(\omega - \mu)}{N_s} \sum_i \sum_{k,k'} a_k^\dagger a_{k'} e^{-\imath (k-k') \cdot r_i} - \frac{t}{N_s} \sum_{\langle i,j \rangle} \sum_{k,k'} a_k^\dagger a_{k'} e^{-\imath (k \cdot r_i - k' \cdot r_j)}. \tag{2.21}$$

The first term in equation 2.21 yields a delta function in k and k', and the second term can be simplified by introducing a lattice vector G, and considering the lattice geometry. Up until now this has been a general treatment of the hamiltonian. Here I will now consider a 2D square lattice, where the lattice vector is defined as $G = (\pm c, \pm c)$, c is the lattice constant, and using the ansatz $r_j = r_i + G$. Plugging these expressions into equation 2.21 the hamiltonian can be written as

$$H^{TB} = (\omega - \mu) \sum_k a_k^\dagger a_k - \frac{t}{N_s} \sum_i \sum_G \sum_{k,k'} a_k^\dagger a_{k'} e^{-\imath (k-k') \cdot r_i} e^{-\imath (k' \cdot G)}. \tag{2.22}$$

The second term now yields a delta function in k and k', and is summed over all lattice sites; which reduces the hamiltonian to

$$H^{TB} = (\omega - \mu) \sum_k a_k^\dagger a_k - t \sum_G \sum_k a_k^\dagger a_k e^{-\imath(k \cdot G)}. \tag{2.23}$$

Summing over the lattice vector G, yields the dispersion curve as a function of the wave vector k, for the 2D square lattice

$$\epsilon(k) = \left((\omega - \mu) - 2t \sum_i^2 cos(k_i c) \right). \tag{2.24}$$

Although the treatment shown here was for the 2D square lattice, it can easily be extended to other geometries as well. For example the dispersion curve for a honeycomb lattice is given as

$$\epsilon_\pm(k) = (\omega - \mu) \pm t \left| 1 + e^{-ik_x c} + e^{-i(k_x - k_y)c} \right|, \tag{2.25}$$

where the plus and minus signs represent the upper and lower bands of the dispersion curve [61]. Consequently the ground state analysis of the bosonic tight binding hamiltonian is independent of the type of lattice, and due to the this bosonic nature of photons the ground state of the hamiltonian can have N-fold degenerate occupancies in the zero momentum state ($k = 0$). The ground state can be written as

$$E_0 = N(\omega - \mu) - N z_c t, \tag{2.26}$$

where N is the the photon number, and z_c is the lattice coordination number (i.e. the number of nearest neighbors).

There are two insights to be gained from examining this ground state expression. First there are no constraints to the photon number at a single lattice site. This means that the photons can move freely throughout the lattice, which is analogous

to the superfluid phase known from Bose Hubbard physics [39]. Second this ground state presents an instability when $z_c t > \omega - \mu$. As it is not realistic that the ground state energy is negative, this situation is not physical.

2.5 Mott insulator to superfluid phase transition

Phase transitions occur regularly in nature, but are most commonly associated with changes in temperature. These temperature changes cause the properties of a medium to physically change; a very common example would be water transitioning from liquid to solid at $T = 0$ C$^{\text{o}}$, or from liquid to gaseous steam at $T = 100$ C$^{\text{o}}$. A quantum phase transition is a change in the physical system at zero temperature ($T = 0$ K). These transitions can be mediated by an external magnetic field, an external pressure, or another external force that will change the energy of the system without changing the temperature. The major motivation for the research in this thesis was the prediction of a quantum phase transition involving photons. Calculations for a lattice of coupled Jaynes Cummings sites demonstrated that photons within the lattice exhibit two distinct quantum ground states. The two phases are a Mott insulating regime and a superfluid regime. Many recent proposals have shown a transition from one regime to another by tuning the energy ratio g/t [3, 38, 61].

This type of phase transition has been observed for systems described by the Bose-Hubbard model [39], but it is an interesting development to consider a system of photons behaving like a system of atoms. This implies that the same fundamental physics exists in two fundamentally different systems, described by two different hamiltonians; which is the essence of quantum simulation. As such, it is intuitive to first consider this phase transition from the perspective of the Bose-Hubbard model; subsequently results for the lattice of interacting photons will be presented. Also much

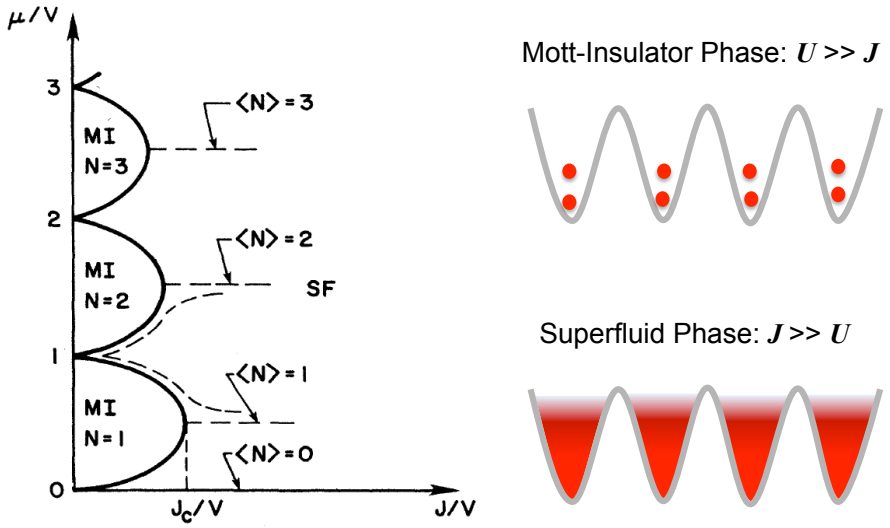

Figure 2.7: The phase diagram calculated by Fisher et al. [31] in the absence of disorder. When J/U is small the system localized with an integer number of bosons at each site. For large J/U, the bosons move freely throughout the lattice.

of the discussion on Bose-Hubbard model is an extension of a previous discussion in section 1.2.1.

The phase diagram describing the Mott insulator to superfluid transition for a system of bosons was first calculated by Fisher et al. [31] (figure 2.7), and it wasn't until 2002 that it was observed in a system of ultra cold atoms trapped in optical lattices by Greiner et al [39]. The phase diagram showed that in different parameter spaces, two physically different systems existed at zero temperature. From this phase diagram a very intuitive picture of the Bose-Hubbard model arises.

$$H = -J \sum_{\langle i\ j \rangle} a_i^\dagger a_j + \frac{1}{2} U \sum_i n_i(n_i - 1) \tag{2.27}$$

where U is the onsite interaction, and J is the nearest neighbor hopping rate. The different phases are a result of the competition between these two energies. In cold atom systems the tunneling rate J is determined by the intensity of the lasers forming the optical lattice, and the different regimes can be observed by adjusting the laser power. When $J/U \gg 1$, the height of the energy potential trapping the bosons at

each site is small, and the wave function of the bosons spreads over the entire lattice. This is known as the superfluid phase. An important distinction of the superfluid phase is that the phase coherence of the bosons is preserved across the entire lattice. The phase-number uncertainty principle ([98]) implies that the phase coherence of the boson gives rise to a large uncertainty the particle number. Accordingly, at any given site the number fluctuates and the variance of the boson number ($\mathrm{Var}(n_i) = \langle n_i \rangle$) forms a Poissonian distribution.

When two neutral atoms in close proximity of one another, a repulsive interaction will result from collisions, also referred to as a contact interaction. This gives rise to the onsite interaction U. It is also worth noting that charged atoms can be used to change the sign of U. For the energy ratio $J/U \ll 1$, the potential trapping the bosons is large compared to the repulsion and quantum fluctuations drive the system into a state where an integer number of bosons are localized at each site. This stable ground state is known as the Mott insulating phase, and is a state in which no phase coherence is prevalent in the lattice. Furthermore each lattice site has the same fixed particle number.

The predicted phase transition of the JCL hamiltonian (equation 2.12) is qualitatively very similar to the phase transition observed from the Bose Hubbard model. For example, analogies can easily be drawn between the atomic limit described in section 2.4.1 and the Mott Insulator phase; as well as the hopping dominated limit discussed in section 2.4.1 and the superfluid phase. In fact it was shown in Koch et al. [61] that the JCL model maps to the Bose Hubbard and an "effective Hubbard U" can be defined as

$$U_{n,\pm} = \left(E^{\mu}_{(n+1)\pm} - E^{\mu}_{n\pm} + \mu \right) / n \tag{2.28}$$

where E^{μ} is the energy in the atomic limit from equation 2.17. For this "effective U" it can be argued that for large polariton number per site, the energy cost of adding extra photons is negligible; which implies the system can no longer be in a localized

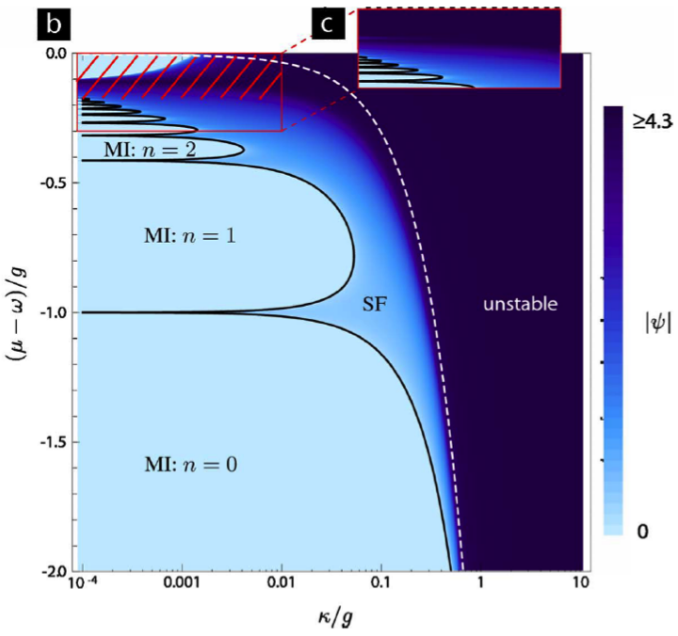

Figure 2.8: Mean field calculation illustrating a Mott insulator to superfluid quantum phase transition in the Jaynes Cummings Lattice [61]. Here $\kappa = t$ is the nearest neighbor photon hopping rate. The light blue region corresponds to Mott insulating state with $\psi = 0$, and and n polaritons per site, which occurs when $g \gg \kappa$. For increasing values of κ, the system will transition into a superfluid phase. In the Mott insulating state the number of polaritons per lattice site will increase for increasing size in the μ, however the size of the Mott lobes in parameter space decreases significantly for increasing μ. For large values of κ the system becomes unstable, as discussed in 2.4.2, because it corresponds to a negative ground state energy. This region is illustrated by a white dotted line. Also it is not realistic to increase the chemical potential $\mu - \omega > 0$, because this corresponds to a negative energy cost per polariton, which is not physical.

regime. This is consistent with results for the Bose Hubbard model describing a gas of non-interacting bosons. Furthermore, without assuming an atomic limit or a hopping limit, a mean field theory calculation using the JCL hamiltonian demonstrated a phase diagram much like the one calculated by Fisher et al. [31] (figure 2.8).

Mean field calculations are commonly used to reduce the computational difficulties of many body calculations [95, 101, 102]. These calculations are an approximation, but the approximation becomes increasingly accurate for an increasing number of dimensions. In order to make this approximation the expectation of the field is generally taken over the nearest neighbor sites, rather than extending across the

entire lattice; effectively decoupling the lattice sites. The general approach for the mean field approximation is to substitute two operators with the expression $a_i^\dagger a_j = \langle a_j^\dagger \rangle a_i + \langle a_j \rangle a_i^\dagger - \langle a_i^\dagger \rangle \langle a_j^\dagger \rangle$. This substitution is made on the hopping hamiltonian (equation 2.14) which gives rise to

$$H^{hop} = t \sum_i \sum_{j \in n.n.(i)} \left(\langle a_j^\dagger \rangle a_i + \langle a_j \rangle a_i^\dagger - \langle a_i^\dagger \rangle \langle a_j^\dagger \rangle \right) , \tag{2.29}$$

where $n.n.(i)$ corresponds to only nearest neighbor sites [38, 61].

Introducing the superfluid order parameter $\psi = zt\langle a_i \rangle$, where z is the coordination number (number of nearest neighbors), the full mean field JCL model can be expressed as $H^{mf} = \sum_i h_i^{mf}$, where

$$h_i^{mf} = H^{JC} - \mu N - (a_i \psi^* + a_i^\dagger \psi) + \frac{1}{zt} |\psi^2| . \tag{2.30}$$

The order parameter is a complex function that is defined as the derivative of the free energy, and is a measure of a systems order as it transitions from one phase to another. The system is considered to be ordered for values of $\psi = 0$, and as seen in figure 2.8, the Mott insulator phase is reached for $\psi = 0$. For increasing values of ψ the system transitions into a superfluid phase.

The mean field calculations have provided an intuitive picture of what is expected, but they do not capture the true nature of these photonic systems. By including a term for the chemical potential μ, these calculations assume an equilibrium picture. While this is not realistic to include a chemical potential, implementing methods used for calculations of open quantum systems is computationally very difficult. It is worth mentioning that efforts are currently being made to engineer a chemical potential by coupling lattice sites to a photonic quantum bath [41].

Chapter 3

Design and fabrication of microwave cavity lattices

3.1 Introduction

The JCL model has been used to produce many theoretically interesting results, but for even the most substantial results the model was simplified beyond what is experimentally achievable. For this reason realizing a quantum simulator based on this model will require significant experimental efforts. The JCL model presented in section 2.4 consists of two significant physical components that must be developed: a lattice of resonators described by a tight binding hamiltonian (equation 2.14), and a lattice of qubits. Due to the nature of the fabrication process it is necessary to fabricate a lattice of resonators prior to including a lattice of qubits. Consequently experimental efforts have followed this systematic approach towards realization and have been focused on a lattice of resonators without qubits.

This chapter will discuss how a lattice of CPW resonators is designed and fabricated. The fundamental building block in these lattices is a transmission line resonator. As such, it is both necessary and intuitive to understand the basic physics of

a single resonator in order to properly design and understand a large lattice of resonators. In section 3.2 the transmission line resonator used for these lattices will be discussed in great detail. The type of transmission line used is a coplanar wave-guide. This chapter begins by discussing equations commonly used amongst microwave engineers for calculating device parameters. Next in section 3.2.2, the effects of a microwave background on a CPW resonator will be presented, and some insight as to how the background arises will discussed.

In subsequent sections two different methods of circuit analysis will be presented in order to gain valuable insight about the intrinsic properties of a CPW resonator. In section 3.2.3 a lumped element method will be used, and shown that when the system is near resonance it is a good approximation for a CPW resonator. Next in section 3.2.4 a distributed element approach is used in order to model a CPW resonator. This analysis shows that the exact eigenmode frequencies for a resonator can be calculated without any assumptions.

Scaling up to larger lattices inevitably requires new methods of analysis. In section 3.3 a distributed element analysis will be presented that extends from methods in section 3.2.4. This analysis provides a means to calculate the rate at which photons hop throughout the lattice and the rate at which photons decay from the lattice. These hopping energies are expressed in terms of device parameters that can be calculated using methods presented in previous sections.

Designing, fabricating, and developing necessary equipment in order to measure these lattices consumed much more time than can be justified in this thesis. In section 3.4.1, some insight into how these complicated microwave structures are designed will be provided. While the experiments in this thesis were conducted for only the empty lattice of resonators, the lattices were design so that transmon qubits could be easily integrated into these lattices. Subsequent sections discuss how these lattices were fabricated (section 3.4.2) and the exhaustive efforts used for connecting ground planes

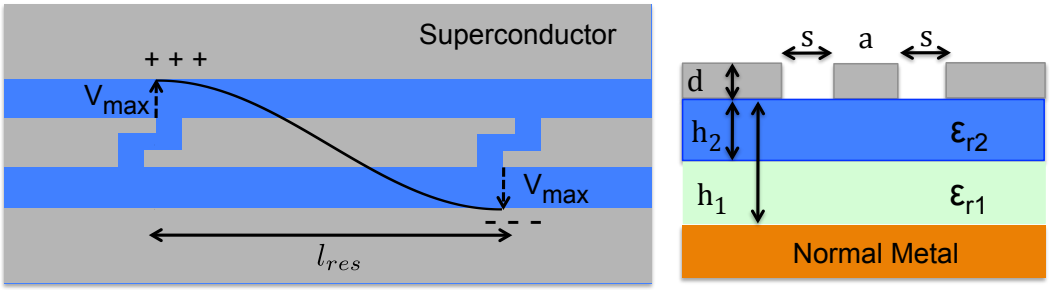

Figure 3.1: A cartoon illustration of a conventional superconducting coplanar waveguide resonator of length l_{res}, with center pin width a, gap width s, fabricated on top of a multi-layer dielectric substrate, mounted to a normal metal surface. Typical cQED devices are fabricated on single-layer dielectric substrates, but the analysis presented for the multilayer can easily be applied a single-layer, in the limit of $h_2 = 0$.

(section 3.5.1). This chapter finishes up by presenting engineering associated with the packaging hardware necessary to measure devices in an electrically and magnetically isolated environment inside of a dilution refrigerator.

3.2 Coplanar waveguide resonators

A conventional coplanar waveguide is composed of three conductors on a dielectric substrate. The two outer conductors are large semi-infinite ground planes and the central conducting strip is separated from the ground planes by a small dielectric (figure 3.1). This can be thought of as a planar version of a coaxial cable capable of supporting a large range of frequencies (kHz - THz) [97]. Typical cQED experiments operate in the microwave frequency spectrum from 4 -10 GHz, which are ideal for CPWs. The excitations inside a CPW propagate inside the central conductor, but the transverse electric field is confined within the gap between the center pin and the ground planes. This confined field is the source of strong coupling in cQED.

3.2.1 CPW properties

In the CPW geometry, resonators can be formed by interrupting the central conductor on either end. The gaps in the center pin form capacitors between the transmission line and the resonator. These two capacitors act as mirrors and allow standing waves to form (figure 3.1). To a good approximation the resonant frequency of the standing wave can be calculated as

$$\omega_{(n-1)} = n\frac{c}{\sqrt{\epsilon_{eff}}\ 2l_{res}}\ , \tag{3.1}$$

where $n > 0$ is the mode number (ω_0 being the fundamental mode), c is the speed of light, ϵ_{eff} is the effective dielectric constant, and l_{res} is the length of conductor between the capacitors. Due to the open boundary conditions formed by the capacitors half a wavelength ($\lambda/2$) resonances are formed. Typical cQED experiments use resonators where the fundamental mode $\omega_r = \omega_0$ falls within the frequency range 4-10 GHz, but cavities can easily be made to harness resonances with higher harmonics by simply making the cavity longer. The higher harmonics are thus integer multiples of the fundamental resonance $\omega_{n-1} = n\omega_0$.

For a conventional CPW all relevant circuit properties can be calculated if the geometry and materials are known. Relevant parameters are the center pin a, the dielectric gap s, and the permmitivity ϵ_r of the dielectric substrate. If these are known, one can calculate the circuit impedance Z_0, the effective dielectric constant ϵ_{eff} of the waveguide and even the attenuation in the line α [97]. Analytical expressions of these circuit properties can be derived using a conformal mapping technique within a quasi-transverse electromagnetic mode (TEM) approximation [15]. This derivation is not presented here. The results from conformal mapping are expressions for the capacitance and inductance per unit length; which can then be used to calculate the desired circuit properties Z_0, and ϵ_{eff}.

Here an example of a typical CPW calculation is presented for a CPW on a multilayer substrate [97]. This example can easily be simplified to single layer substrate for $h_2 = 0$. For this calculation the different dielectric regions are each analyzed separately, therefore partial capacitances for each region can be evaluated. The resulting total capacitance per unit length for a conventional CPW is simply the sum of all partial capacitances in the circuit

$$C_{CPW} = C_1 + C_2 + C_{air} \ . \tag{3.2}$$

The total capacitance for the multilayered substrate (figure 3.1), with partial capacitance regions for the two lower dielectrics C_1 and C_2, and also the partial capacitance in the absence of all dielectrics C_{air}. The partial capacitance for dielectric layer 1 is

$$C_1 = 2\epsilon_0(\epsilon_{r1} - 1)\frac{K(k_1)}{K(k_1')} \tag{3.3}$$

Where $K(k_1)$ and $K(k_1')$ are elliptic integrals of the first kind and the geometric dependence arises from the modulus for these elliptic integrals, k_1 and k_1'

$$k_1 = \frac{\tanh(\frac{\pi s}{4h_1})}{\tanh(\frac{\pi(s+2a)}{4h_1})} \tag{3.4}$$

$$k_1' = \sqrt{1.0 - (k_1)^2} \tag{3.5}$$

where h_1 is the height of the substrate as shown in figure 3.1. These elliptic integrals can easily be numerically evaluated using Matlab (ellipke) or Mathematica (EllipticK). Similarly for dielectric layer 2

$$C_2 = 2\epsilon_0(\epsilon_{r2} - \epsilon_{r1})\frac{K(k_2)}{K(k_2')} \ , \tag{3.6}$$

and

$$k_2 = \frac{\sinh(\frac{\pi s}{4h_2})}{\sinh(\frac{\pi(s+2a)}{4h_2})} \tag{3.7}$$

$$k_2' = \sqrt{1.0 - (k_2)^2} \ , \tag{3.8}$$

where h_2 is the height of the layer (figure 3.1). The different trigonometric functions tanh or sinh in $k_{1,2}$ are determined by the boundary conditions of the dielectric, and arise from the conformal mapping [15]. The tanh function the result of a metal boundary, and the sinh function is the result of a dielectric boundary. Additionally the partial capacitance to air is going to be the sum of partial capacitances for the regions above and below the CPW

$$C_{air} = 2\epsilon_0 \frac{K(k_1)}{K(k_1')} + 2\epsilon_0 \frac{K(k_0)}{K(k_0')} \ , \tag{3.9}$$

where $k_0 = a/(s + 2a)$ is the modulus for an infinitely thick layer of air above the CPW, and k_1 was previously defined.

Given the partial capacitances, the impedance Z_0, and effective dielectric constant ϵ_{eff} can be calculated as

$$Z_0 = \frac{1}{c} \frac{\sqrt{\epsilon_{eff}}}{C_{CPW}} \ , \tag{3.10}$$

where c is the speed of light, and

$$\epsilon_{eff} = \frac{C_{CPW}}{C_{air}} \ . \tag{3.11}$$

The attenuation constant for a CPW can also be calculated as the sum of attenuation due to dielectric losses in the substrate, and also due to conductor losses in the center pin and ground planes. In this thesis only superconductors are used and consequently conductor losses are negligible; however, some loss arises due to defects/asymmetries

in the microwave circuitry due to fabrication [97]

$$\alpha = \frac{\pi}{\lambda_0}\frac{\epsilon_r}{\sqrt{\epsilon_{eff}}} q \tan(\delta_e) \text{ Nepers/meter } . \tag{3.12}$$

Here λ_0 is the free space wavelength in meters, δ_e is the dielectric loss tangent, and q is the filling factor given by

$$q = \frac{1}{2}\frac{K(k_1)}{K(k_1')}\frac{K(k_0')}{K(k_0)} \ , \tag{3.13}$$

this expression assumes a single layer substrate (i.e $h_2 = 0$).

The total inductance per unit length L_{tot} is not necessary for calculations of Z_0 and ϵ_{eff}, because these properties are not dependent on the magnetic properties of the CPW. Although the inductance does contribute to the frequency of the resonator $\omega_0 = 1/2\sqrt{L_{tot}C_{CPW}}l_{res}$, and is an important physical property when considering superconducting circuits. For superconductors the total inductance is going to be the sum of the temperature independent magnetic inductance and temperature dependent kinetic inductance

$$L_{tot} = L_{mag} + L_{kinetic} \ . \tag{3.14}$$

With the magnetic inductance being,

$$L_{mag} = \frac{\mu_0}{4}\frac{K(k_1')}{K(k_1)} \ . \tag{3.15}$$

For normal metals the kinetic inductance can be ignored, but for superconductors it must be considered. For example charged particles traveling thru a wire have inductance because they generate a magnetic field, and according to Lenz's law an opposing magnetic field is induced so as to maintain a constant magnetic field. This is referred to as magnetic inductance. Now in addition to magnetic potential energy the charge particles have some kinetic energy, which is the cause of kinetic inductance. In an AC electric field, the charged particles will oscillate at the frequency of the field,

but the response time of the charged particles will be limited by the inductance. For normal metals the charge particles will scatter off of eachother and off of impurities in the metal, but for superconductors the electron pairs do not scatter, and the kinetic inductance contributes to the response time.

Even for superconductors L_k is small compared to L_m and is usually ignored; however, for CPW resonators L_k is more sensitive to the geometry than L_m, and variations in a result in significant shifts in resonant frequency $\omega_r = 1/2\sqrt{L_{tot}C_{tot}}$. This dependence arises from a geometrical factor where,

$$L_k = \frac{\mu\lambda_L^2(T)}{da} g(a,s,d) \tag{3.16}$$

where μ_o is the permeability in vacuum, λ_L is the temperature dependent magnetic penetration depth, and $g(a,s,d)$ is a geometrical factor derived from the conformal mapping of a CPW [104].

$$g(a,s,t) = \frac{1}{2k^2K(k)^2}\left\{-ln\left(\frac{d}{4a}\right) + \frac{2(a+s)}{(a+2s)}ln\left(\frac{s}{a+s}\right) - \frac{a}{(a+2s)}ln\left(\frac{d}{4(a+2s)}\right)\right\} \tag{3.17}$$

where a,s,d are as seen in figure 3.1. The topic of kinetic inductance will be further discussed in chapter 4.1.

3.2.2 Resonance lineshapes

The most significant characteristic of superconductors is zero resistance at low temperatures. Therefore CPW resonators can be fabricated with remarkably low losses, and photons can be made to bounce back and forth up to a million times before they leave the cavity. This means the loss mechanism of a CPW resonator is determined by defects in the substrate dielectric ϵ_r, impurities in the superconductor, and asym-

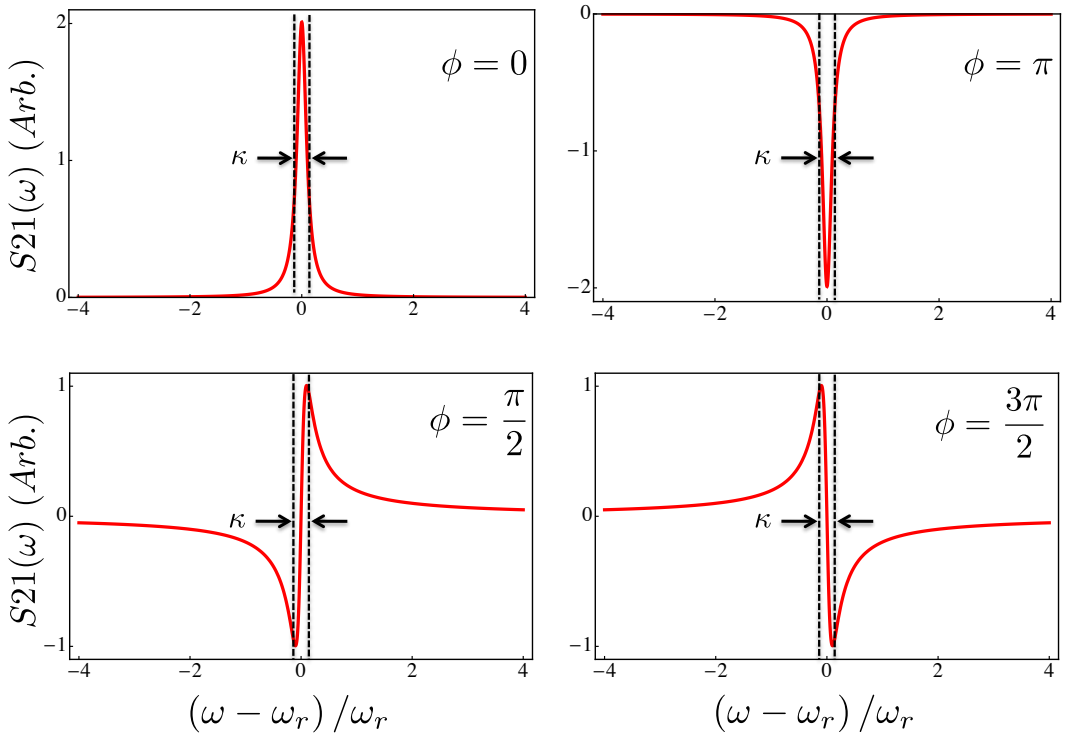

Figure 3.2: Lorentzian line-shapes with background B. The background has been subtracted off for convenience. The FWHM of the line-shape is κ, and is a measurement of the total loss of the resonator. The line shape is determined by the phase of the background ϕ. For backgrounds that are not in phase ($\phi = 0$) with the resonator a Fano resonance is observed. Typically the backgrounds that produce Fano resonances are parasitic modes and can have undesirable consequences. With the exception of ultra high Q devices ($Q \geq 10^6$), the background will have little effect on κ, but can significantly reduce qubit lifetimes T_1 and T_2. The qubit can capacitively couple to the incoherent background modes in the resonator which results in decoherence. Usual suspects for these parasitic modes are slot line modes, box modes, and poorly designed microwave circuitry [105, 46, 34, 16]. Slot line modes are very common and are the most problematic because these resonances or excitations manifest in the ground plane, and can be very difficult to eliminate. There are many sources for slot line modes, to name a few: poorly connected ground planes, badly designed circuit boards, impedance mismatches, and any sort of asymmetries in the microwave circuitry. Basically good microwave hygiene is the best way to eliminate slot line modes. Box modes are the result of resonances inside the sample holder that contains the microwave circuits of interest. Typical means of reducing box modes are brute force numerical calculations to design the sample box so that the resonance spectrum is not within the frequency range of the qubit. Calculations are typically done using software packages such as Ansoft HFSS.

metries in the microwave circuitry. The metric for loss is referred to as the cavity quality factor $Q = \omega_r/\kappa$, which is the ratio of the resonant frequency ω_r to the cavity loss rate κ. The cavity loss rate κ is also equivalent to the full width at half max (FWHM) of a measured spectrum (figure 3.2). For CPW resonators the spectrum follows a Lorentzian line shape of the form ($\omega = 2\pi f$),

$$F_{lor}(\omega) = \frac{A}{1 + \frac{i2}{\kappa}(\omega - \omega_r)} + Be^{-i\phi} \ , \tag{3.18}$$

where A is the amplitude of transmission on resonance, B is the amplitude of the background noise, and ϕ is the phase of the background. This complex function accurately describes a lossy system near resonance, but it is not exactly what is observed from a network analyzer. The square amplitude of this function $S_{21} = |F_{lor}(\omega)|^2$ is what the network analyzer measures, and is what should be used for fitting measured transmission peaks.

3.2.3 Lumped element analysis

Here a pedagogical approach is taken in order to develop an intuition for a CPW resonator. The resonator will be treated as lumped element parallel LCR oscillator that is capacitively coupled to external transmission lines that are modeled with resistors (figure 3.5a). This is a valid treatment for a CPW resonator near resonance ($\omega - \omega_0 \ll 1$) [32]. Subsequent to the lumped element analysis a more precise distributed element analysis will be reviewed.

A simple parallel LCR oscillator will have a loss mechanism that determines the internal "unloaded" quality factor Q_{int} of the resonator. Although in order to measure the LCR oscillator it is necessary to couple to it externally, which contributes to the total quality factor of the system. This "loaded" quality factor Q_L is what is actually

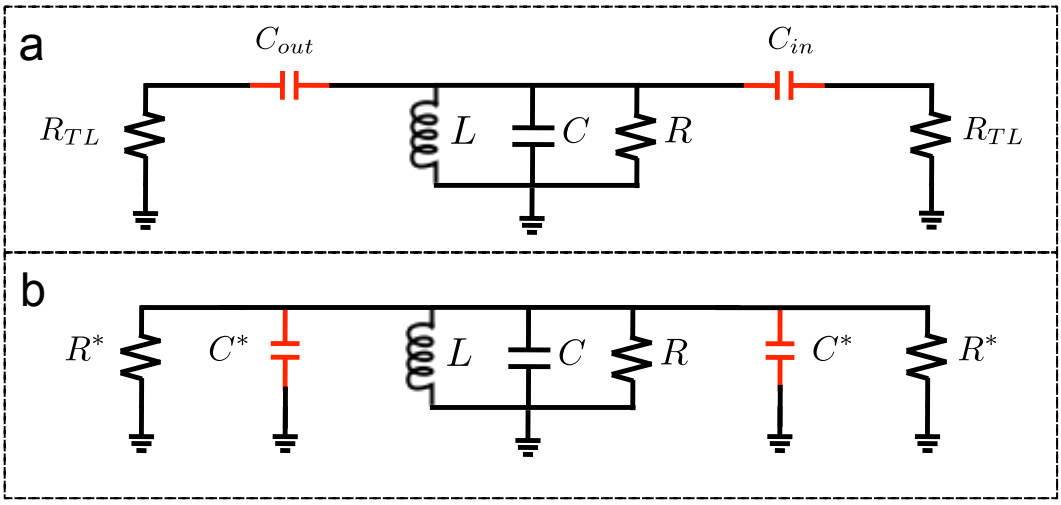

Figure 3.3: Lumped element model of CPW resonator. **a** An LCR oscillator capacitively coupled to transmission lines. The transmission lines are modeled with $R_{TL} = 50\Omega$. **b** Lumped element circuit with the Norton equivalent coupling.

measured, and is given as

$$\frac{1}{Q_L} = \frac{1}{Q_{int}} + \frac{1}{Q_{ext}} \tag{3.19}$$

The internal quality factor can be extracted from the impedance of the parallel LCR oscillator

$$Z_{LCR}(\omega) = \left(\frac{1}{Z_L} + \frac{1}{Z_C} + \frac{1}{Z_R}\right)^{-1} = \left(\frac{1}{j\omega L} + j\omega C + \frac{1}{R}\right)^{-1} . \tag{3.20}$$

This expression can be simplified by examining the oscillator near resonance. On resonance the phase difference across the inductor and the capacitor is zero which requires $Z_L = Z_C$. Using this assumption, and expanding for frequencies near resonance $\omega - \omega_0 << 1$, the impedance can be rewritten as

$$Z_{LCR}(\omega) = \frac{R}{1 + 2jRC(\omega - \omega_0)} , \tag{3.21}$$

which is of the same form as equation 3.18. The characteristic properties of this oscillator are

$$L = \frac{2L_{tot}l_{res}}{n^2\pi^2} \ , \tag{3.22}$$

$$C = \frac{C_{CPW}l_{res}}{2} \ , \tag{3.23}$$

$$R = \frac{Z_0}{\alpha l_{res}} \ , \tag{3.24}$$

therefore, we can define

$$Q_{int} = \omega_0 RC = \frac{RC}{\sqrt{LC}} = \frac{\pi}{2\alpha l_{res}}. \tag{3.25}$$

The LCR oscillator is capacitively coupled to $R_L = 50\Omega$ input/output lines. This coupling will result in capacitive and resistive loading of the resonator which will effect the Q and the resonant frequency. To simplify this analysis one can assume symmetric coupling $C_{in} = C_{out}$ and then transform the series resistor and capacitor into the Norton equivalent parallel connection figure 3.5b. The resulting expressions are

$$R^* = \frac{1 + \omega_n^2 C_{in}^2 R_{TL}^2}{\omega_n^2 C_{in}^2 R_{TL}} \ , \tag{3.26}$$

$$C^* = \frac{C_{in}}{1 + \omega_n^2 C_{in}^2 R_{TL}^2} \ , \tag{3.27}$$

The loaded quality factor for this parallel circuit is going to be the product of the new loaded frequency $\omega_n^* = 1/\sqrt{L(C + 2C^*)}$ and the new loaded RC constant.

$$Q_L = \omega_n^*(C||2C^*)(R||2R^*) = \frac{\omega_n^*}{\kappa} = \omega_n^* \frac{C + 2C^*}{1/R + 2/R^*} \ , \tag{3.28}$$

The expression for κ can be further simplified by considering the coupling capacitors to be small compared to the capacitance of the oscillator $C_{in} \ll C$, which leads to $C + 2C^* \approx C$. The internal loss of the resonator can be assumed to be negligible $R \ll$

R^* (valid for superconductors). Finally plugging in some typical experimental values $\omega_n C_{in} R_L \approx (5 \cdot 10^9)(1 \cdot 10^{-14})(50) = 25 \cdot 10^{-4} \ll 1$, justifies $R^* \approx R_{TL}/\omega_n^2 C_{in}^2 R_{TL}^2$. From these assumptions the simplified form for the cavity decay becomes

$$\kappa = 2\omega_n^3 C_{in}^2 R_{TL} Z_0 \ , \tag{3.29}$$

where $R_{TL} = Z_0 = 50\Omega$. This is a convenient form for the cavity loss rate because the coupling capacitance C_{in} can be calculated numerically using a commercial software package Ansoft Maxwell, and the resonant frequency can be computed from equation 3.1.

3.2.4 Distributed element analysis

A more accurate method method of breaking down a superconducting CPW transmission line is using a distributed element method [59]. Using this method the exact eigenmode frequencies of the resonator can be computed, and in the following sections this method can be used to understand the capacitive coupling between resonators in a lattice.

Here the distributed method breaks down the circuit into infinitesimally small identical LC oscillator circuit elements. In contrast the lumped element method was an example of spatially simplified circuit elements. The distributed model is composed of the sum of inductances ldz and capacitances cdz, where l and c are inductances and capacitances per unit length, and dz is the infinitesimal length scale (figure 3.5). These elements can be evaluated using a Lagrangian in compact matrix notation

$$\mathcal{L}_{tl}(\dot{\vec{\phi}}_{i,n}, \vec{\phi}_{i,n}) = \frac{1}{2}\dot{\vec{\phi}}_i^{\intercal} T_j \dot{\vec{\phi}}_{i,n} - \frac{1}{2}\vec{\phi}_{i,n} V \vec{\phi}_{i,n} \ , \tag{3.30}$$

where T and V are matrices forming the kinetic and potential energy contributions, and $\vec{\phi}^{\intercal} = (\phi_1, \ldots, \phi_N)$ is a vector of spatially dependent field elements inside the

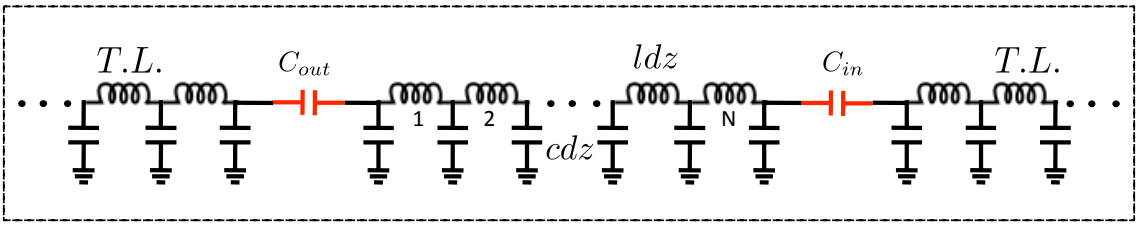

Figure 3.4: **a** Distributed element model of a CPW resonator capacitively coupled to two transmission lines. Here c and l are the inductance and capacitance per unit length, and $C_{in/out}$ is the coupling capacitance to the transmission lines.

transmission line. Consider now a resonator capacitively coupled to transmission lines on either end; the Lagrangian for this resonator can be written precisely as

$$\begin{aligned}\mathcal{L} = &\mathcal{L}'_{TL\ in} + \mathcal{L}'_{TL\ out} + \\ &\frac{1}{2}C_{in}(\dot{\phi}_1 - \dot{\phi}_{in})^2 + \frac{1}{2}C_{out}(\dot{\phi}_N - \dot{\phi}_{out})^2 + \\ &\frac{1}{2}\sum_{i=1}^{N} cdz\dot{\phi}_i^2 - \frac{1}{2ldz}\sum_{i=2}^{N}(\phi_i - \phi_{i-1})^2 \ .\end{aligned} \tag{3.31}$$

For clarification the expression is broken up into three parts: Lagrangians for input and output transmission lines $\mathcal{L}_{in/out}$, contributions to the energy from the capacitive coupling to the resonator $C_{in/out}$, and the kinetic and potential energy contributions for the resonator itself. The capacitive coupling contribution can be further expanded to show: equation 3.32a, the capacitive interaction energy due to capacitive loading, equation 3.32b, the capacitance contribution from the transmission line, and equation 3.32c, the capacitive contribution from the resonator.

$$-C_{in}\dot{\phi}_1\dot{\phi}_{in} - C_{out}\dot{\phi}_N\dot{\phi}_{out} \tag{3.32a}$$

$$C_{in}\frac{1}{2}\dot{\phi}_{in}^2 + C_{out}\frac{1}{2}\dot{\phi}_{out}^2 \tag{3.32b}$$

$$C_{in}\frac{1}{2}\dot{\phi}_1^2 + C_{out}\frac{1}{2}\dot{\phi}_N^2 \tag{3.32c}$$

Recall the purpose of this analysis is to extract resonator mode frequency. From equation 3.31 one can extract kinetic and potential energy matrices T and V for the

resonator contribution;

$$T_{ii'} = \delta_{ii'}(cdz + C_{in}\delta_{i1} + C_{out}\delta_{iN}) \ , \tag{3.33}$$

and

$$V = \frac{1}{ldz}\begin{pmatrix} 1 & -1 & & & & \\ -1 & 2 & -1 & & & \\ & -1 & 2 & -1 & & \\ & & & \ddots & & \\ & & & -1 & 2 & -1 \\ & & & & -1 & 1 \end{pmatrix} \ . \tag{3.34}$$

Typically for a transmission line, the n^{th} eigenmodes are of the form $\vec{\phi} = \eta_n a_n e^{-i\omega_n t}$, and a generalized eigenproblem $Va_n = \omega_n^2 T a_n$ with normalization condition $a_n^{\intercal} T a_\mu = \delta_\mu n$ can be solved to determine the normal modes of the system [59]. This eigenproblem can be difficult to solve, but fortunately it can be simplified because T is easily invertible, and thus $T^{-1}V = \omega_n^2 a_n$. The matrix for this expression becomes

$$T^{-1}V = \frac{1}{lc(dz)^2}\begin{pmatrix} \frac{cdz}{C_{in}+cdz} & -\frac{cdz}{C_{in}+cdz} & & & & \\ -1 & 2 & -1 & & & \\ & -1 & 2 & -1 & & \\ & & & \ddots & & \\ & & & -1 & 2 & -1 \\ & & & & -\frac{cdz}{C_{out}+cdz} & \frac{cdz}{C_{out}+cdz} \end{pmatrix} \ . \tag{3.35}$$

Physically this matrix describes the discrete field ϕ at each infinitesimal section dz inside the resonator. Rows $i = 1$ and $i = N$ describe the field at the capacitive boundaries, and rows $i = 2 \to N-1$ describe the field in the interior of the resonator. First considering interior section of the matrix, the field can be expressed as a discrete laplacian.

$$\frac{\partial^2\phi}{\partial z^2} = \lim_{dz\to 0} \frac{[\phi(z+dz) - \phi(z)] + [\phi(z-dz) - \phi(z)]}{lc\ dz^2} \ , \tag{3.36}$$

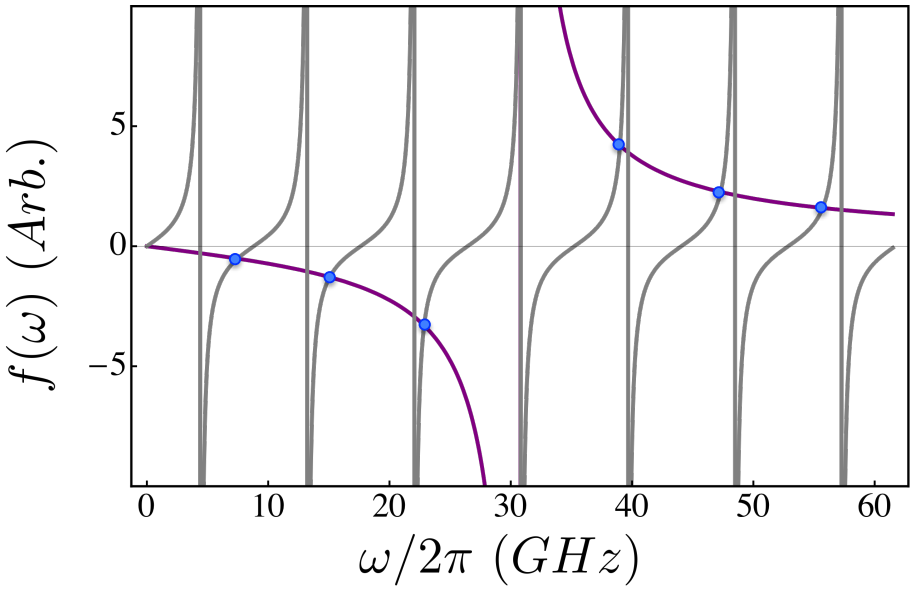

Figure 3.5: Using fabricated devices parameters equation 3.42 was plotted where the blue dots mark the first six exact eigenmode frequencies. Here the fundamental mode is $\omega_0 = 7.4$ GHz. Values for this calculation were for a 50Ω impedance CPW resonator, $l_{res} = 7500\mu m$, l and c were computed using methods from section 3.2.1, and $C_{in} = C_{out} = 18$ fF.

and in the continuous limit one obtains the following wave equation for the mode $\phi_\nu(z)$

$$\frac{d^2\phi_n}{dz^2} = -(\omega_n\sqrt{lc})^2\ \phi_n(z)\ . \tag{3.37}$$

The capacitors at the ends of the resonators form the homogeneous boundary conditions

$$-\left.\frac{d\phi_n}{dz}\right|_{z=0} = \left. lC_{in}\omega_n^2\phi_n\right|_{z=0} \tag{3.38}$$

$$\left.\frac{d\phi_n}{dz}\right|_{z=l_{res}} = \left. lC_{out}\omega_n^2\phi_n\right|_{z=l_{res}} \tag{3.39}$$

Solutions to the wave equation will be sinusoidal functions of the form

$$\phi_n(z) = A\cos(\omega_n\sqrt{lc}z) + B\sin(\omega_n\sqrt{lc}z)\ . \tag{3.40}$$

Using this sinusoidal function in conjunction with boundary conditions ,equation 3.38 and equation 3.39, a system of equations can then be set up to solve for the coefficients A and B.

$$\begin{pmatrix} \eta_{in} & \beta \\ -\beta\sin(\beta l_{res}) - \eta_{out}\cos(\beta l_{res}) & \beta\cos(\beta l_{res}) - \eta_{out}\sin(\beta l_{res}) \end{pmatrix} \begin{pmatrix} A \\ B \end{pmatrix} = 0 \quad (3.41)$$

Where $\beta = \omega_n\sqrt{lc}$, and $\eta_{in/out} = lC_{in/out}\omega_n^2$. Evaluating the determinant of this matrix and doing a little algebra the exact eigenmodes frequencies of the resonator can be given by solutions to the transcendental equation

$$\tan(\bar{\omega}_n) = -\frac{\bar{\omega}_n(\chi_{in} + \chi out)}{1 - \chi_{in}\chi_{out}\bar{\omega}_n^2}, \quad (3.42)$$

where $\bar{\omega}_n = \omega_n\sqrt{lc}l_{res}$ and $\chi_{in/out} = C_{in/out}/(cl_{res})$. The distributed element analysis for this resonator presented has been exact and although it must be solved numerically provides a more accurate calculation of the resonant frequency compared to equation 3.1 because it takes into account the capacitive boundary conditions.

3.3 CPW resonator lattices

Developing a large network of coupled resonators in which transmon qubits can easily be integrated is non-trivial task, with many experimental complications that must be considered during the design process. This section focuses on how to design such a lattice intelligently, and will highlight the experimental concerns that were considered. The first issues that will be addressed are: understanding how photons decay from the lattice, how photons hop throughout the lattice, and how these rates are related to the capacitive coupling. By using a distributed element analysis, a derivation for the lattice decay rate κ and for nearest neighbor photon hopping t will be presented for a lattice of resonators that are capacitively coupled in a honeycomb lattice geometry.

Following the derivation of the hopping rates a discussion of the how the lattice was designed will be presented. This section will discuss how to symmetrically tile CPW resonators equipped with transmon qubits in a honeycomb lattice geometry while trying to conserve the physical size of a large lattice. Additionally, for large lattices, boundary conditions for edge resonators must be considered; these boundary conditions will be discussed.

3.3.1 Photon hopping rates

As shown in a preceding chapter, it is the competition between nearest neighbor photon hopping t and onsite coupling g that will give rise to quantum phase transitions of photons within a lattice. Given this dependence on the photon hopping rate, it is critical to understand how to control and engineer nearest neighbor hopping rates in order to realize a feasible quantum simulator. Here a distributed element approach is used to drive the photon hopping rates for a honeycomb lattice of CPW resonators. In subsequent chapters it will be shown that the photonic realization of the honeycomb lattice is the dual lattice and is referred to as a Kagome lattice. For the rest of the chapter it is presented as a honeycomb lattice because that is what is physically realized and what is considered during the design process.

The lattice model presented here is a continuation of the preceding discussion for a single site (section 3.2.4), and following that formalism from it is straight forward write the total system Lagrangian. It is simply the sum of Lagrangians for single resonator sites, coupling capacitors, and the output transmission lines.

$$\mathcal{L} = \sum_{i=1}^{N} \mathcal{L}_{res,i} + \mathcal{L}_{coupling,i} + \sum_{i=1}^{edge} \mathcal{L}_{T.L.,i} \tag{3.43}$$

Where N is the total number of lattice sites, and for a symmetrically coupled lattice the number of resonators will be the same as the number of coupling elements. The

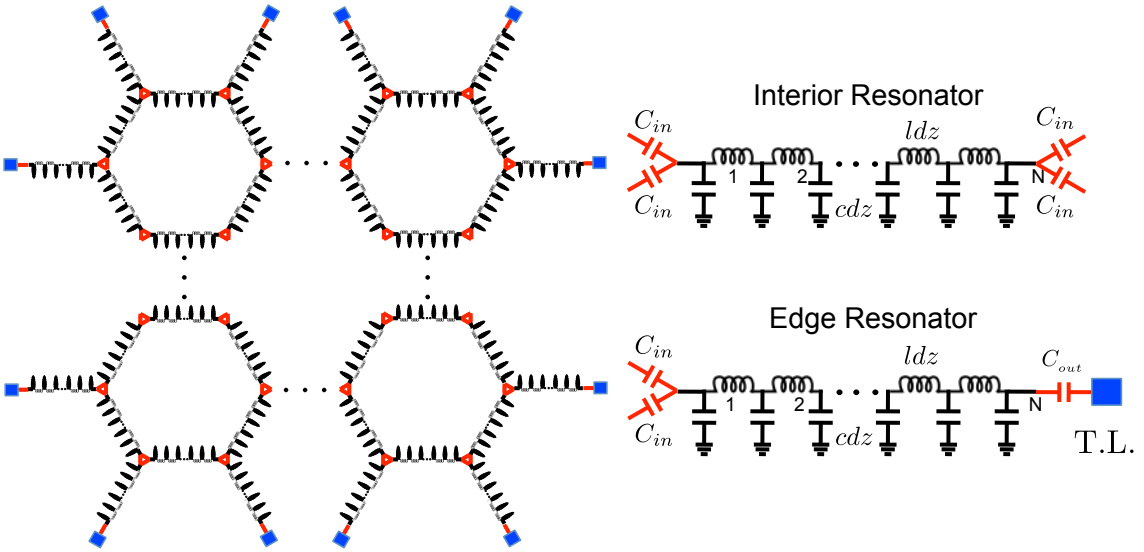

Figure 3.6: A distributed element model (DEM) of the honeycomb lattice of CPW resonators; this model is an extension of the preceding DEM treatment for a single resonator. Here each interior lattice site is symmetrically coupled to four nearest neighbors, and each edge resonator is coupled to two interior resonators and a transmission line. Theoretically it is convenient to consider an infinite lattice; however, experimentally that is not feasible and the edges must be treated. When considering a finite lattice there are two types of resonators that must be considered: interior and edge. With a lattice of these two resonators, there are three types of capacitive boundary conditions: interior to interior set by C_{in}, interior to edge set by C_{in}, and edge to transmission line (TL) set by C_{out}. The blue ports represent transmission lines and for analysis purposes are treated as a continuum of states.

transmission line Lagrangian is only summed over the number of edge resonators. The individual resonator Lagrangians can be expressed as

$$\begin{aligned}\mathcal{L}_{res} = &\sum_{i}^{interior} \frac{1}{2}\dot{\phi}_i^{\intercal} T_{in} \dot{\phi}_i - \frac{1}{2}\phi_i V \phi_i + \\ &\sum_{i}^{edge} \frac{1}{2}\dot{\phi}_i^{\intercal} T_{out} \dot{\phi}_i - \frac{1}{2}\phi_i V \phi_i + \\ &\sum_{i}^{edge} \frac{1}{2}\dot{\psi}_i^{\intercal} T_{T.L.} \dot{\psi}_i - \frac{1}{2}\psi_i V \psi_i\end{aligned} \tag{3.44}$$

where the ϕ_i is the discrete field vector at lattice site i (equation 3.40), and ψ_i is a continuous field afforded by the transmission line. The potential energy matrix V is

the same as equation 3.34. The different boundary conditions arise from the coupling capacitors and are present in the kinetic energy matrix $T_{i,i}$.

$$T_{(i,i')in} = \delta_{i,i'}\left(cdz + 2C_{in}\delta_{i,1} + 2C_{in}\delta_{i,N}\right) \tag{3.45}$$

$$T_{(i,i')out} = \delta_{i,i'}\left(cdz + 2C_{in}\delta_{i,1} + C_{out}\delta_{i,N}\right) \tag{3.46}$$

$$T_{(i,i')T.L.} = \delta_{i,i'}\left(cdz + C_{out}\delta_{j,N}\right) \tag{3.47}$$

The delta functions fix the boundary conditions at the ends of the resonators, where the indices represent the position of the field along the resonator (figure 3.6). Each interior resonator has two nearest neighbors on either end, so each capacitive energy term has a factor of two not present in the previous analysis. Edge resonators are each coupled to two interior resonators, and to a transmission line by C_{out}.

Each lattice site exchanges energy by capacitively coupling the fields from nearest neighbor sites ϕ_i and ϕ_i'. The coupling Lagrangian in equation 3.43 takes into account the energy exchange with three different capacitive coupling terms: inner-inner, inner-outer, and outer-transmission line. The coupling Lagrangian is of the form,

$$\begin{aligned}\mathcal{L}_{coupling} = &- C_{in}\sum_{<i,i'>}^{interior}\dot{\phi}_i\dot{\phi}_{i'} \\ &- C_{in}\sum_{<i,i'>}^{edge}\left(\dot{\phi}_i\dot{\phi}_{i'} + \dot{\phi}_i\dot{\phi}_{i'}\right) \\ &- C_{out}\sum_{<i,i'>}^{edge}\dot{\phi}_i\dot{\psi}_{i'}\ .\end{aligned} \tag{3.48}$$

To extract the photon hopping rates it is convenient to switch from the Lagrangian picture to the Hamiltonian picture. This transition can be made easier by considering the generalized eigenproblem $Va_n = \omega_n^2 Ta_n$ (section 3.2.4) and expressing the field operators in terms of eigenmodes $\phi_i \to \sum_n \xi_{i,n}\varphi_{i,n}(z)$ and $\psi_i \to \sum_n \zeta_{i,n}\tilde{\varphi}_{i,n}(z)$, where

n is the mode number. The resulting resonator Lagrangian can be written as

$$\mathcal{L}_{res} = \overbrace{\sum_{i=1}^{N}\sum_{n}\left(\dot{\xi}_{i,n}^2 - \frac{1}{2}\omega_{i,n}^2\xi_{i,n}^2\right)}^{resonators} + \overbrace{\sum_{i=1}^{edge}\sum_{n}\left(\dot{\zeta}_{i,n}^2 - \frac{1}{2}\epsilon_{i,n}^2\zeta_{i,n}^2\right)}^{ports}, \tag{3.49}$$

where ω_n is the resonator field frequency, and ϵ_n is the transmission line field frequency. The coupling Lagranian becomes

$$\begin{aligned}\mathcal{L}_{coupling} = &- C_{in}\left(\sum_{<i,i'>}^{interior}\dot{\varphi}_{i,n}(0)\dot{\varphi}_{i',n}(l_{res})\dot{\xi}_{i,n}^2\dot{\xi}_{i',n}^2\right)\\ &- C_{in}\left(\sum_{<i,i'>}^{edge}\dot{\varphi}_{i,n}(0)\dot{\varphi}_{i',n}(l_{res})\dot{\xi}_{i,n}^2\dot{\xi}_{i',n}^2 + \dot{\varphi}_{i,n}(0)\dot{\varphi}_{i',n}(l_{res})\dot{\xi}_{i,n}^2\dot{\xi}_{i',n}^2\right)\\ &- C_{out}\left(\sum_{<i,i'>}^{edge}\dot{\psi}_{i,n}(l_{res})\dot{\psi}_{i',n}(0)\dot{\zeta}_{i,n}^2\dot{\zeta}_{i',n}^2\right).\end{aligned} \tag{3.50}$$

Now using $\vec{y} = (\xi_{1,1}, \zeta_{1,1}, \cdots)$, the Lagrangian can be cast into a more convenient matrix notation.

$$\mathcal{L} = \frac{1}{2}\dot{\vec{y}}^{\intercal}(\mathbb{I} + \mathcal{K})\dot{\vec{y}} - \frac{1}{2}\vec{y}^{\intercal}\begin{pmatrix}\omega_{1,1}^2 & & & & \\ & \epsilon_{1,1}^2 & & & \\ & & \ddots & & \\ & & & \omega_{i,n}^2 & \\ & & & & \epsilon_{i,n}^2\end{pmatrix}\vec{y} \tag{3.51}$$

where the coupling Lagrangian has been written as $\mathcal{L}_{coupling} = \frac{1}{2}\dot{\vec{y}}^{\intercal}\mathcal{K}\dot{\vec{y}}$.

The Hamiltonian is the Legendre transformation of the Lagrangian $H = p\dot{y} - \mathcal{L}$, and here it can be obtained by perforing a Legendre transformation on the velocity vector $\dot{\vec{y}}$, to obtain the new momentum vector $\vec{p} = \partial\mathcal{L}/\partial\dot{\vec{y}} = (\mathbb{I} + \mathcal{K})\dot{\vec{y}}$. Additionally it will be assumed that $(\mathbb{I} + \mathcal{K})^{-1} \approx (\mathbb{I} - \mathcal{K})$, (valid for $\mathcal{K} \ll 1$). The resulting

hamiltonian is of the form.

$$\begin{aligned} H &= H_{res} - H_{coupling} \\ &= \vec{p}^{\,\intercal}\dot{\vec{y}} - \mathcal{L} \\ &= \frac{1}{2}\vec{y}^{\,\intercal} \begin{pmatrix} \omega_{1,1}^2 & & & & \\ & \epsilon_{1,1}^2 & & & \\ & & \ddots & & \\ & & & \omega_{i,n}^2 & \\ & & & & \epsilon_{i,n}^2 \end{pmatrix} \vec{y} + \frac{1}{2}\vec{p}^{\,\intercal}\vec{p} - \frac{1}{2}\vec{p}^{\,\intercal}\mathcal{K}\vec{p} \end{aligned} \tag{3.52}$$

Using the canonical quantization for the momentum and position vectors $\vec{p}_{i,n} = \sqrt{\omega_{i,n}/2}\ (ia_{i,n}^\dagger - ia_{i,n})$ and $\vec{y}_{i,n} = 1/\sqrt{2\omega_{i,n}}\ (a_{i,n}^\dagger + a_{i,n})$, and then using the RWA, the Hamiltonian begins to take a more familiar form. Now it can easily be seen that the resonator term is of the form of the energy term in a harmonic oscillator, $H_{res} = \sum_{i=1}^{N} \omega_{i,n}(a_{i,n}^\dagger a_{i,n} + \frac{1}{2})$; although the coupling term $H_{coupling} = -\frac{1}{2}\vec{p}^{\,\intercal}\mathcal{K}\vec{p}$ requires further analysis to obtain the photon hopping rates.

The analysis can be made simpler by considering only the fundamental mode $n = 1$. For a CPW resonator the fundamental mode is $\lambda/2$ which implies $\varphi_i(0) = -\varphi_i(l_{res})$. The resulting coupling Hamiltonian is

$$\begin{aligned} H_{coupling} = &- C_{in}\left|\varphi_{in}(0)\right|^2 \frac{\omega_{in}}{2} \sum_{<i,i'>}^{interior} \left(a_i^\dagger a_{i'+1} - a_i^\dagger a_{i'-1} + h.c.\right) \\ &C_{in}\varphi_{in}(0)\varphi_{out}(0)\frac{\sqrt{\omega_{in}\omega_{out}}}{2} \sum_{<i,i'>}^{edge} \left(a_i^\dagger a_{i'+1} - a_i^\dagger a_{i'-1} + h.c.\right) \\ &C_{out}\varphi_{out}(l_{res})\frac{\sqrt{\omega_{out}}}{2} \sum_{<i,i'>}^{edge} \sum_n \tilde{\varphi}_n(0)\sqrt{\epsilon_n}\left(a_i^\dagger b_{i'} + h.c.\right) \end{aligned} \tag{3.53}$$

Leveraging the assumption of the fundamental mode again, it can be assumed that the field is of the form $\varphi(z) = A\cos(z\omega_n\sqrt{lc})$, and the coefficient A can be solved using normalization $1 = A^2 c\int dz\varphi^2(z) = A^2 c l_{res}/2$. Considering just the bath coupling term in the Hamiltonian (term containing C_{out}); the decay rate κ from a

single edge resonator to a transmission line can be extracted with the use of Fermi's golden rule. The density of states in a single edge resonator for the fundamental mode is $\rho(\omega_0) \rightarrow dN/dE = l_{res}\sqrt{lc}/\pi$. The resulting decay rate is given as

$$\begin{aligned}
\kappa &= \frac{2\pi}{\hbar} \left|\langle i|H_{port}|f\rangle\right|^2 \rho(E_i) \\
&= 2\pi \left| \frac{1}{4}\varphi_{out}^2(l_{res})\tilde{\varphi_n^2}(0)\omega_0^2 C_{out}^2 \right| \rho(\omega_0) \\
&= 2\pi \left| \frac{1}{4}\frac{2}{cl_{res}}\cos^2(l_{res}\omega_0\sqrt{lc})\frac{2}{cl_{res}}\omega_0^2 C_{out}^2 \right| l_{res}\frac{\sqrt{lc}}{\pi} \\
&= 2\pi \left| \frac{1}{4}\frac{2\omega_0 Z_0}{\pi}\omega_0^2 C_{out}^2 \right| \frac{2Z_0}{\pi} \\
&= \frac{2}{\pi}\omega_0^3 Z_0^2 C_{out}^2
\end{aligned} \tag{3.54}$$

which is of the same form as equation 3.29. For a lattice with many edge resonators coupled to transmission lines, the total decay rate of the lattice, or the external quality factor, Q_{ext}, of the lattice is effected by all edge resonators coupled to transmission lines. If each edge has a different coupling the total decay rate is

$$\kappa_{total} = \left(\frac{1}{\kappa_1 + \kappa_2 + \ldots + \kappa_{N_{out}}} \right)^{-1} \tag{3.55}$$

where N_{out} is the number of edge resonators coupled to transmission lines.

Considering the internal coupling hamiltonian, there are two types of internal coupling rates, inner-inner, and inner-edge. Here it is assumed that these hopping rates are equivalent which implies that $\omega_{in} = \omega_{out}$, and $\varphi_{in}(0) \approx \Phi_{out}(0)$. Following this assumption the internal hopping rate is given as

$$\begin{aligned}
t_{in} &= C_{in} \left|\varphi_{in}(0)\right|^2 \frac{\omega_0}{2} \\
&\approx C_{in}\frac{2}{cl_{res}}\frac{\omega_0}{2} \\
&= \frac{C_{in}\omega_0^2 Z_0}{\pi}
\end{aligned} \tag{3.56}$$

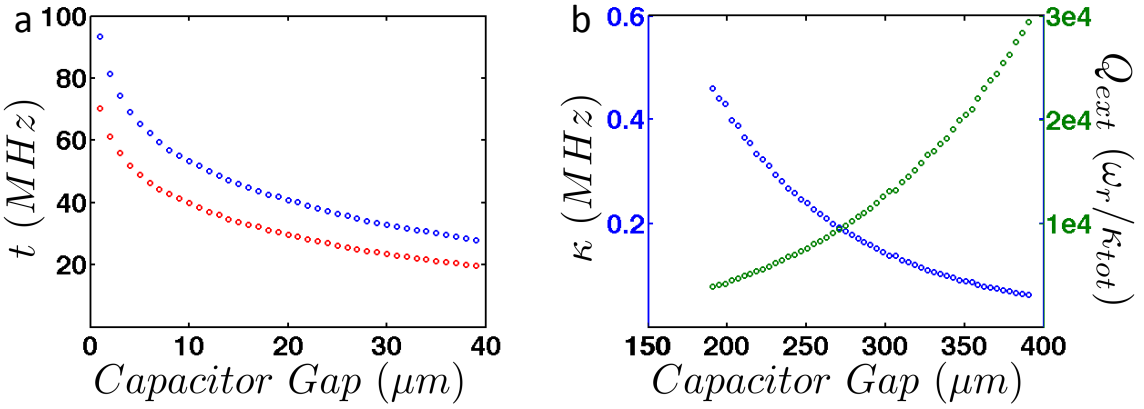

Figure 3.7: Experimental values of the nearest neighbor photon hopping rate **a**, and the photon escape rate **b**. The figures are plotted from equations derived in this chapter, with capacitances determined numerically from finite element software Ansoft Maxwell. **a** Using equation 3.56, the hopping rate is plotted for two different capacitor geometries. In comparison to optical cavities the capacitor functions as a mirror, and the transparency can be tuned by adjusting the gap between cavities. The parameters used for this calculation were $\omega_r = 8$GHz, $Z_0 = 50\Omega$, and C_{in} from the finite element calculation. The two curves are for capacitor geometries with a 200µm wide paddle (red) and a 220µm wide paddle (blue) (see figure 3.10 for example of capacitor geometries). **b** Using equation 3.54, the same parameters the external hopping rate κ was determined for a capacitor with a 220µm wide paddle. Also plotted is Q_{ext}, which is determined by the sum of all resonators coupled to a transmission line (equation 3.55). For the plotted Q_{ext} a lattice with four equally coupled output resonators were considered $\kappa_{total} = 4\kappa$.

It is worth noting here that this is only the magnitude of the inner hopping rate. Due to the $\lambda/2$ nature of the fundamental mode of a CPW resonator there is an awkward minus sign present in the coupling Hamiltonian. This minus sign leads to a frustrated hopping lattice, and for the honeycomb geometry leads to localized modes within the hexagon of the lattice figure 3.8. These localized modes are highly degenerate for a disorder less lattice, and result in a dispersion less photonic band called a flatband. The physics of this flatband will be discussed in more detail in subsequent sections. Here one can treat the minus sign mathematically by doing a gauge transformation with the creation and annihilation operators; using $a_i/a_i^\dagger \rightarrow c_i/c_i^\dagger$ and $d_i/d_i^\dagger$. The result is the well known tight binding Hamiltonian.

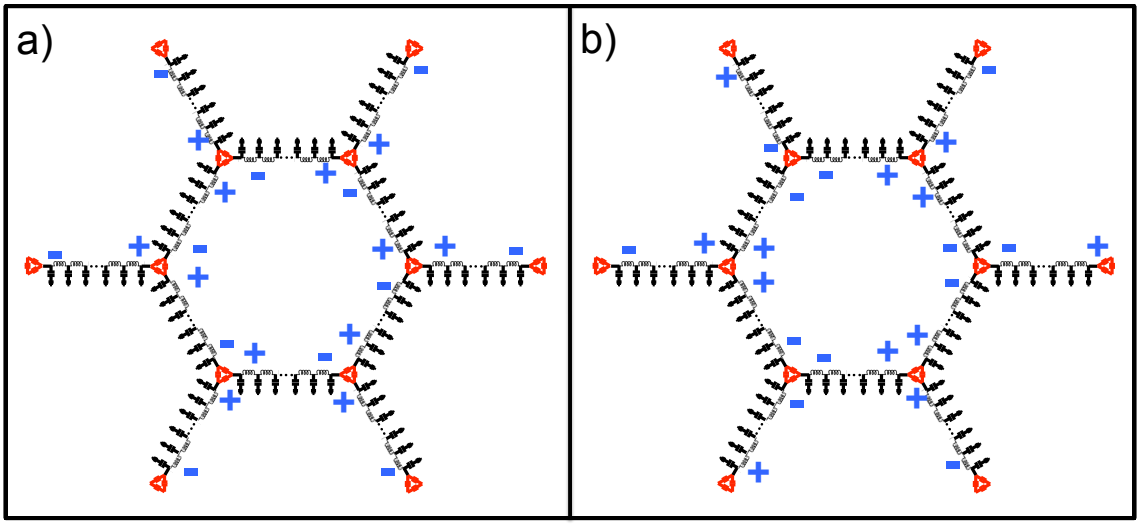

Figure 3.8: **a** The alternating sign of the field in a $\lambda/2$ resonator will result in frustrated coupling elements. For the honeycomb geometry shown here the effect of frustrated coupling is the destructive interference of fields outside the inner hexagon, and can result in localized modes within the hexagons [80, 59, 77]. **b** The frustrated coupling leads to a minus sign in the coupling hamiltonian. The sign of the hopping can be theoretically handled with a gauge transformation.

$$H = t_{in} \sum_{<i,i'>}^{interior} (c_i^\dagger c_{i'+1} + c_i^\dagger c_{i'-1} + h.c.) + t_{in} \sum_{<i,i'>}^{edge} (c_i^\dagger d_{i'+1} + c_i^\dagger d_{i'-1} + h.c.) \qquad (3.57)$$

The two terms in the Hamiltonian correspond to hopping between interior lattice sites, and hopping to the edge sites. With this Hamiltonian all photons are contained within the lattice. In order to consider the effects of lattice decay one would need pursue an open quantum systems approach. In this case a Linblad master equation should be considered.

3.4 Lattice design and fabrication

3.4.1 Lattice design

The physical orientation of the microwave resonators is a honeycomb geometry. Subsequent chapters will discuss how the photonic lattice is actually a Kagome lattice; which is the dual of the honeycomb lattice. For design purposes it is only necessary to consider the honeycomb lattice. The honeycomb lattice is a bravais lattice with a two atom basis, where the separation between atoms is the lattice constant d, and the entire lattice can be spanned with lattice vectors $\vec{a_1}$ and $\vec{a_2}$.

$$\vec{a_1} = \frac{d}{2}\left[3, \sqrt{3}\right] \tag{3.58}$$

$$\vec{a_2} = \frac{d}{2}\left[3, -\sqrt{3}\right] \tag{3.59}$$

A very notable realization of the honeycomb lattice is graphene [76]. In the graphene lattice the atoms sit on the vertices and are separated by edges of length d. However, in a honeycomb lattice of CPW resonators the vertices are the coupling elements, composed of three-way coupling capacitors, and the resonators are the edges spanning a length d that separates the coupling capacitors (figure 3.9).

For designing large honeycomb lattices, the use of lattice vectors can be very advantageous. By first designing a unit cell composed of three resonators (figure 3.10), a lattice can be easily tiled by spacing unit cells at integer lengths of $\vec{a_1}$ and $\vec{a_2}$. Unfortunately with this method issues will arise along the edges of the lattice and can be cumbersome to deal with. All the lattices were designed using python, and then saved in an Autocad dxf file format using the dxfwrite library. Conveniently these files are also compatible with the Heidleberg mask maker in the shared cleanroom.

Designing a large honeycomb lattice of resonators required significant forethought and understanding of the fabrication process in order to make a symmetric disorder

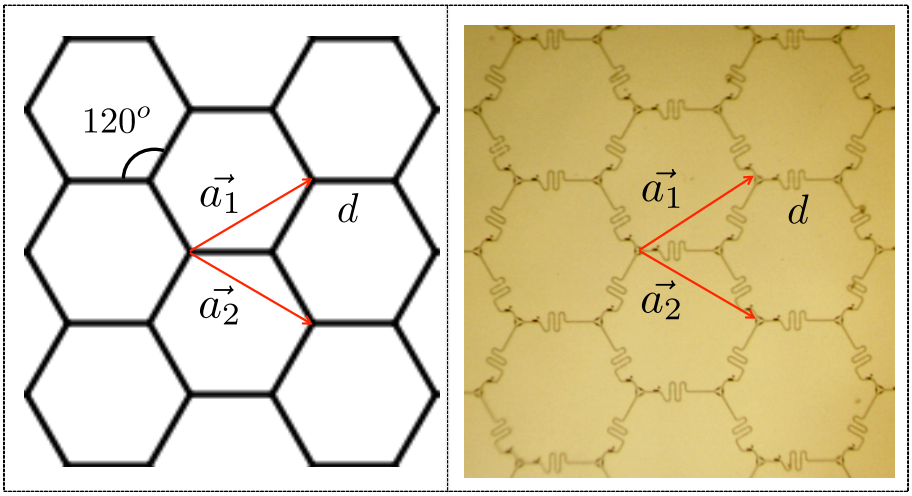

Figure 3.9: A simple honeycomb lattice with lattice vector d. A realization of the CPW resonator honeycomb lattice, where each is capable of yielding superconducting transmon qubits.

less lattice. A useful strategy when designing complicated systems or structures, is to first list all the limitations and restrictions that create a design constraint, and then work towards a solution that satisfies the listed design constraints. Here the design constraints that were considered will be listed, and then a subsequent discussion will be presented outlining how these constraints were satisfied.

The end goal is a symmetric honeycomb lattice of resonators with a superconducting qubit coupled to each resonator. Here the foreseeable design constraints were as follows:

1. a physically small lattice with many sites,
2. identical resonant frequencies at each site (i.e. $\omega_{r,i} = \omega_{r,i+1}$),
3. maintain the same lattice constant d at each site,
4. the qubit position relative to the resonator must be the same for each site; as shown in figure 3.10 $\Delta X_{qubit,\ i} = \Delta X_{qubit,\ i+1}$
5. each qubit must be oriented along the same axis.

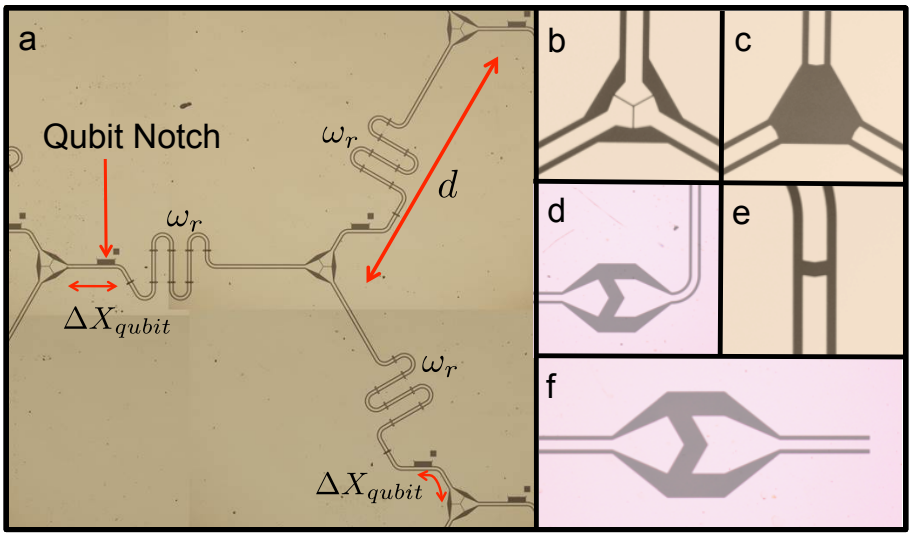

Figure 3.10: **a** The unit cell of the resonator honeycomb lattice. Despite the geometric differences each resonator in the unit cell is designed to be identical in frequency ω_r. The difference is necessary for the qubit fabrication process, which requires each qubit to have the same orientation. The unit cell device parameters were $d = 4000\mu$m, $l_{res} = 7500\mu$m, $\Delta X_{qubit} = 570\mu$m, and $\omega_r = 7.48$GHz. **b** Example of a three way coupling capacitor for a strongly coupled lattice, and **c** a weakly coupled lattice. **d** The output coupling capacitor for strongly coupled lattice, and **e** a weakly coupled lattice. **f** Edge resonator coupled to a $\lambda/4$ boundary resonator that is far detuned from the resonant frequency of the lattice.

A major difficulty associated with designing a two dimensional lattice with many sites is trying to increase the density of lattice sites, for a predetermined chip size. For example, the length of an 8 GHz CPW resonator is $l_{res} \sim 7.5$mm long, and if $l_{res} = d$ then the width of a unit cell would be 11.5mm, and such a lattice does scale reasonably. Typically resonators are designed with a meandering middle section to reduce the length, and for 2D lattices this works fine as long as the start and end of the resonator are aligned along the same axis.

In order to ensure $\omega_{r,i} = \omega_{r,i+1}$, the length of each resonator must be the same at each site; additionally each resonator must also have the same number of meandering sections. It is understood that the effective length of a CPW bend is different than the effective length of a straight (i.e. $l_{bend} = r_{bend}\theta \neq l_{straight}$), and a difference in meander number can result in systematic frequency disorder. Furthermore the bend

radius chosen needs to be much larger than the feature geometry of the CPW (i.e $r_{bend} \gg (s + 2w)$).

Integrating qubits in the lattice makes it more difficult to maintain symmetry. Due to the qubit fabrication process, each qubit must be oriented along the same axis, and also in order to reduce disorder in the qubit-resonator coupling g each qubit must be the same distant ΔX_{qubit} from the capacitor. This will ensure that each qubit is coupled to the same field maximum V_{max}. The result of satisfying all these design requirements was a unit cell composed of three physically different resonators that are identical in frequency (figure 3.10). The consequence of satisfying these constraints was an increase in the lattice vector d which meant that the lattice site density was reduced.

Measurement in these lattices is performed by driving one edge resonator and measuring the transmitted signal through a second edge resonator. Edge resonators that are used for measurement are capacitively coupled to a transmission line. For large lattices it is inevitable that there will be more edge resonators than measurable RF lines within the dilution refrigerator. The left over dangling edge resonators were managed by capacitively coupling to a far detuned quarter wavelength boundary resonator.

3.4.2 Lattice fabrication

A circuit QED lattice is fabricated using both optical lithography and electron beam lithography. A lattice without qubits is easily fabricated with standard photolithography techniques because the smallest feature sizes are greater than 2μm (figure 3.10) (standard photolithography starts to become difficult for feature sizes less tha 1μm). For photolithography, an $\sim$ 800nm layer of AZ 1508 is used pattern lattices on a thin 200nm film of Nb that has been sputtered onto a 0.5mm thick epipolished sapphire wafer. After exposing and developing the photoresist, a short O_2 descum is

performed to remove any undeveloped resist. Following the descum the Nb is etched for 40s in SF6 plasma, inside an inductively coupled plasma etcher. After etching, the left over photo resist is chemically removed and then another 'protective' layer of resist is applied so the lattice can be put into a dicing saw, and cut to the proper size. Post dicing, the protective resist is chemically removed and then the lattices can be prepped for qubit fabrication. Since qubits are very delicate devices, they should always be the final fabrication step!

In this thesis results are only presented for an empty lattice, so only a brief discussion of the qubit fabrication process will be presented here. As previously mentioned the lattices have been designed to easily integrate transmon qubits; once the photolithogrpahy procedures have been completed. The key component of the transmon qubit is a Josephson junction which is about 100x100nm and fabricated using a Dolan bridge technique [27]. This technique is a bilayer resist process in which the bottom layer of resist is exposed leaving the top layer remaining in the form of a bridge. The bottom layer of resist is a copolymer MMA(8.5) EL 13 (Ethyl-lactate 13%), and spins to about 550nm at 4000rpm. The top layer of resist is PMMA A3 (955k weight) from Microchem, which spins to approximately 120nm thick at 4000rpm. A more detailed discussion of this fabrication process can be found in [91].

3.5 Packaging

3.5.1 Connecting ground planes

For each lattice it is critical that the ground planes are well grounded! For typical cQED devices a high density of wirebonds is used to help prevent parasitic slot line modes [105]. This is particularly important for large lattices because the isolated ground planes are even more susceptible to slotline modes and undesirable excitations

in the ground plane. In this thesis various methods have been explored in order to provide good connections between isolated ground planes and will be discussed.

Wirebonding isolated ground planes is proven to be the easiest and most convenient method of connecting ground planes, but there are disadvantages to using wirebonds. For example wirebonds have a large inductance, and a poorly placed wire bond can be a source of flux noise in qubits. It has also been shown that a high density of wirebonds is necessary to impede the propagation of slotline modes [16]; which isn't always possible on chip. Additionally for large devices, wirebonds are not a scalable method. The large lattice presented in this thesis are fabricated on a $35x35$mm chip, and can contain up to 200 sites. Consequently these lattices require > 1000 wirebonds that must be individually placed . Even with the help of an automatic wirebonder (Questar Q7000 series) this is a very cumbersome task. It generally takes many hours, and one slip of the hand can result in a misplaced wirebond that will ruin a device.

Alternatives to wirebonding have been considered, and are an active area of research within the superconducting qubit community. Here three methods that have been considered will be discussed and while not all have been implemented for experiments in this thesis, it is believed that these methods present a more scalable alternative to wirebonds. The methods that have been considered are micro fabricated air bridges, dielectric supported bridges and via holes through the substrate. Micro fabricated air bridges have been demonstrated in previous cQED experiments, and have demonstrated a reduction in the slot line modes by reducing the total inductance [16]. While these have been shown to be advantageous over wirebonds there are concerns and technical difficulties associate with them. The most obvious concern is that they must all be made with 100% confidence because one collapsed bridge will result in a shorted ground plane. It is understood that the reliability of fabricating airbriges increases as the thickness of the metal film increases. One major drawback

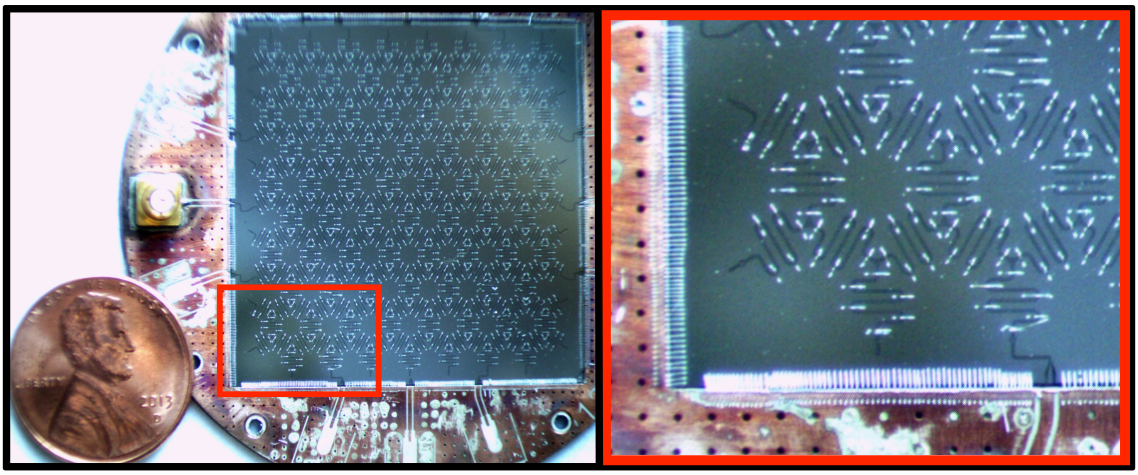

Figure 3.11: Over 1000 wire bonds used to connect ground planes to the copper circuit board and also the isolated ground planes of a 219 site lattice. In the zoomed in portion of the picture the high density of wirebonds can be observed. Wirebonds are placed with $\sim$ 100µm spacing. Typically placing wire bonds from the copper circuit board to the Nb chip were the most troublesome. This is a common issue, and is usually the result of poorly mounting the device to the circuit board, and not properly cleaning the surface of the circuit board. In general bonding from one Nb surface to another was not problematic, but it is advised to move carefully because one slip of the hand can easily produce a wire bond over a center pin; thus ruining the device.

to these air bridges is the subsequent qubit fabrication. Due to the delicate qubit fabrication process; qubits must be the final fabrication step, and the post bridge processing has detrimental effects on bridge structure.

Supported bridges are a safer alternative to air bridges, but the added dielectric that is used to support the crossover connections will result in undesirable loss. In this thesis supported bridges were developed and used for experiments involving a scanning probe that was brought into contact with the surface of the lattice (figure 3.12). Here the support layer was a material called bisbenzocyclobutene (BCB), also referred to as spin on glass. The type of BCB used was Cyclotene 4022-35 and was selected because it can be patterned like photoresist using optical lithography, and it has a very low loss tangent in the microwave regime $\gamma = 0.0002$ at up to $10GHz$ [68]. BCB is an arduous material to work with, but despite the difficulty it turned

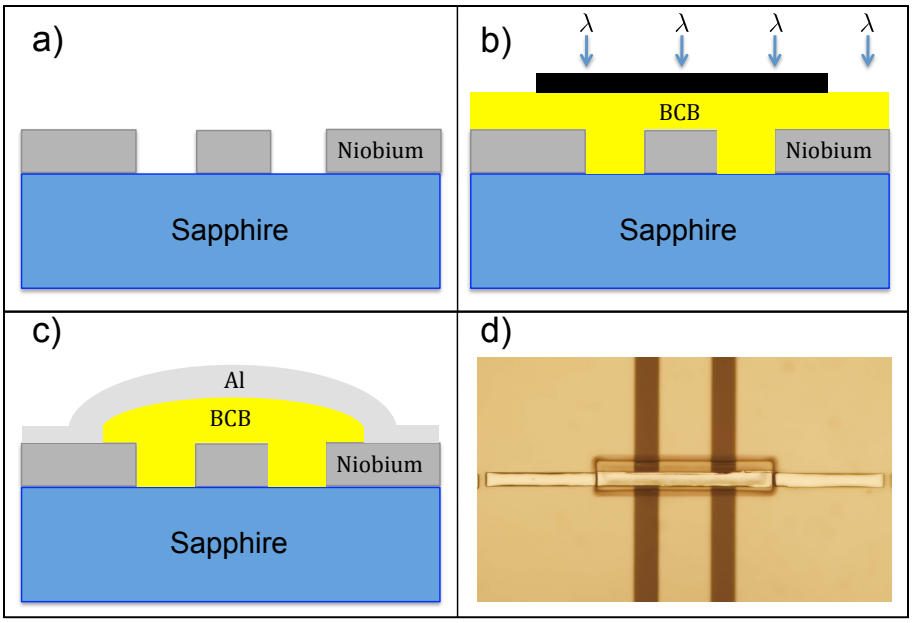

Figure 3.12: Lithography process for BCB supported bridges that connect isolated ground planes. Starting with a CPW resonator, the BCB is spin coated on the device. Following the baking process the BCB is exposed, and since it is a negative resist, the regions that are not exposed get removed in the developer. The BCB is then cured at very high temperatures in a vacuum oven. After the BCB has been patterned, a liftoff photolithography step is used to deposit aluminum over the BCB. The result is a strip of aluminum supported by BCB.

out to be more reliable than deposited dielectrics. BCB is a negative resist which means the unexposed regions get washed away during development. It spins to about 4μm thick, and post development it must be cured at 250 C in a vacuum over for optimal electrical properties. See appendix B.1 for a detailed recipe. Following the BCB deposition, a 300nm Al film is evaporated over the BCB with connections made to the Nb ground planes. A 5 degree angled evaporation is used while rotating the sample; this helped to ensure a conformal film thickness over the edges of the BCB.

Another approach that was considered but not fully tested was using via holes to connect the upper ground plane to a lower ground plane. It is mentioned here because ideally it could work without any of the drawbacks previously mentioned. The process considered would be to laser drill small via holes on a thin sapphire substrate, and then sputter Nb on both sides of the wafer. For good connections, it

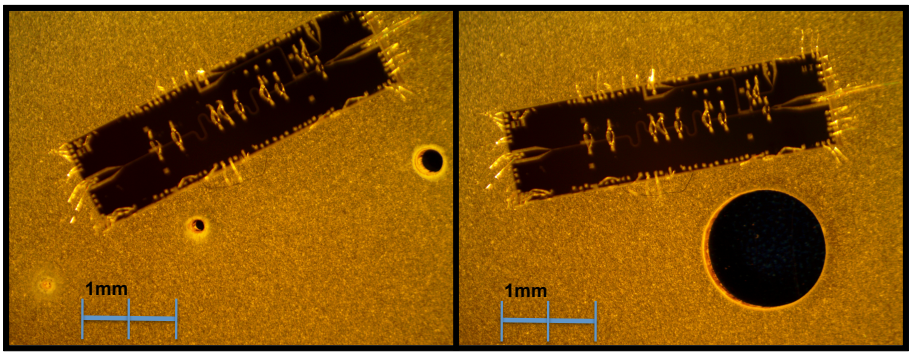

Figure 3.13: Images of laser drilled holes in a 0.5mm sapphire wafer, pictured with an old 2x7mm single resonator cQED device for reference. The drilled holes are shown here to illustrate that it is possible to create via hole ground connections on isolated ground planes on a large lattice. Furthermore small vias could be developed on smaller chips for the purpose of quantum simulation. The diameters of the three hole sizes shown in the two pictures are $\sim$ 250µm, $\sim$ 500µm, and $\sim$ 2mm. These types of ground connections were not implemented in this thesis, but I believe that given the drawbacks and technical difficulties associated with other methods via holes have the more potential for a scalable and more reliable method of connecting ground planes.

is important to consider the aspect ratio of the substrate thickness and the via hole diameter. For small diameters and thick substrates, it will be difficult to ensure the sputtered Nb makes connections through the bias. Here images are shown of small laser drilled holes in a 0.5mm thick sapphire substrate using a 500Watt YAG laser (figure 3.13). By first patterning the via holes, devices could easily be patterned around the via holes resulting in well connected ground planes without unnecessary wirebonds or crossover bridges.

3.5.2 Printed circuit boards, and sample holders

In order to measure large lattices it was necessary to design and construct new hardware, and new technical expertise in order to measure these devices at low temperatures. The technology developed here is complimentary to hardware used in traditional cQED experiments, but scaled up to incorporate more RF input lines, and larger chip sizes. Much of the technical challenges that were overcome were related to

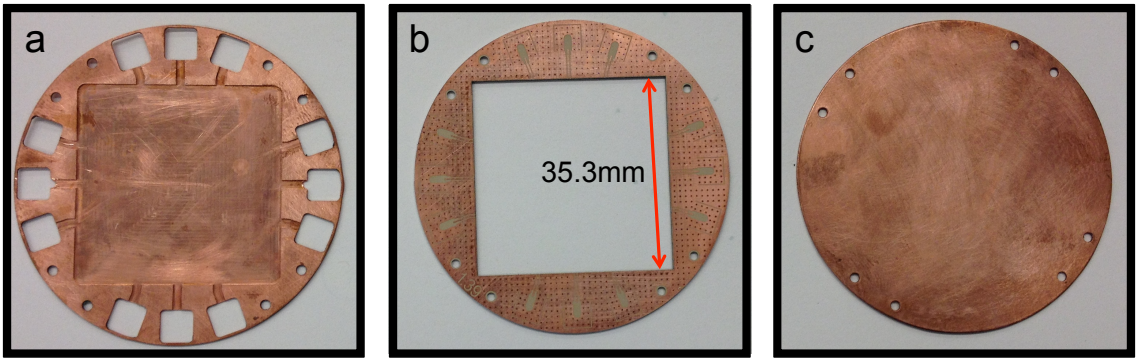

Figure 3.14: Printed circuit board assembly for the dodecahedron sample box. This assembly is design to neatly package large devices of microwave circuitry in an elctromagnetically shielded environment. **a**, A coverslip that fits over the microwave circuitry and prevents spurious radiation from coupling to the device. **b**, The twelve port PCB designed for larger devices, more specifically lattices of microwave cavities. The different ports provide different means of driving and measuring external lattice sites. The wafer sits within the large hole in the center of the device. **c**, Copper plate that the PCB is mounted to, in order to support the wafer that sits within the hole in the PCB.

the difficulty associated with large devices. These technical challenges are addressed in this section.

All devices must be properly thermally connected to a base plate of a dilution refrigerator in order for the devices to reach a base temperature of ∼20mK. In order to do this post fabricated devices are mounted to copper printed circuit board (PCB) using a conductive cryogenic high performance silver paste (PELCO. Product No. 16047), and then mounted to a sample box machined from oxygen free copper. The sample box is then secured to the baseplate of the dilution refrigerator. During each mounting procedure good mechanical contact is essential. Additionally, to promote thermal conductivity, small amounts of Apiezon N-Grease can be applied between surfaces.

Since large lattices have many edge resonators, sample boxes were designed to accommodate up to twelve RF connections; the maximum number of ports possible (figure 3.15). Maximizing the number of ports also allows for flexibility when designing future experiments. All RF cables used on the sample box and on the base

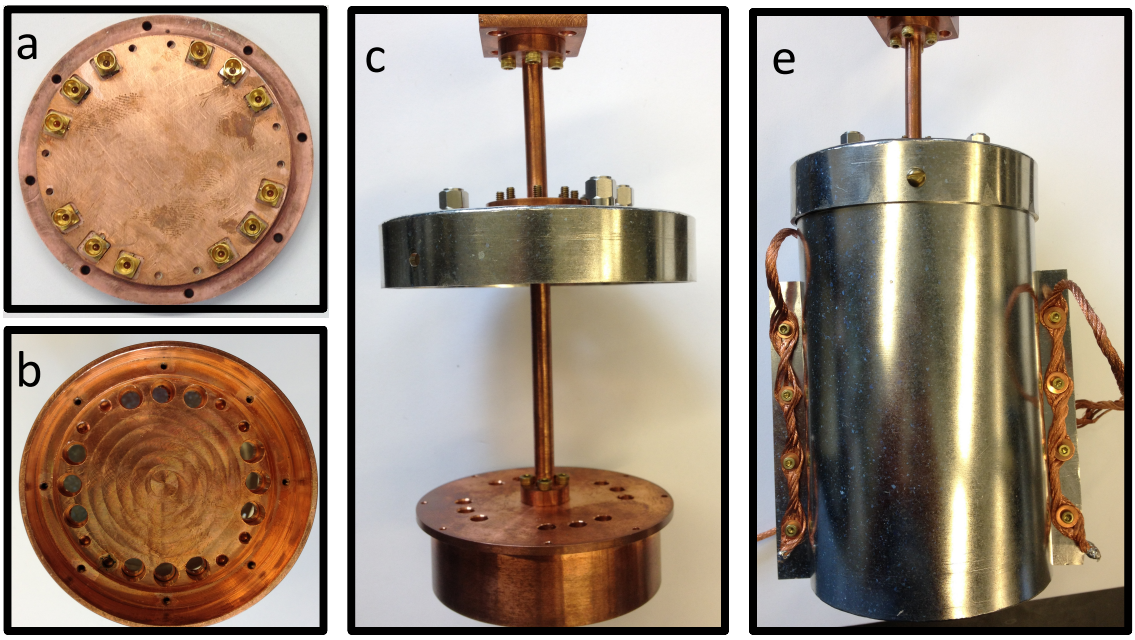

Figure 3.15: The sample box used to package and mount the large microwave circuits to the base plate of a dilution refrigerator, in an environment that is electrically and magnetically shielded. All sample box material is machined out of high purity oxygen free copper, to ensure maximum thermal conductivity. **a**, The assembled microwave circuit board mounted to the base of the sample box. The RF connectors on the circuit board align with the holes for RF cables on the lid. **b**, An overhead view of the lid. **c** The sample box assembly is mounted to copper rods that are secured to the lid of a mu-metal shield. Although not pictured, RF cables will secure to the mu-metal lid and extend to the lid of the sample box. **d** Complete mu-metal shielding for sample box, that is mounted to refrigerator baseplate. Maximum flux shielding is achieved when the sample box positioned near the bottom of the Mu-metal shield.

plate of the dilution unit were made from semi-rigid UT-85C-TP-LL cables, and were custom made for each sample box. Unused sample box cables were terminated with 50Ω terminators. The sample boxes were designed to fit within a Mu-metal shield that was thermally anchored to the base plate with thick oxygen free copper braids. The Mu-metal shield provides necessary shielding from unwanted flux noise.

The PCBs were designed and then constructed from Arlon AD1000, which is a low loss dielectric sandwiched between electrical grade copper (figure 3.14). The material and the design were sent to Hughes Circuits to be made. All transmission lines on the PCB were designed to be 50Ω, and the upper and lower copper plates were connect by

a high density of via holes. For smaller chips sizes the center of each chip was milled out to leave a pocket just large enough for a fabricated devices. For large lattices the pocket size was too large and the entire region was milled out. In order to secure the device to the PCB, a copper plate was soldered to the backside of the PCB using Amtech NWS-4100 solder. RF connectors were soldered to the topside of the PCB with NWS-4100 by carefully applying the solder and then heating on a hotplate for a few minutes at 225^{o}C. For best results a generous amount of solder is suggested.

Prior to mounting devices to PCBs it is critical that the device is properly cleaned and polished. A thick oxide will be formed on the PCBs after connectors have been soldered, and this must be removed or else wire bonding will not be possible. The treatment found to work best is as follows: soldering flux is first used to remove the unwanted oxide, followed by a Q-tip covered in IPA to remove the corrosive flux. Afterwards a fiberglass pen is gently used around the edge of the cutout region in order to polish the surface, followed by Q-tip covered in IPA to remove any residual copper. After cleaning the PCB the device can be securely mounted using the conductive silver paste. Here it is important to apply a uniform layer so the device sits flat.

Chapter 4

The Photonic Kagome Lattice

4.1 Introduction

An idea of growing interest is to use photons as particles in a quantum simulator for non-equilibrium systems [61, 42, 38, 3, 43, 75, 47]. According to this idea, a photon lattice is created with an array of cQED elements, each consisting of a photonic cavity coupled strongly to a two level system, or qubit. In these lattices, photons can hop between neighboring cavities and experience an effective photon-photon interaction within each cavity, mediated by the qubit. The superconducting circuit architecture is an attractive candidate for realizing such lattices due to the flexibility afforded by lithographic fabrication and the relative ease of attaining strong coupling [8]. Such cQED lattices have been predicted to exhibit a wide variety of phenomena, including a superfluid-Mott insulator transition [61, 42, 38, 3], macroscopic quantum self trapping [87], and even fractional quantum Hall physics [43].

Prior to fabricating such a complicated system a necessary first step is to understand a lattice without qubits. This chapter focuses on understanding the empty lattice, more specifically the photonic Kagome lattice which naturally arises from a two-dimensional lattice of transmission line resonators. The signature of the Kagome

lattice is the triangular plaquettes that make up the unit cell (figure 4.1); the source of geometric frustration in the Kagome lattice. For this reason the Kagome lattice has been a model of great theoretical interest for the study of frustrated spin systems, and magnetism. For example it was used for the first proof of ferromagnetism on the Hubbard model [69]. More recently there has been significant interest on studying the ground state of interacting bosons [49, 80, 106]. The cQED lattices proposed in this thesis represent an ideal architecture for realizing such a system of interacting bosons.

Much of the interest in the Kagome lattice is due to the dispersionless band that forms from the geometric frustration. This can be observed in the band structure, and in this chapter a derivation of the Kagome lattice band structure will be presented, along with a discussion of other unique properties associated with the Kagome lattice. Transport measurements are the standard form of measurement used in these experiments. A subsequent discussion on how these measurements are conducted is presented. Subsequently, a transport measurement on a 219 site lattice will be presented and shown to comply with expected results from tight binding calculations.

In order for these lattices to be a useful for quantum simulation it is necessary to be able to reliably fabricate low disorder lattices. To demonstrate this the smallest complete two dimensional Kagome lattice (a 12-site lattice) was studied to asses the reliability of the fabrication process. This is refereed to as a Kagome star and in this experiment 25 different devices were measured for two different photon hopping rates $t_{i,j} = 0.8$MHz and $t_{i,j} = 31$MHz. The spectra from transport measurements were analyzed in order to study the effects of random disorder. By modifying the CPW resonator geometry the random disorder was shown to be reduced to a few parts in 10^4 of ω_r, indicating that a lattice-based quantum simulator is a realizable goal. The work on the Kagome star was published in Physical Review A [100], and in this chapter a detailed review of how these results were achieved will be presented.

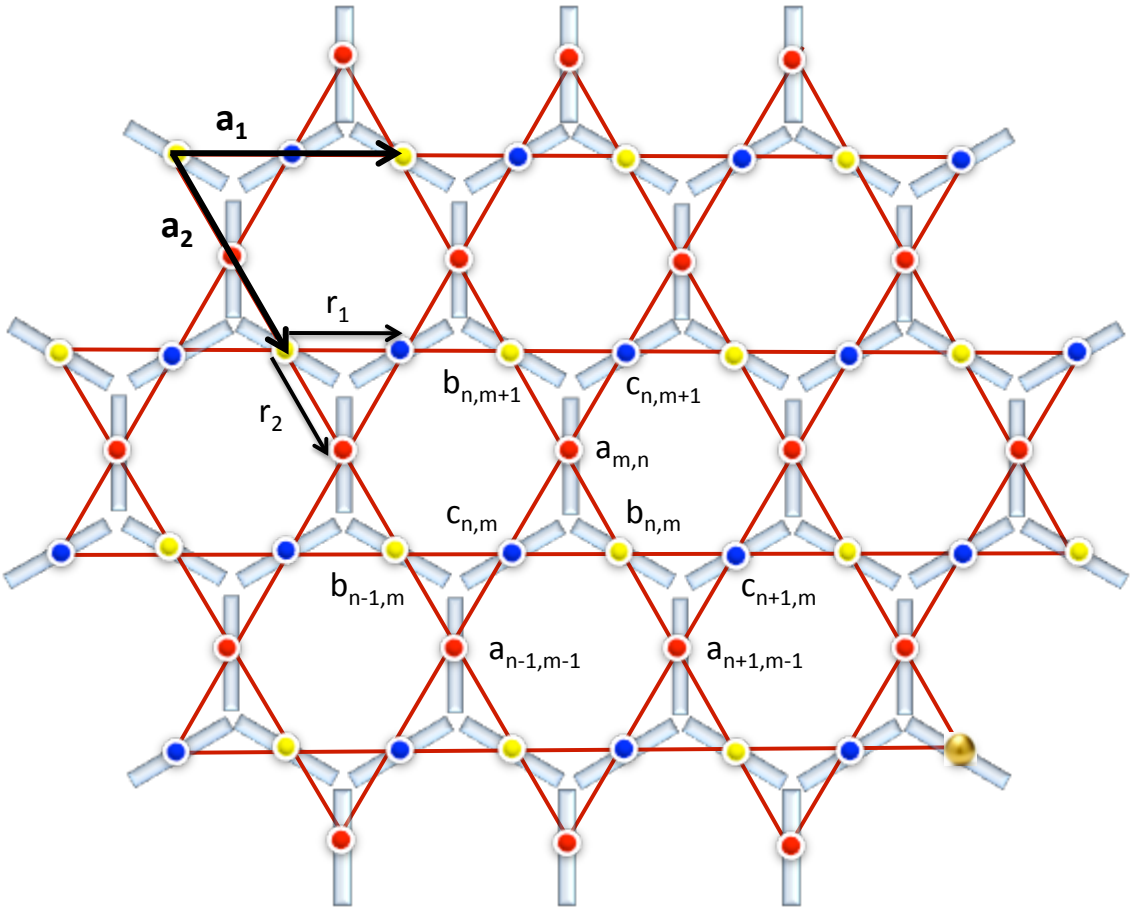

Figure 4.1: The Kagome lattice is the reciprocal lattice of the honeycomb lattice. Here both lattices are illustrated. The Kagome lattice is a bravais lattice with a three atom basis, described by primitive vectors $\mathbf{a_1}$ and $\mathbf{a_2}$, and basis vectors $\mathbf{r_1}$ and $\mathbf{r_2}$. Each atom in the unit cell is indicated by a different color. The labeling scheme (a,b,c) is used in the subsequent derivation of the band structure.

4.2 Kagome Lattice Bandstructure

The Kagome lattice has a very unique band structure. The most interesting aspect of the band structure is the dispersionless band that is consequence of the destructive interference on the triangular plaquettes. Here a derivation of the band structure is presented beginning with a tight binding hamiltonian [59].

The primitive vectors that define the Kagome lattice are given as

$$\vec{a}_1 = a(1, 0) \tag{4.1}$$

$$\vec{a}_1 = a(1, \frac{1}{\sqrt{3}}) \tag{4.2}$$

and the basis vectors that describe the unit cell can be expressed as

$$\vec{r}_0 = (0, 0) \tag{4.3}$$

$$\vec{r}_1 = \frac{\vec{a}_1}{2} \tag{4.4}$$

$$\vec{r}_2 = \frac{\vec{a}_2}{2} \tag{4.5}$$

The allowed energy levels of a Kagome lattice are given by a tight binding hamiltonian,

$$\begin{aligned} H_{TB} = \omega_r \sum_{n,m} \left(a^\dagger_{n,m} a_{n,m} + b^\dagger_{n,m} b_{n,m} + c^\dagger_{n,m} c_{n,m}\right) + \\ t \sum_{n,m} (a^\dagger_{n,m} b_{n,m} + b^\dagger_{n,m} c_{n,m} + c^\dagger_{n,m} a_{n,m} + \\ a^\dagger_{n-1,m-1} c_{n,m} + a^\dagger_{n+1,m-1} b_{n,m} + c^\dagger_{n+1,m} b_{n,m}) + H.C. \end{aligned} \tag{4.6}$$

where the a, b, c ($a^\dagger b^\dagger c^\dagger$) are the creation (annihilation) operators for photons for nearest neighbor sites, and the coupling scheme can be observed in figure 4.1. The momentum space representation of the tight binding hamiltonian can be obtained by performing a Fourier transform on H_{TB}.

$$\begin{aligned} H_{TB} = \omega_r \sum_{\vec{k}} \left(a^\dagger_{\vec{k}} a_{\vec{k}} + b^\dagger_{\vec{k}} b_{\vec{k}} + c^\dagger_{\vec{k}} c_{\vec{k}}\right) + \\ t \sum_{\vec{k}} \left(2a^\dagger_{\vec{k}} b_{\vec{k}} \cos(\vec{k} \cdot \vec{r}_2) + 2b^\dagger_{\vec{k}} c_{\vec{k}} \cos(\vec{k} \cdot \vec{r}_1) + 2c^\dagger_{\vec{k}} a_{\vec{k}} \cos(\vec{k} \cdot \vec{r}_1 - \vec{r}_2)\right) + H.C. \end{aligned} \tag{4.7}$$

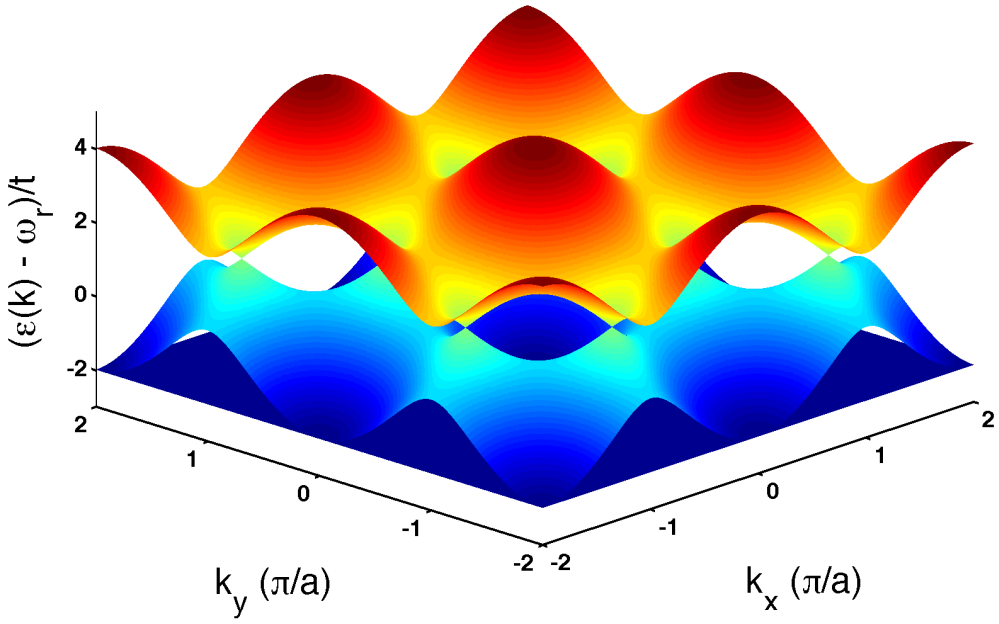

Figure 4.2: Bandstructure of a Kagome lattice calculated with equations 4.9. The allowed energies have been shifted by ω_r, and normalized to the hopping rate t. Three bands are observed, with the lowest energy band being a dispersionless band at energy $\epsilon(k) = \omega_r - 2t$. With the exception of the flatband, the Kagome band structure is very similar to that of graphene. At six points in the first Brilluon zone, the upper and lower bands meet at a dirac point, at energy $\epsilon(k) = \omega_r + t$. The dispersion around these singular points changes linearly with $\vec{k}$ and are known as dirac cones. In this linear limit the points around the tight binding hamiltonian can be simplified and shown to give rise to the dirac equation [62, 35].

Using the lattice symmetry this hamiltonian can now be expressed in a block diagonal from

$$H_{TB} = \sum_{\vec{k}} (a^\dagger b^\dagger c^\dagger) \begin{pmatrix} \omega_r & 2t\cos(\vec{k}\cdot\vec{r}_2) & 2t\cos(\vec{k}\cdot\vec{r}_1 - \vec{r}_2) \\ 2t\cos(\vec{k}\cdot\vec{r}_2) & \omega_r & 2t\cos(\vec{k}\cdot\vec{r}_1) \\ 2t\cos(\vec{k}\cdot\vec{r}_1 - \vec{r}_2) & 2t\cos(\vec{k}\cdot\vec{r}_1) & \omega_r \end{pmatrix} \begin{pmatrix} a \\ b \\ c \end{pmatrix} \quad (4.8)$$

The dispersion $\epsilon(k)$ is thus obtained from diagnolization of the 3x3 matrix and gives rise to three energy bands.

$$\epsilon_1(k) = \omega_r - 2t \tag{4.9}$$

$$\epsilon_{2,3}(k) = \omega_r + t \pm |t| \sqrt{4\left(\cos^2(\vec{k}\cdot\vec{r}_1) + \cos^2(\vec{k}\cdot\vec{r}_2) + \cos^2(\vec{k}\cdot\vec{r}_1 - \vec{r}_2)\right) - 3} \tag{4.10}$$

The resulting band structure has some unique properties. Similar to graphene there are six dirac points within the first brilluon zone located at

$$\begin{aligned}
\vec{k} &= (4\pi/3a, 2\pi/3a) \\
&= (-4\pi/3a, -2\pi/3a) \\
&= (2\pi/3a, 4\pi/3a) \\
&= (-2\pi/3a, -4\pi/3a) \\
&= (-2\pi/3a, 2\pi/3a) \\
&= (2\pi/3a, -2\pi/3a)
\end{aligned} \tag{4.11}$$

The signature of these points is the linear dispersion close to the dirac point, and in this linear limit takes the form of the massless dirac equation [62, 35]. Additionally the lowest frequency band is a dispersionless band at energy $\epsilon(k) = \omega_r - 2t$. For fermionic systems the unit cell represents a highly unstable spin region, and gives rise to complicated ground states [29]. Although more relavant to the system of interest is the study of weakly interacting bosons in a dispersionless band. In this band the group velocity will be zero $d\omega/dk = 0$, and degenerate localized states are expected. If the flatband is the lowest energy band bosons will condense in these localized states, and the nature of the ground state will be determined by the interactions of the bosons [49].

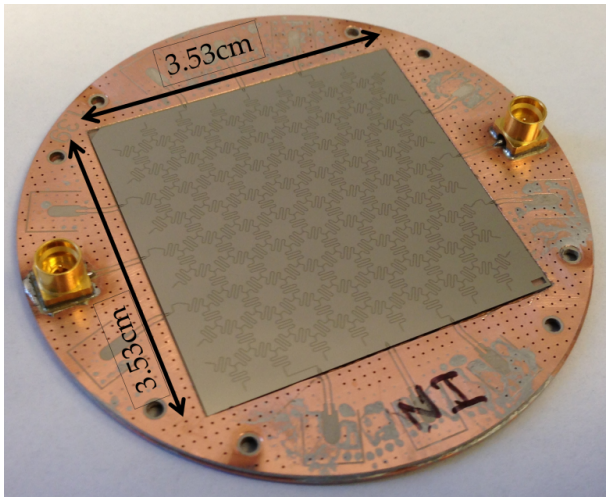

Figure 4.3: A 219 site lattice Kagome lattice mounted on a copper PCB. The gold plated SMP connectors are used as input/ouput ports for the lattice. All edge resonators that are not connected to input/output ports are capacitively coupled to a $\lambda/4$ resonator that is far detuned from the lattice (see section 3.4.1).

4.3 Transport measurements

Two-dimensional lattices represent a complicated network of microwave circuitry, but are limited to the same two port measurement techniques used in even the simplest microwave circuitry. In these experiments a vector network analyzer is used to measure the frequency dependence of lattices by measuring S21 through two edge resonators. All measurements are conducted in CW mode, and the amplitude of the observed spectrum is in units of dB= 10Log(V_1/V_2), where V_2 is the voltage measured at the input port of the analyzer, and V_1 is the voltage measured at the output port of the analyzer. The major drawback to these types of measurements is that only limited information about interior lattice sites can be extracted, and it is not possible to directly measure transport through an interior lattice site without breaking the symmetry of the lattice.

Results are presented for transport measurements on a 219 site lattice conducted between two edge resonators on opposite sides of the lattice. The observed spectrum is a measurement of all normal modes with measurable weight of resonators that

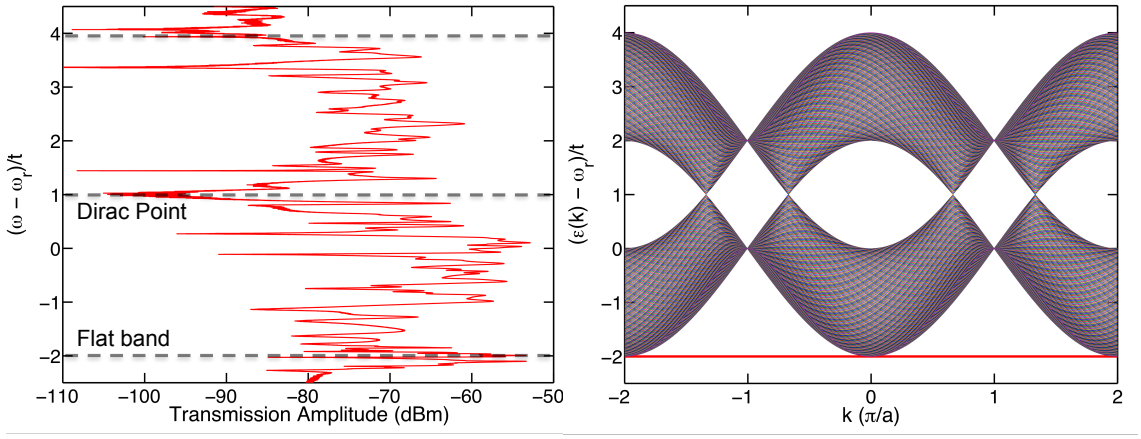

Figure 4.4: Transport measurements through 219 site Kagome lattice plotted next to a planar projection of a Kagome lattice band structure calculation. The measured spectrum shows three bands that comply with the expected Kagome lattice bands. The plots were align by shifting the frequency axes by the bare cavity resonance, and normalized by t. Comparable features are a wide dip in the transmission spectrum is observed near the expected dirac point is at energy $\omega_r + t$; along a low mode density near this point. Additionally many peaks are observed near the expected flatband frequency $\omega_r - 2t$. Since the lower band touches the flatband many peaks are expected in this region. Discrepancies between data and expected values are believed to be the result of random disorder, and undesirable slot line modes in the ground plane. There are many possible sources of slot line modes, but most the most common source is insufficient ground connections (section 3.2.2), and post measurement inspection points towards this as a major contribution.

are coupled to the input and output drive ports of the lattice. While the spectrum appears to be a complicated mess of peaks, the outline of the three expected bands can be observed (figure 4.4). By plotting the spectrum in this manner, and next to the expected band structure, the outline of the three bands becomes more apparent. For this reason the normalized frequency is plotted on the vertical axis. The frequency axis of the measured spectrum was normalized with device parameters $\omega_r = 8.55$GHz and $t = 27.5$MHz.

4.4 The Effects of Disorder in the Kagome Star

4.4.1 Disorder in the Hamiltonian

Here 25 arrays of microwave cavities have been fabricated and characterized with each cavity designed to be identical. The focus of these experiments is to understand and reduce uncontrolled disorder in arrays of resonators in a kagome geometry. It was discovered that disorder in the individual resonator frequencies mainly originates from variations in the kinetic inductance due to small changes in the transverse dimensions of each resonator. The disorder was reduced to less than two parts in 10^4 with a suitable choice in the geometric layout of the transmission line resonators.

The system of coupled cavities is described by the Hamiltonian:

$$H = \sum_i \hbar(\omega_r + \delta_i)(a_i^\dagger a_i + \tfrac{1}{2}) + \sum_{j>i} \hbar t_{ij}(a_j^\dagger a_i + a_i^\dagger a_j) \tag{4.12}$$

where $a_i^\dagger, a_i$ are the photon creation and annihilation operators corresponding to resonator i in the array. Where the frequency of resonator i and its shift due to random disorder is given by ω_r and δ_i, respectively. As derived in section 3.3.1 the hopping rate between resonators i and j is given by

$$t_{ij} = 2Z_0 C_{ij}(\omega_r + \delta_i)(\omega_r + \delta_j), \tag{4.13}$$

where C_{ij} denotes the coupling capacitance between the cavities and Z_0 the characteristic impedance of the transmission line [77]. The array studied consists of twelve resonators coupled capacitively at their endpoints in a two-dimensional kagome geometry (figure 4.6). Photon hopping was achieved by coupling triples of resonators in the interior of the array with symmetric three-way capacitors. This coupling scheme naturally results in a kagome lattice.

In an ideal array with uniform resonator frequencies ω_r and hopping rate t, the spacing between normal mode frequencies scales linearly with the photon hopping rate, with a frequency separation between the highest and lowest modes of $(3+\sqrt{5})t$; which arises from diagonalizing the 12x12 matrix resulting from equation (4.12). Assuming that disorder in coupling capacitances is negligible, it is discovered that disorder in resonator frequencies leads to shifts of the normal mode frequencies through the first term in equation (4.12) by an amount $\sim \delta_i$, whereas the additional disorder in t_{ij} only results in corrections $\sim \delta_i t/\omega_r$. Since $\omega_r \gg t_{ij}$, we can thus approximate the photon hopping rate to be uniform with value $t = 2Z_0 C\,\omega_r^2$ for nearest-neighbor resonators (equation 3.56), and $t_{ij} = 0$ for other resonator pairs. Therefore, the primary focus of these experiments is concerned with effects of disorder in resonator frequencies (i.e. reducing δ_i).

4.4.2 Distribution of Disordered Normal Modes

Without disorder, there are eight distinct mode frequencies, four of which are doubly degenerate. The presence of disorder breaks the degeneracy, widens the distribution of normal mode frequencies, and results in twelve distinct frequencies. We study the effects of disorder by numerically diagonalizing the Hamiltonian (equation 4.12) for random $\{\delta_i\}$ drawn from a Gaussian distribution with a standard deviation σ. The resulting histogram for the number of eigenmodes $N(\omega)\,d\omega$ in a given frequency interval $[\omega, \omega+d\omega]$ is shown in figure 4.5 for varying amounts of disorder σ. When $\sigma \ll t$, disorder is negligible and the normal mode frequencies are all close to those of the ideal lattice. As σ increases and becomes larger than t, the peaks in the distribution associated with individual normal mode frequencies broaden and ultimately merge. Once merging occurs, the observed mode frequencies and corresponding modes can no longer be easily identified with the idealized modes, and the device is considered to be dominated by disorder. In the limit of $\sigma \gg t$, the normal mode histogram

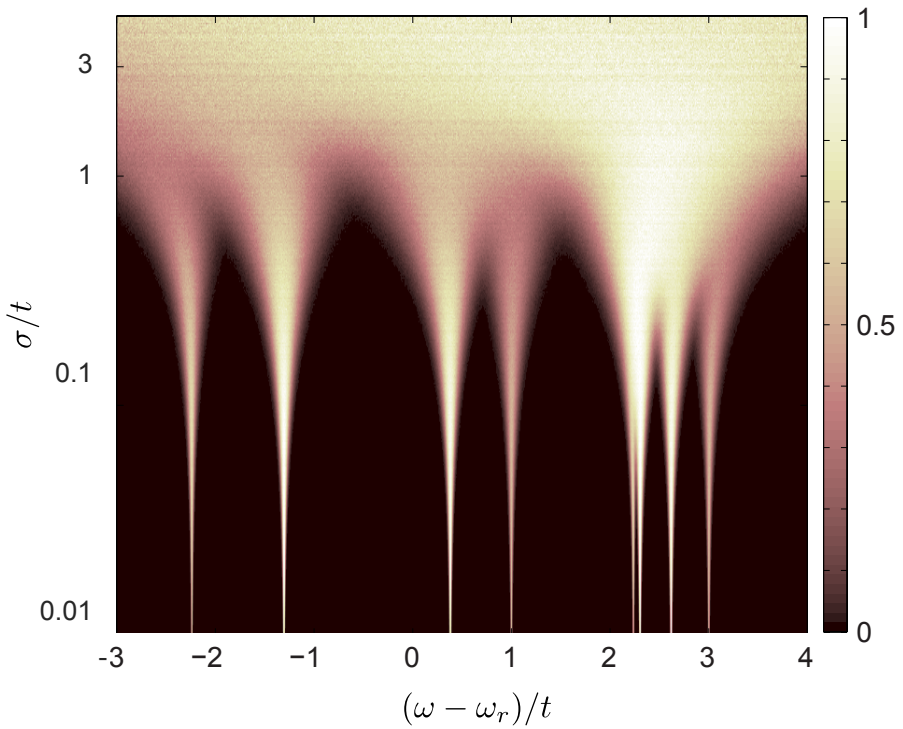

Figure 4.5: (Color online) The normal mode histogram in the presence of disorder. Normal mode frequencies are calculated from equation (4.12) using a set of $\{\delta_i\}$ drawn from a Gaussian distribution with standard deviation σ. For each value of σ, this procedure is repeated 10^7 times. Histograms are generated from 10^7 disorder realizations (for each value of σ), and are normalized to the maximum number of counts for clarity. For $\sigma \gg t$, the histogram is dominated by disorder and forms a single Gaussian. For $\sigma \ll t$, the histogram shows sharp peaks corresponding to the ideal normal mode frequencies.

approaches a single Gaussian of width σ from which the overall disorder of individual resonator frequencies can be extracted. For this reason, devices with a small hopping rate t are ideal for discerning the effects of disorder.

4.5 Kagome Star Device

By design, each coplanar waveguide resonator had a frequency of $\omega_r/2\pi \approx 7\,\text{GHz}$, and an impedance $\text{Z}_0 = 50\ \Omega$. At the outer edges of the array, each cavity is capacitively coupled to a transmission line, resulting in a photon escape rate $\kappa = 4Z_0^2 C_{\text{out}}^2 \omega_r^3$ to the continuum (equation 3.54). This allowed for transport measurements through

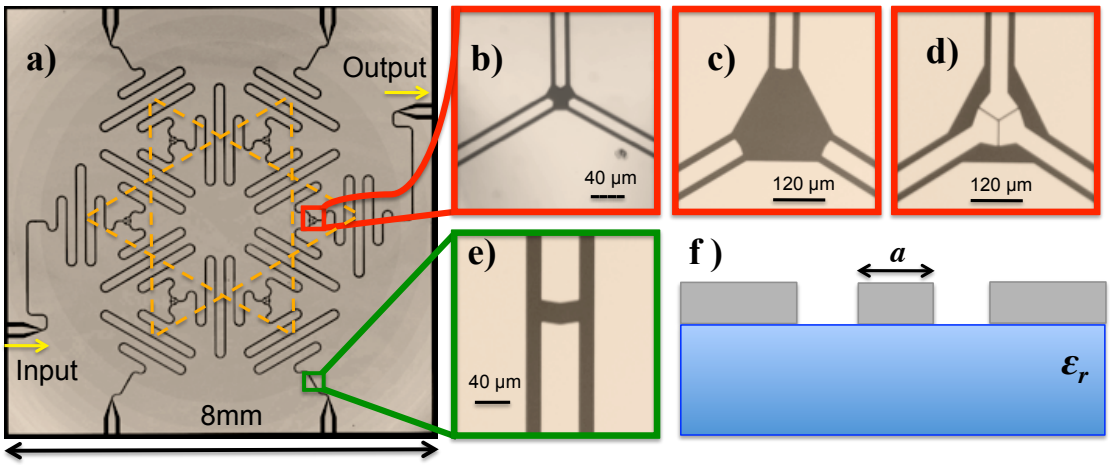

Figure 4.6: **a)** Device picture of twelve capacitively coupled resonators. The overlaid orange dashed lines have been drawn between the coupled resonators and illustrate how the photonic lattice sites form a single kagome star. Transmission was measured between the ports labeled "Input" and "Output".**b,c)** Images of symmetric 3-way capacitors with low hopping rate ($t/2\pi = 0.8\,\mathrm{MHz}$) with $10\,\mu$m and $40\,\mu$m wide center pins. **d)** Capacitor with high hopping rate ($t/2\pi = 31\,\mathrm{MHz}$) and $40\,\mu$m wide center pin. **e)** Image of outer coupling capacitor ($\kappa/2\pi = 0.05\,\mathrm{MHz}$) for $40\,\mu$m center pin. **f)** Cross-section of coplanar waveguide resonator with center pin width a, on a dielectric substrate ε_r.

opposite ports (figure 4.6) of the array using a vector network analyzer. The unused ports were connected to $50\,\Omega$ terminators, though no significant difference was observed when the ports were left open. Each device was cooled to a base temperature of 20 mK inside a dilution refrigerator – a necessary requirement for future quantum simulations with small numbers of polaritons [61, 42, 38, 3, 43, 59].

Results for the set of 25 devices is summarized in Table 4.1, includes samples with two distinct hopping rates of $t/2\pi = 0.8\,\mathrm{MHz}$ and $t/2\pi = 31\,\mathrm{MHz}$, which were obtained from equation (4.13) by using values for the coupling capacitances determined using a finite-element calculation. While the high-t devices allow us to access $t \gg \sigma$ and are most useful for quantum simulation, the low-t devices are the better choice for characterizing disorder.

$t/2\pi$ (MHz)	a (μm)	$\sigma/2\pi$(MHz)	σ/t	# Measured
0.8	10	9.1 ± 2.8	11.5	13
0.8	20	3.9 ± 1.2	4.9	4
0.8	40	1.4 ± 0.8	1.7	4
31	40	1.3 ± 0.3	0.04	4

Table 4.1: Results extracted from 25 measured devices. Devices were characterized with two different photon hopping rates t and three different center pin widths a. The random disorder σ was extracted from peak positions of the transmission spectrum for each device. The disorder is observed to decrease for increasing a. The ratio σ/t is a metric of how the normal mode frequencies are effected by disorder. For the 40μm devices, σ is reduced to less that two parts in 10^4 of $\omega_r/2\pi$. All uncertainties are computed from standard deviation of individual measurements.

4.6 Disorder Analysis on Transmission Spectra

We extract normal mode frequencies from the peak positions in the measured transmission spectra (figure 4.7 **a)-c)**) in order to determine the disorder. To account for small systematic shifts in devices made in separate fabrication batches, all frequencies were expressed relative to the mean peak frequency of each spectrum, and normalized to t. For low-t devices, not all twelve peaks are always visible. Such "missing" peaks can be due to normal mode degeneracies (occuring in the ideal case), as well as normal modes with small or vanishing amplitude in either of the resonators coupled to the input or output port.

For low-t devices, analyzing the peak positions provides a systematic method for extracting σ from a transmission measurement. Specifically, the disorder strength can be extracted from the peak positions using:

$$\begin{aligned}\sigma^2 &= \left\langle \frac{1}{n}\sum_{i=1}^{n}\delta_i^2 \right\rangle \\ &= \left\langle \frac{1}{n}\sum_{i=1}^{n}\left(\Omega_i^{\mathrm{dis}} - \bar{\Omega}_i^{\mathrm{dis}}\right)^2 \right\rangle - \frac{1}{n}\sum_{i=1}^{n}\left(\Omega_i - \bar{\Omega}_i\right)^2, \end{aligned} \tag{4.14}$$

where $n = 12$ is the number of resonators in each sample, Ω_i and Ω_i^{dis} denote the twelve normal mode frequencies in the absence and presence of disorder (supplementary A.1).

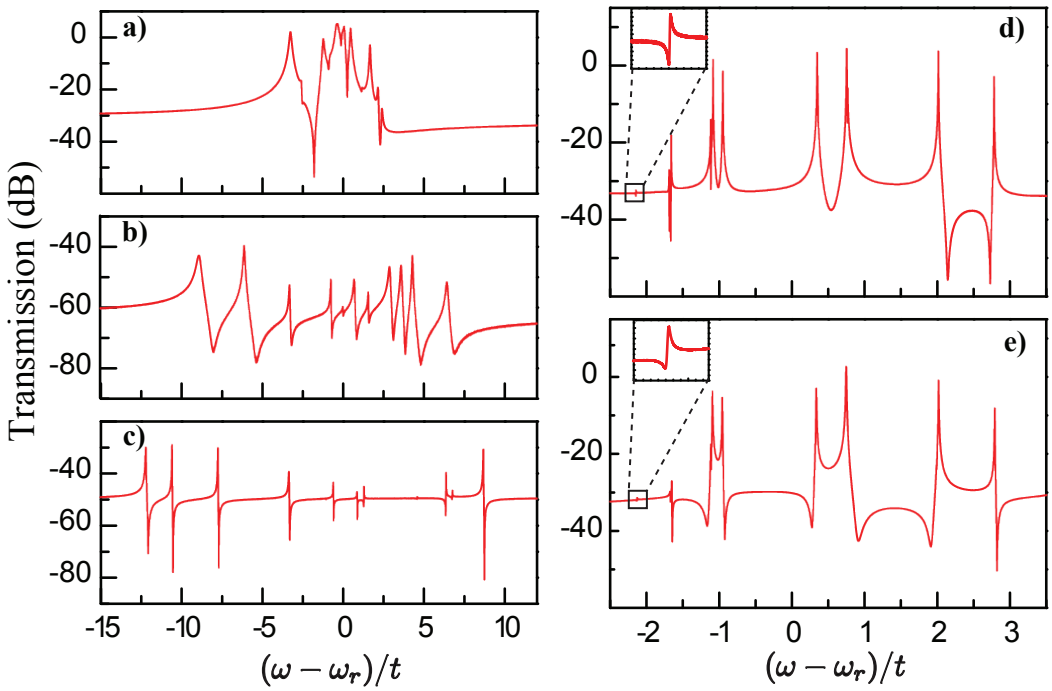

Figure 4.7: Transmission spectra for measured devices. The first column shows spectra for devices with **a)** $t/2\pi = 0.8\,\mathrm{MHz}$, $a = 40\,\mu\mathrm{m}$, **b)** $t/2\pi = 0.8\,\mathrm{MHz}$, $a = 20\,\mu\mathrm{m}$, **c)** and $t/2\pi = 0.8\,\mathrm{MHz}$, $a = 10\,\mu\mathrm{m}$. The width of the spectrum decreases for increasing resonator width, demonstrating a decrease in σ. The second column **d),e)** shows transmission spectra for two nominally identical devices with $t/2\pi = 31$ MHz and $a = 40\,\mu\mathrm{m}$. Each scan contains twelve well defined peaks that are consistent between the two devices. Peak positions are similar to those expected, when accounting for a systematic edge effect due to the difference between inner and outer capacitors. The inset shows the lowest energy mode that is localized on the inner six resonators in the absence of disorder.

Here $\bar{\Omega}_i$ and $\bar{\Omega}_i^{\mathrm{dis}}$ are their means (for a single disorder realization), whereas ensemble averages over disorder realization are denoted by $\langle\cdot\rangle$. In the disorderless case, the "variance" of the normal mode frequencies of the kagome star is $3t^2$.

Applying this method to samples with a standard $10\,\mu\mathrm{m}$ width of the transmission line center pin, it was found that the disorder $\sigma/2\pi = (9.1 \pm 2.8)\,\mathrm{MHz}$ was larger than expected from resonator length variations due to finite resolution in optical lithography. To investigate the origin of this disorder, devices were fabricated with different widths a of the center pin, while maintaining a constant Z_0. As a result a systematic dependence of disorder on a was discovered.

By increasing the center pin width devices with small disorder were found to be reproducible, subsequently four high-t (strongly coupled) devices were fabricated and studied. Transmission spectra for all four of these devices revealed very similar normal mode frequencies, confirming that disorder was small. Two representative transmission spectra are shown in figure 4.7 **d, e**. For all high-t devices, the lowest energy mode is significantly smaller in amplitude than the other eleven modes. In the absence of disorder, the lowest energy mode is localized to the six inner resonators and cannot be driven from any port. For the infinite kagome lattice, it is these localized states that lead to the known flat bands [59, 70, 69, 71]. Disorder in the array weakly breaks this localization and causes the mode to acquire a small amplitude in the outer resonators.

For high-t devices, σ is small compared to t and both variances on the right-hand side of Eq. (4.14) are large and nearly cancel each other. Consequently, an alternate method to extract σ in these devices is used. In devices where $t \gg \sigma$, the twelve peaks are easily identifiable in the transmission spectra and directly indicate the variation in individual normal mode frequencies. In this limit, the frequency Ω_j^{dis} of the j^{th} normal mode can be expanded to lowest order in the $\{\delta_i\}$ as

$$\Omega_j^{\text{dis}} = \Omega_j + \sum_i \frac{\partial \Omega_j}{\partial \delta_i} \delta_i. \tag{4.15}$$

The variance of this normal mode frequency with respect to disorder is then

$$\begin{aligned} \sigma_j^2 &= \left\langle \left(\Omega_j^{\text{dis}}\right)^2 \right\rangle - \left\langle \Omega_j^{\text{dis}} \right\rangle^2 \\ &= \sum_i \left(\frac{\partial \Omega_j}{\partial \delta_i} \right)^2 \sigma^2. \end{aligned} \tag{4.16}$$

The partial derivatives in equation (4.16) can be calculated numerically. Doing so, one finds that for each pair of degenerate normal modes the two normal mode frequencies

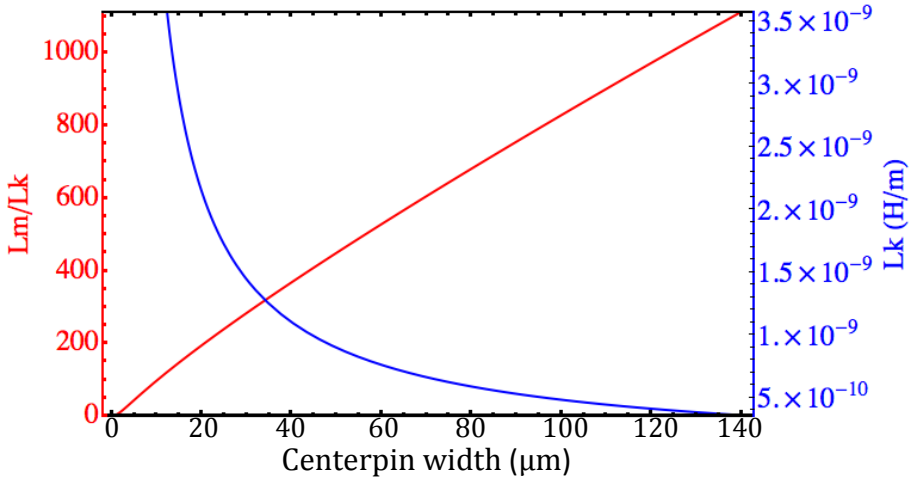

Figure 4.8: The magnitude of L_k is shown to change drastically for increasing a (blue), but the ratio L_m/L_k (red) is shown to increase 3 orders of magnitude, demonstrating that L_m is less sensitive to resonator geometry. Consequently for $\omega_r \propto 1/\sqrt{(L_m + L_k)}$ small changes in L_k result in significant changes in ω_r.

depend on mutually exclusive sets of the $\{\delta_i\}$. Thus, these two eigenfrequencies fluctuate independently about a common mean value. In order to estimate disorder σ from the measurements of the high-t devices, first the variance of the frequencies corresponding to each set of singly or doubly degenerate normal modes is calculated. Then, using equation (4.16), the variance is scaled by the sum of the squares of the partial derivatives to calculate an estimate for the disorder σ. Finally the average of the estimates for σ is found for all of the sets of normal modes, weighted by the order of the degeneracy of each set. Using this method, a $\sigma = (1.1 \pm 0.6)$ MHz is determined, which is well into the limit of $\sigma \ll t$.

4.7 Geometric Dependence of Kinetic Inductance

The magnitude of disorder decreases with increasing center pin width (figure 4.10). This dependence of disorder on the device geometry can be attributed to random variations in the width of the center pin that arise during microfabrication. These

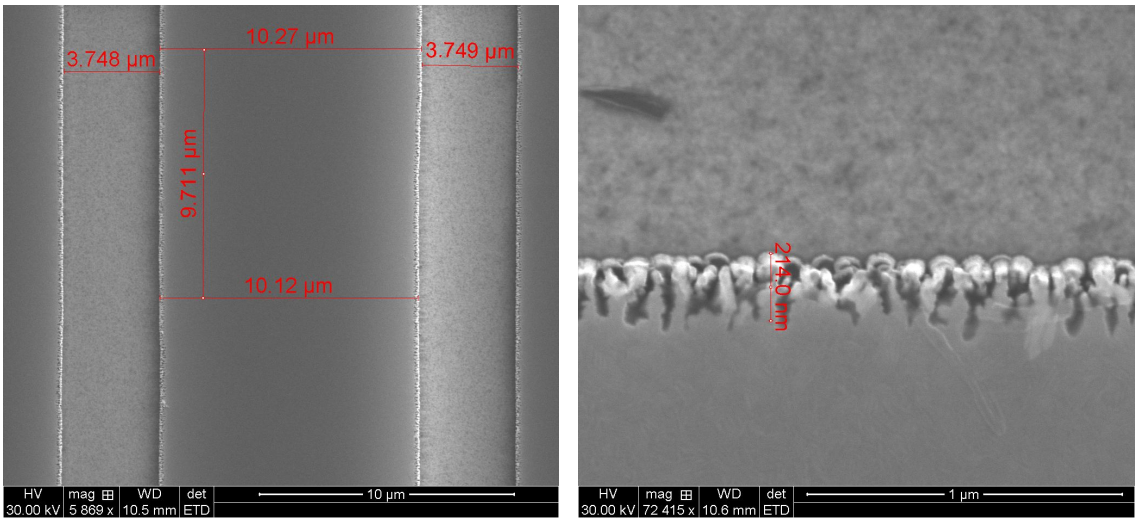

Figure 4.9: SEM image showing the undesired effects of the fabrication process. The features were designed to maintain a 50 Ω impedance, with feature sizes $a = 10\mu m$ and $s = 4.186\mu m$. The image on the left shows a measured centerpin width of $a = 10.27\mu m$ and a gap size $s = 3.749\mu m$. Deviations in the CPW feature sizes are understood to be the main source of frequency disorder in CPW lattices. The image on the left shows the serrated edges produced by the plasma etch process used to etch 200 nm of Nb (appendix B.2 for etch recipe). This is also considered to contribute to the effects of random disorder in these lattices.

variations in width result in variations in the kinetic inductance L_k, which in turn affects the resonator frequency through the relation:

$$\omega_r = \frac{1}{2\sqrt{(L_m + L_k)C_{\text{tot}}}} \tag{4.17}$$

where L_m is the intrinsic magnetic inductance and C_{tot} is the total capacitance. In normal metals, L_k is suppressed by electron scattering but in superconductors the DC electrical resistance is vanishing and L_k is no longer suppressed. A discussion on how to calculate L_m and L_k is presented in chapter 3.2.1.

Although L_k is more relevant in superconductors, it is still two orders of magnitude smaller than L_m, for the device geometry considered here; however, L_k is significantly more susceptible to geometric deviations than L_m (figure 4.8). For a single resonator, L_k typically only results in a small shift in ω_r [33, 32]. For arrays of coupled resonators,

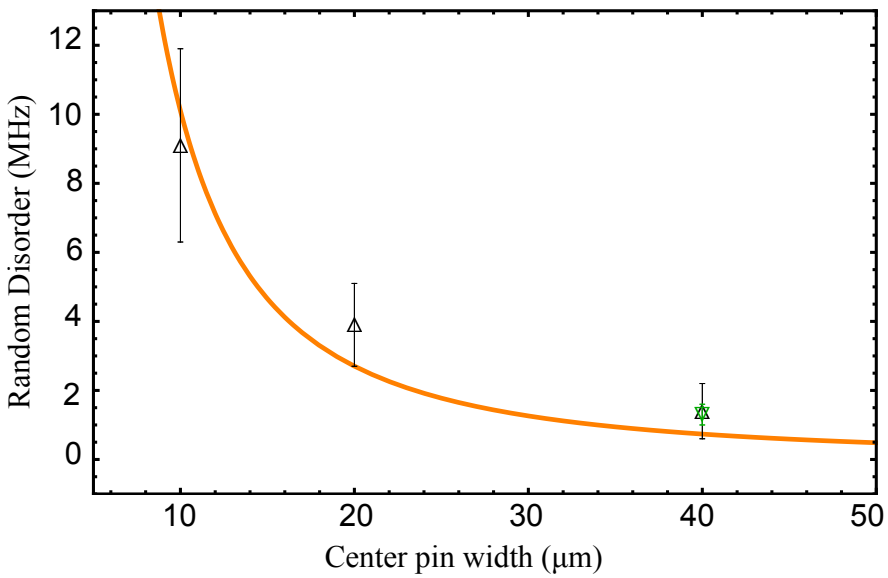

Figure 4.10: Random disorder versus center pin width for all devices. Disorder extracted from low-t devices is plotted in black with upward pointing triangles, while disorder extracted from high-t devices is plotted in green with a downward pointing triangle. The curve shows the difference in frequency for two resonators, one with center pin width equal to the value on the horizontal axis and the other with a center pin width 600 nm smaller and dielectric gap 1200 nm larger. Error bars are computed from standard deviation of individual measurements.

however, these small shifts can introduce significant disorder if the kinetic inductance contributions vary across the array.

For the small length scales used here, the sensitivity of the kinetic inductance to variations in a decreases rapidly as the width a is increased [104][1].

In the devices studied variations in the center pin width of up to ~ 600 nm were observed and twice that for the dielectric gap, when examining them with a scanning electron microscope. An example of this can be observed in figure 4.9 where the centerpin is seen to be $\sim$ 270nm different than the designed centerline width. The random disorder expected due to kinetic inductance variations can be estimated by comparing ω_r for cavities of equal length but with widths differing by the observed 600 nm, see figure 4.10. The random disorder observed here is consistent with varia-

[1]The expression for L_k from [104] is accurate for film thickness less than twice the penetration depth. It was used here to obtain a rough estimate for the geometric dependence of the superconductor

tions in device geometry and can be reduced to less than two parts in 10^4 by making resonators with 40μm wide center pins.

4.8 Summary

In this chapter the properties of the photonic Kagome lattice have been presented. Theoretically it has been shown how the band structure arises from a simple tight binding Hamiltonian, and also that transport measurements on a lattice of 219 sites behave according to the expected tight binding calculations. It was also shown that by reducing the size of the lattice to a single Kagome star it was possible to systematically study the source of disorder in these lattices. It was shown that the kinetic inductance was very sensitive to the geometry of the transmission line resonator, and that increasing the feature sizes reduced the effects of undesirable disorder to less than a few parts in 10^4 [100].

These photon lattices open the door for future experiments looking for quantum phase transitions and other many-body photon effects in coupled cQED arrays, and reliably fabricating these photon lattices is an important first step towards realizing a functional quantum simulator. The Kagome lattice is an ideal choice for such experiments, because it has a long history of theoretical proposals for being used as a model lattice for a quantum simulator. Furthermore the naturally occurring frustration in the Kagome lattice could lead to new proposals for studying the physics of interacting polaritons in dispersionless bands. Addiotionally, with random disorder sufficiently reduced future experiments with cavity arrays could be used to study localization effects by adding controlled amounts of disorder [2, 92].

Chapter 5

Scanning Probe Microscopy on a Kagome Lattice

5.1 Introduction

In this chapter a perturbative scanned probe microscopy (SPM) method is presented that is used to observe the internal mode structure of microwaves within a 49 site Kagome lattice. This perturbative method provides a means of gaining insight about interior lattice sites, while only measuring transmission from edge resonators. By positioning a small piece of dielectric above the surface of a single lattice resonator,

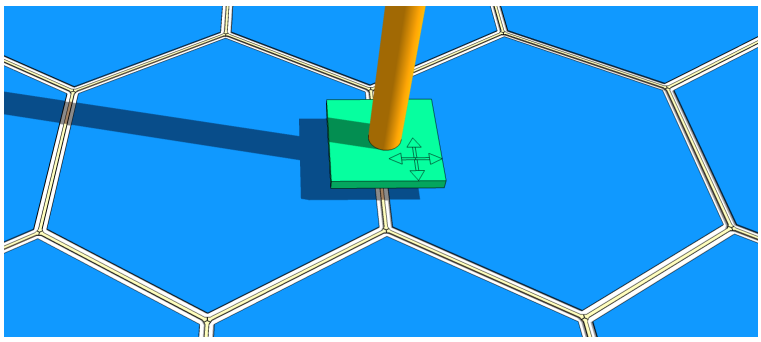

Figure 5.1: Illustration of the perturbative scanning microscopy experiment on a lattice of microwave resonators. The green square is the scannable defect above a lattice of coplanar waveguide resonators.

the frequency will change forming a local defect, furthermore adjusting the position of the dielectric will allow for tunability of the defect size. The shift in resonance at a single site will result in a measurable frequency shift of modes that have weight at that site, with the magnitude of the shift proportional to the strength of the field.

It is worth noting that similar perturbative measurement techniques have been used to characterize higher order modes in large RF cavities for accelerators [6, 37, 67]. These experiments are referred to as bead-pull experiments, and it has this name because in the experiment a dielectric bead is pulled on a string through a 3D RF cavity. The resonances of the cavities can thus be characterized by measuring the frequency shift as the bead is pulled through the cavity. Furthermore perturbative scanning measurements have also been used to study mesoscopic physics, where the coherent flow of electrons in a two dimensional electron gas was measured by using an AFM cantilever probe to perturb the flow of electrons near a quantum point contact [28, 99].

The chapter begins by discussing some technical details of the experiment; the scanning stage, the type of defect used to perturb each lattice site, the Kagome lattice used in the experiment, and the basic movement of the probe. Next the results from a calibration experiment will be presented. The goal of the experiment was to understand how the probe effected the resonant frequency of a coplanar waveguide resonator, and to quantify the response of the resonator as a function of the height of the probe. Subsequently the experiment where the defect is scanned over a Kagome lattice of resonators will be presented. First navigating the probe relative to the lattice features will be discussed, followed by a detailed treatment of how the mode weights were accurately extracted from the experimental data. Finally the measured mode weights of three different normal modes will be presented, and compared to theoretically predicted mode weights.

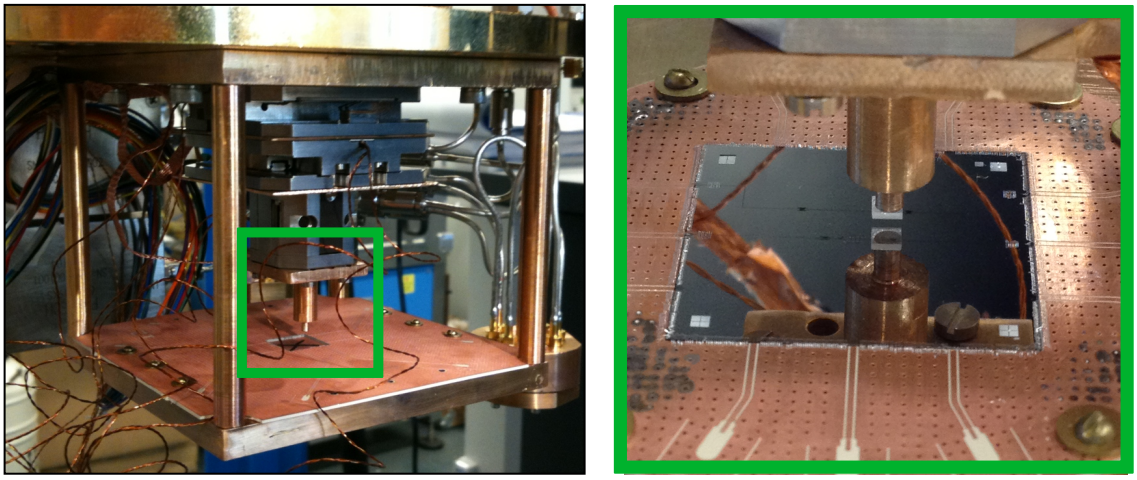

Figure 5.2: On the left a stack of three cryogenic linear nano-positioners mounted to a gold plated copper frame, that is mounted to the bottom of a Bluefors dilution refrigerator. The positioner at the bottom of the stack (ANPz101/RES) provides Z movement with a working distance of 12 mm. The two linear positioners (Attocube ANPx340/RES) at the top of the stack provide XY movement and have a working distance of 20 mm. In order to reduce the heating after movement, gold plated copper plates are mounted between each positioner, and are also mechanically clamped to copper braid that is then secured to the bottom of the dilution refrigerator. On the right is a zoomed in picture of the square piece of sapphire glued to a gold-plated copper rod. The sapphire defect was glued using MMA (methyl methacryllate) ebeam resist. The defect is pictured above a single coplanar waveguide resonator that is used for defect calibration.

5.2 Experimental setup

The defect consisted of a 2mm x 2mm epipolished sapphire wafer that was glued to a copper rod, and then mounted to a three axis nano-positioner scanning stage. In figure 5.2 it can be seen mounted to the copper stage above a single straight resonator. The defect was designed to be much wider than the center pin of the resonator, but shorter than the length of a single resonator. This ensured that the defect would cover the entire center pin but, would not overlap with multiple resonators.

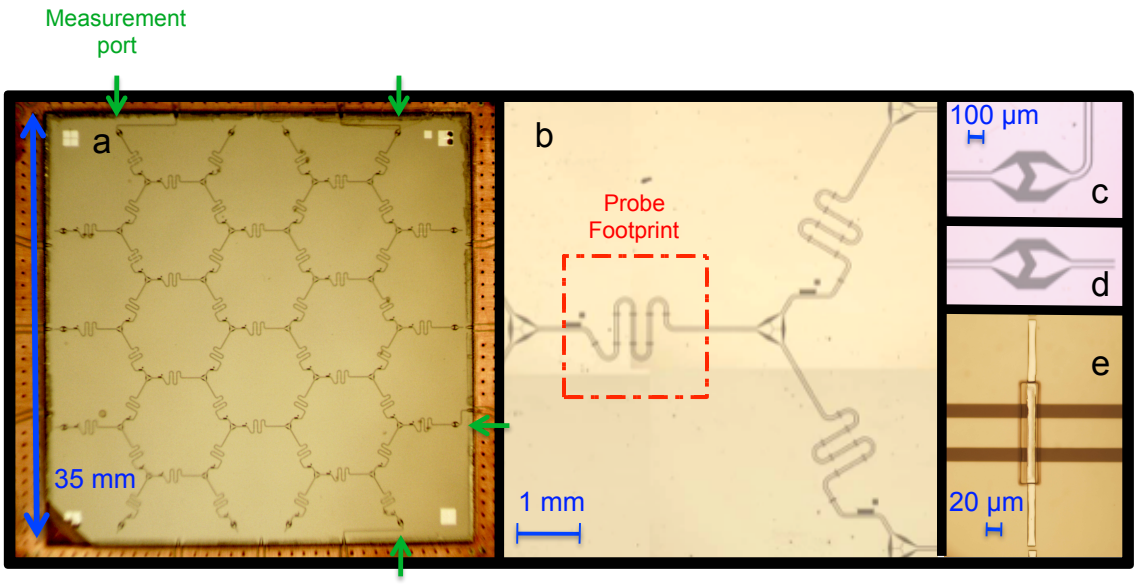

Figure 5.3: **a** The lattice was design was previously discussed in section 3.4.1. A large lattice was fabricated so that it would be easier to probe a single site without interfering with other sites. **b** The lattice unit cell. For all measurements the sapphire probe was centered over the meandering region. While no qubits were used during the experiment, the resonators were designed to be qubits could be easily integrated into the lattice. **c** Edge resonator capacitor coupled to transmission line for measurement. **d** Edge resonator capacitor coupled to quarter wavelength resonator detuned to $10\nu_r$. Here only four edge resonators were coupled to transmission lines for measurement (indicated with green arrows). The number of measurement ports were limited by the wiring within the dilution refrigerator. **e** The BCB supported crossover that connected isolated ground planes.

5.2.1 Kagome lattice for scanning

The lattice used for scanning contained 49 resonators, with each resonator designed to have a frequency of $\nu_r = 7.48$GHz, a nearest neighbor hopping rate of $t_{i,j} = 100$MHz, and an edge resonator escape rate of $\kappa = 300$kHz. The lattice was fabricated using photolithography on 200nm of sputtered Nb on a 500μm thick sapphire substrate (figure 5.3). Isolated ground planes within the lattice were connected with 300nm aluminum bridges evaporated on top of a 4μm thick pad of bisbenzocyclobutene (BCB); a very low loss dielectric [68]. Supported cross-over connections were used instead of wirebonds to prevent shorts to ground when the scanning probe was brought into contact with the surface. The device was mounted to a copper PCB using high-

performance silver paste, and wirebonds were used to ground the outer edges of the lattice, and connect to measurement ports.

5.2.2 Probe movement

To begin each experiment, the probe was slowly moved into mechanical contact with the surface of the device. Once in contact, moving the probe laterally consisted of an up-over-down sequence per step; always ending a step with the probe in mechanical contact with the surface of the device. A transmission measurement was made after each step in order to observe changes in the spectrum. The changes in transmission spectrum were then used to gauge the relative position of the probe. For each lateral up-over-down step sequence, the movements consisted of 100µm up, 100µm over, and 110µm down; ensuring good mechanical contact.

The length of the over step determined the accuracy of the probe position, but due to the large feature sizes of the lattice and the large size of the sapphire probe, 100µm position uncertainty was more than sufficient. Each lateral step heated the dilution refrigerator from 15mK to over 90mK and would take several minutes to settle to base temperature. Measurements were taken between 35-40mK in order to reduce wait times, and while the lattice without qubits did not require such low temperatures, all measurements were performed at the same temperature for consistency.

5.3 Defect Calibration

When the defect is positioned above the resonator the effective dielectric constant ϵ_{eff} of the resonator will change, resulting in a change in resonant frequency $\omega_r = \frac{c}{\sqrt{\epsilon_{eff}}\ 2l_{res}}$. An analogous way to consider this is that the capacitance per unit length, C will change as a result of the defect; this will change the resonant frequency, $\omega_r = \frac{1}{\sqrt{CL}l_{res}}$ in a similar way. In section 3.2.1 it was shown that C is proportional to ϵ_{eff}.

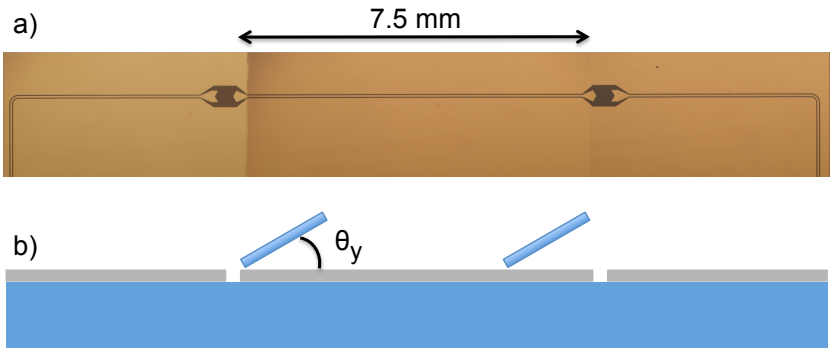

Figure 5.4: **a** A straight resonator used for defect calibration. For this experiment the probe was centered over the resonator, then starting from one capacitor it was moved across the resonator in 100μm steps. After each step a transmission measurement was made. bfb Cartoon illustration of misalignment between the probe and the resonator. This type of misalignment resulted in asymmetric coupling to the probe near the capacitors.

Therefore both of these interpretations provide an intuitive picture for the effects of the perturbing a resonator, and are accurate as long as the entire resonator is covered by the defect. However, it was discovered that these expressions do not accurately describe the situation when the resonator is only partially covered. Consequently other numerical methods were necessary to quantify the effects of the resonator. In order to verify the numerics, a calibration experiment was performed, and the results were compared to simulations from a finite element software package, Ansoft HFSS (High Frequency Structural Simulator).

5.3.1 Frequency shift vs probe y-position

A single transmission line resonator with no meandering lines was used to calibrate the effect of scanning a dielectric probe over the surface of a resonator (figure 5.4 a). The resonator was 7500μm in length, had an unperturbed resonant frequency of $\nu_r = 8.2$ GHz and a cavity decay rate of $\kappa = 2$ MHz. In order to fully calibrate the effect of the sapphire probe, the frequency response of the cavity was measured for 92 different

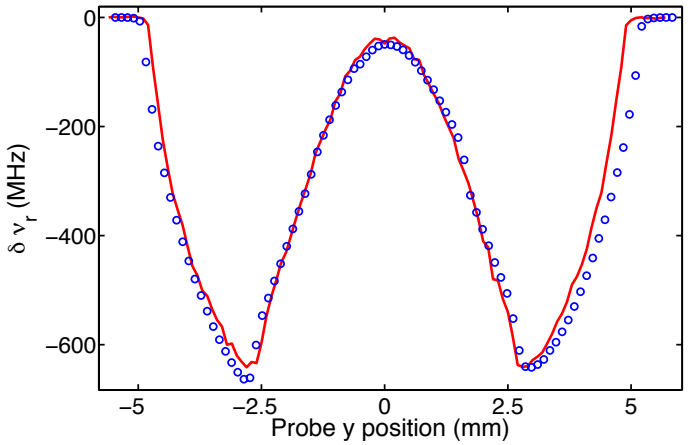

Figure 5.5: The measured frequency shift of a long straight transmission line resonator, at different probe positions along the transverse axis of the resonator. At each position the probe is centered over the resonator and is in mechanical contact. The curve was produced by an HFSS simulation for a flat probe that is 2μm above the surface of the resonator. This height difference between experiment and simulation is related to the asymmetry at maximum shifts and is understood to be the result of probe tilt (figure 5.4 b). The symmetric shifts about the center of the resonator are expected for a $\lambda/2$. Here the maximum shifts occur when the edge of the probe is directly above the edge of the capacitor, and the probe couples most strongly to the field inside the cavity. When the probe is centered over the resonator, it is only weakly coupled to the field inside the cavity.

probe positions. The spacing between each probe position was 100μm, and the probe was centered over the resonator in mechanical contact for each measurement.

In the measured frequency shift, a sinusoidal dependence was observed as a function of the probe position (figure 5.5). This behavior is expected for a $\lambda/2$ resonator, because the electric field amplitude is at a maximum near the capacitors and zero at the center. As observed, the frequency of the resonator was most drastically effected when the probe was strongly coupled to the field in the resonator. A maximum shift of 680MHz occurred when the probe was above one end of the resonator, and a minimum shift of 80MHz was observed when the probe was centered over the resonator. As seen in figure 5.5, the agreement between the measured frequency shifts and the HFSS calculation show very good agreement, validating the use of this software package.

A 22MHz asymmetry between maximum shifts was observed and is understood to be caused from misalignment between the probe and the resonator (figure 5.4 b). Misalignment angles of $\theta_{\parallel} \sim 0.02$deg and $\theta_{\perp} \sim 0.06$deg, were determined by comparing measurements to finite element simulations (figure 5.6 a). The misalignment is understood to result from the adhesive used to glue the sapphire to the copper rod, and also the conductive paste that was used to secure the resonator to the copper circuit board.

5.3.2 Frequency shift vs probe z-position

By adjusting the vertical separation between the resonator and the probe, the resonant frequency can be tuned in a controlled manner. On a single resonator the change in resonant frequency can be measured directly, but in a large lattice the change in frequency when one site is perturbed does not directly provide the frequency shift as a function of height. In order to determine the shift in resonance of a lattice resonator, a calibration metric was developed from the measurements on the single resonator. The probe was positioned near a field maximum, then from contact was moved vertically away in 2μm steps. After each step a transmission measurement was made.

The shift as a function of probe z-postion ($\delta_r(z)$) for single resonator was analyzed and a 'best fit' function was used to describe the observed shift. The function was a second-order rational function of the form

$$\delta_r(z) = f(z) = \frac{a}{z^2 + bz + c} + d, \tag{5.1}$$

where a, b, c, and d are free fit parameters. An HFSS calculation was also done to model the probe z-position and demonstrated a similar curvature (figure 5.6 a). However, curve for the measured shift and the curve for the HFSS calculated shift

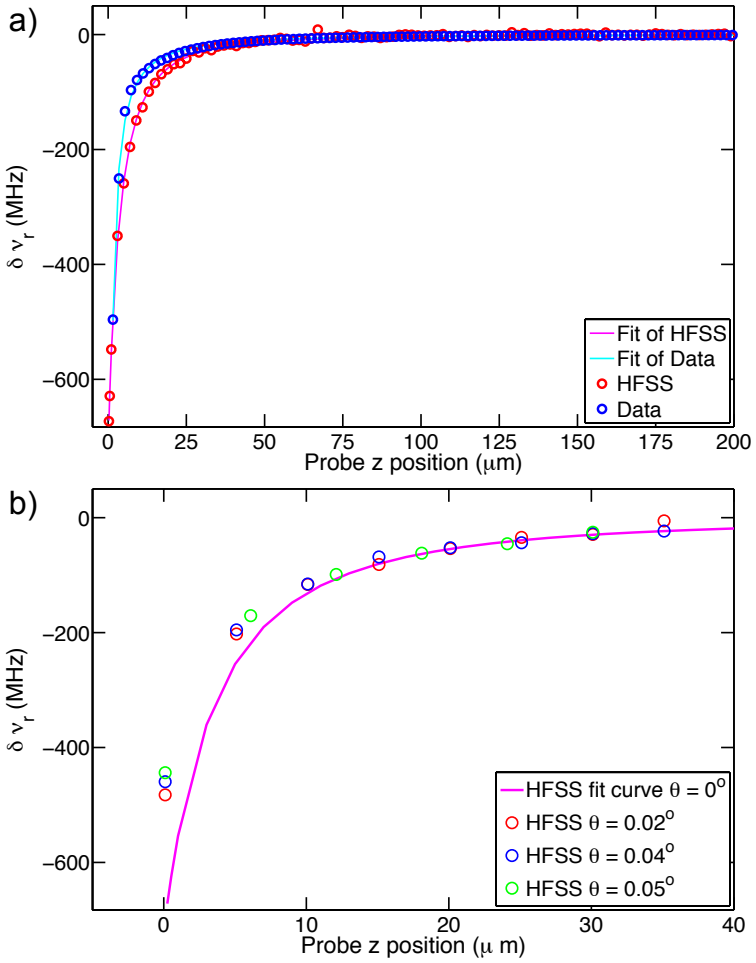

Figure 5.6: The shift of a single transmission line resonator is plotted as a function of the vertical position of the dielectric probe. For both measurement and simulation the edge of the probe is positioned 446μm from the edge of the capacitor. The edge of the capacitor is considered to be the probe position at maximum shift. **a)** The contact z-position of the measured frequency shift was adjusted to be 1.5μm in order to align the data with the simulation. The fit function was applied to measurement and simulation demonstrating the validity of the fit. The divergence at intermediate probe heights is not well understood, but is considered to be due to a combination of probe misalignment and error in the probe position. The coefficients used in the fits were; for the measured data: a = -52.636, b = 57.148, c = 16.216; for the HFSS data: a = -44.398, b = 17.512, c = 61.654. **b)** Simulations for a tilted probe at the same 446μm probe position. At higher tilt angles the frequency shifts at low z-positions are significantly smaller. The contact z-position can be explained by a probe with misalignment angle $\theta = 0.02$deg.

showed a slight deviation in curvature between 8μm - 30μm. This is understood to be due to misalignment between the probe and the resonator (figure 5.6 b).

5.4 Scanning the probe over the Kagome lattice

In the transmission spectrum for an unperturbed lattice a large family of peaks is observed in a bandwidth of $\sim$ 600MHz; close to the theoretical bandwidth of $6t_{ij}$. This spectrum is measured from two non-adjacent edge resonators, and only captures modes that have a measurable weight in those edge resonators (figure 5.7 a). When a single site is perturbed modes with weight at that site will shift an amount proportional to the weight. For each interior lattice site one of the flatband modes will have the most weight, and therefore the largest shift. For a negatively detuned lattice site, this will cause the flatband mode to shift well below the observed bandwidth (figure 5.7 b).

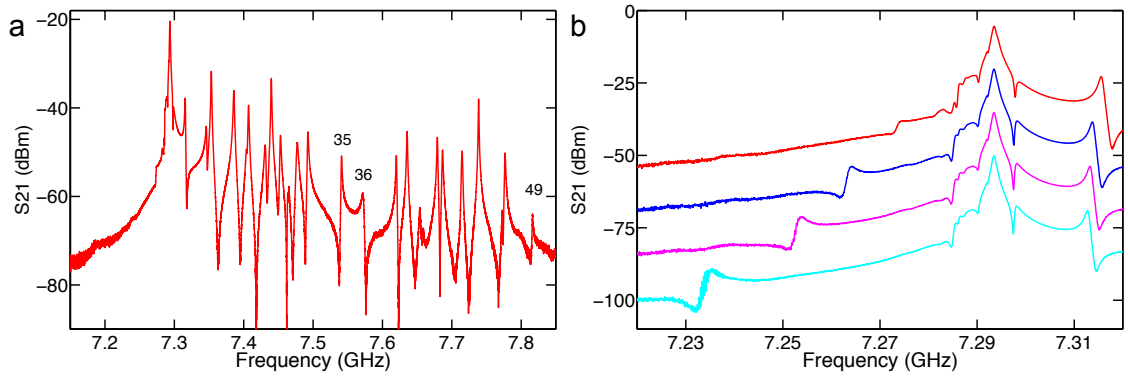

Figure 5.7: **a** Transmission spectrum for a Kagome lattice of 49 resonators. Here the three numbers (35, 36, 49) illustrate the three modes that were tracked while perturbing each lattice site. **b** Measured transmission at the bottom of the frequency band for five different probe positions. Each transmission trace was separated for clarity. The flatband mode is shown to shift $\sim$ 55MHz from it's unperturbed frequency. For each interior lattice site the flatband mode was observed to have the largest frequency shift. The probe positions above the resonator from top to bottom were: $z = 241.93\mu$m, $z = 17.19\mu$m, $z = 12.96\mu$m, and $z = 8.73\mu$m.

5.4.1 Probe position calibration

In order to center the probe over each resonator, and to accurately quantify the effects of the probe for each resonator, it was necessary to determine the position of the probe relative to each lattice site. The X and Y positions of the probe relative to the scanning stage could be determined by measurement of the resistive position encoders integrated into the Attocubes; however these position readings did not directly translate to lattice coordinates, and further calibration was necessary in order to center the probe. The probe position relative to the a given lattice site was determined by monitoring the shift of the flatband mode. The probe could be accurately centered in X and Y by moving the probe off of a resonator onto the ground plane, and also by moving the probe onto a three-way coupler and then back off (figure 5.8).

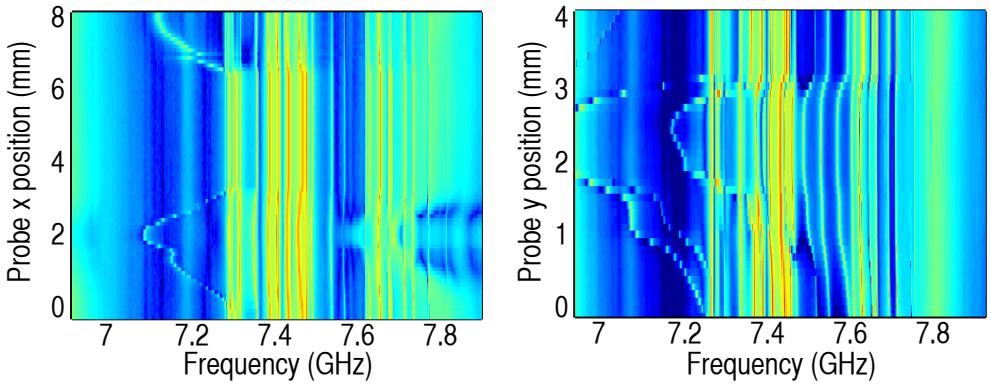

Figure 5.8: Here transmission measurements are shown for transverse probe movement. Each measurement is made when the probe is in mechanical contact. a) Starting on a ground plane, the probe is moved across one lattice resonator, traverses a large ground plane, and then stops centered on different lattice resonator. Here a significant shift in the lowest frequency mode is observed when the probe is in contact with a resonator. When the probe is in contact with the ground plane there is no observable shift. The shift of the lowest frequency mode indicates when the probe steps onto a lattice resonator and this position is known within 100μm; the uncertainty is determined by step size used. b) Starting at the edge of a three-way coupling capacitor, the probe is moved across the capacitor, then off the capacitor and onto a lattice resonator. When the probe covers a three-way capacitor three different lattice sites are simultaneously perturbed resulting in multiple modes shifting down in frequency. The modes shifting back up in frequency indicates the probe is no longer covering the capacitor, and the position of probe relative to the capacitor can be determined within 100μm.

When the probe is positioned above the ground plane no frequency shifts are observed. By moving across a resonator from one ground plane to another, it was easy to establish when the probe was centered over the resonator. When the probe is positioned over a three-way coupler, multiple sites are perturbed and the frequency spectrum changes significantly. By observing when the probe moved off of the three-way resonators, the edge of the resonator could be established by observing when the multiple modes stopped shifting.

5.4.2 The z-scan; tuning the defect size

At each lattice site the probe was first centered over the resonator, moved into contact, and then moved vertically away from the surface. When in contact, calculations indicate the probe to be $\sim 4\mu$m above the resonator, approximately the same height as the BCB supported bridges. The probe was retracted from contact with a 0.8μm step size up to $\sim 20\mu$m, and then a 10μm step size up to $\sim 300\mu$m. Transmission measurements were made at each probe position (figure 5.9). When in close proximity to the surface large frequency shifts > 300MHz are generated, but at probe heights $\geq 200\mu$m, the frequency shifts per step are small and the shifted resonant frequency will asymptotically approach the unperturbed resonant frequency (figure 5.11).

5.4.3 Probe z-position error bars

The uncertainty in the probe position stems from the accuracy of the reading of the resistive encoder on the nano-positioner; this uncertainty is more critical for Z position measurements. The position is determined by applying a constant voltage to the nano-positioners, and measuring a calibrated resistance. The accuracy of the reading is proportional to the amplitude of the applied voltage, but larger voltages would result in heating of the dilution unit. Consequently a voltage was chosen such

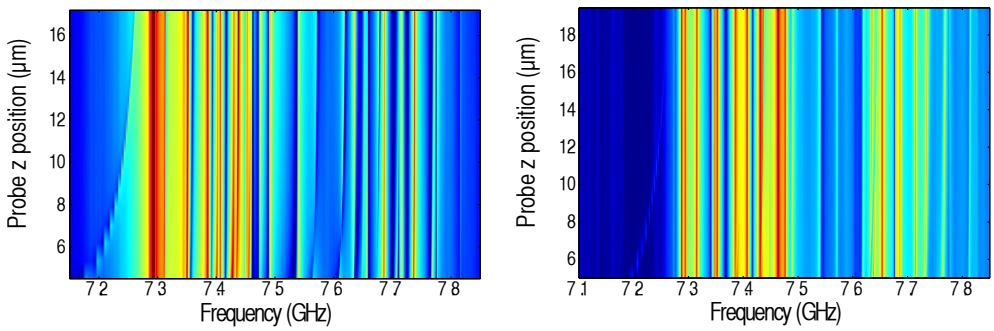

Figure 5.9: Starting in contact the probe is vertically moved away from the surface of a resonator in the Kagome lattice. Here measurements for two different interior lattice sites illustrating the response of the modes for different probe heights. The most notable shift is the lowest frequency flatband mode. These measurements only show the first set of probe position measurements, where the step size is 0.8μm per step.

that the fridge wouldn't heat up, and the position measurements were accurate up to $200nm$.

The experimental uncertainty in the probe position was extracted from a linear fits of position of the readings; the uncertainty was the standard deviation of the fit (figure 5.10). For measurements conducted during the scanning lattice experiment, the results were in the form of a shift in frequency as a function of probe height. From the calibration metrics, the probe height was converted to resonator detuning, and the uncertainty in the probe height was converted to uncertainty in detuning using propagation of errors and taking a numerical derivative of equation 5.1 .

$$\sigma_d^{\text{exp}} = \sqrt{\left(\frac{\partial f}{\partial z}\right)^2 \sigma_z^2} \tag{5.2}$$

Additionally there was an uncertainty in the numerical simulations used to convert the probe position to defect shift. This uncertainty resulted from using a reduced the computational mesh in order to reduce the computational time for the HFSS calculations. The uncertainty was determined by running multiple simulations with the probe at a fixed position and calculating the standard deviation measured frequency

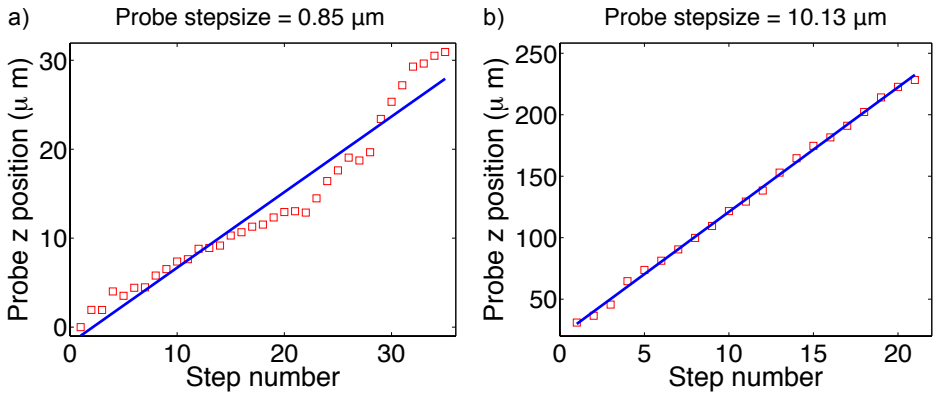

Figure 5.10: The uncertainty in the Z position of the probe is determined from the standard deviation of a linear fit to the attocube position readings. Additionally the experimental stepsize was determined from the slope of the linear fit. After the probe is centered over the resonator it is moved out of contact. For these measurements two step sizes are used **a)** when the probe is close to the surface of the lattice, smaller step sizes are used, and the uncertainty in the probe position is more prevalent. **b)** After the probe is far enough from the surface, a larger step size is used, and the uncertainty in the position reading is not as prevalent.

shifts. The resulting uncertainty was $\sigma_d^{\text{sim}} = 1.57\text{MHz}$, and the total uncertainty in the determined defect is given as

$$\sigma_d = \sqrt{(\sigma_d^{\text{exp}})^2 + (\sigma_d^{\text{sim}})^2} \ . \tag{5.3}$$

5.5 Photon modes in a Kagome lattice

In the experiment each lattice site was perturbed, and the size of the perturbation was tuned by bringing the probe into contact and then vertically moving the probe away from the resonator until the modes stopped shifting. For each perturbed resonator the 35^{th}, 36^{th}, and 49^{th} modes were tracked, and the shift each of these modes was analyzed and used to determine the distribution of the modes within the lattice.

The 35^{th}, and 36^{th} modes are the two modes nearest to the dirac point at $\omega_r + t$, and the 49^{th} mode is the highest frequency mode. Each mode had a large spacing between adjacent modes, and did not overlap with other modes when perturbed by the

probe; resulting in hard to handle mode degeneracies. In addition to the modes being in low density regions, the modes were easily identifiable for theoretical comparisons.

In order to track the three modes, a Lorentzian fit was applied to each mode, for each probe z-position. The frequency shift of each mode was determined by subtracting the frequency determined by the fit from the frequency at the highest probe height. This method provided the mode frequency shift as a function of the probe's z-position, but a more arduous method was necessary to determine the defect size $\delta_r(z)$.

5.5.1 Mode shift vs defect size

For a defect at a single site, the allowed energies of the lattice followed a modified tight binding hamiltonian ($\hbar = 1$),

$$H(z) = \sum_i (\omega_r + \tfrac{1}{2}) a_i^\dagger a_i + \delta_r(z) a_k^\dagger a_k + \sum_{j>i} t_{ij}(a_j^\dagger a_i + a_i^\dagger a_j) \tag{5.4}$$

where $\delta_r(z)$ is the defect size as a function of the z-position of the probe at site k. The value of $\delta_r(z)$ is determined numerically by an HFSS simulation, and by using equation 5.1 to fit the simulation results. For each lattice resonator an HFSS simulation was conducted for different probe z-positions, but since a full lattice simulation was not feasible, each lattice site was modeled as a single two port resonator; similar to the calculations presented in section 5.3.2.

The interior resonators were modeled such that the capacitors had a cavity escape rate of $2t$ at each end, and edge resonators were modeled to have an escape rate of κ on one end and $2t$ on the other. For each simulation the probe was positioned above the resonator based on probe positions extracted from the position calibration measurements (section 5.4.1). Due to the long computational time necessary for accurate simulations, probe heights were only simulated from 10nm to 20.01μm with

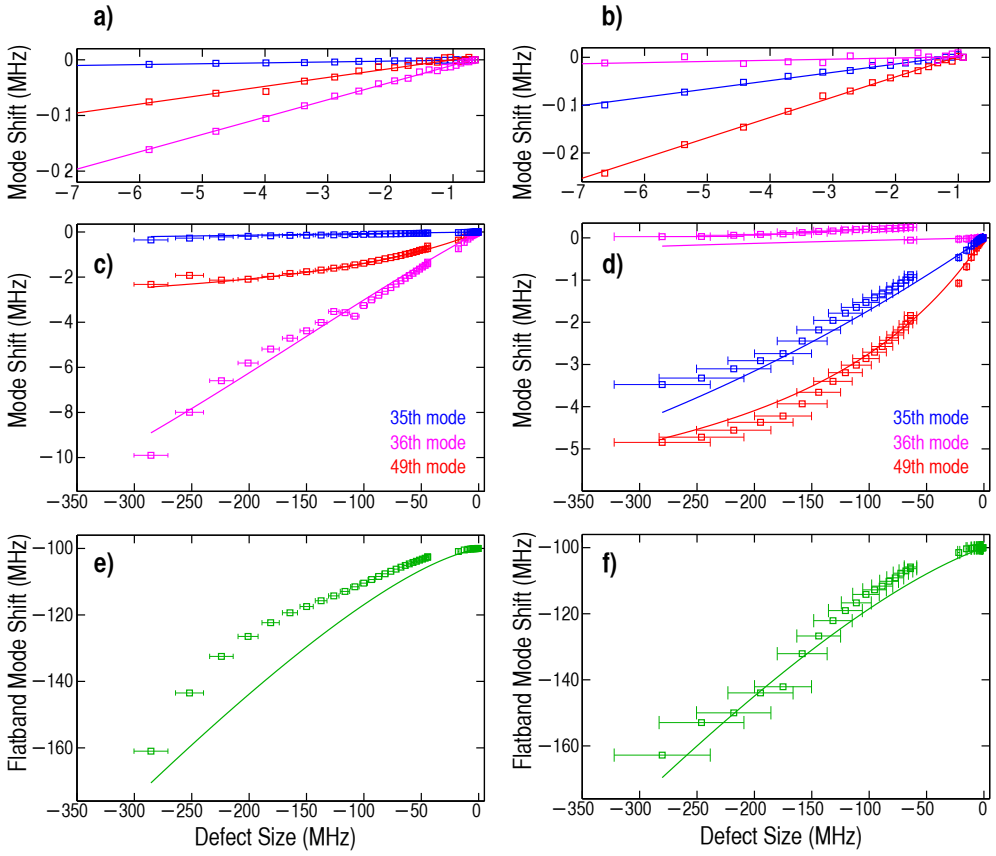

Figure 5.11: Measured and expected normal mode shifts as a function of the Defect size for two different interior lattice sites (left stack is all one lattice site, and right stack is another). **a)**, **b)** The small defect limit for three measured normal modes at different interior lattice sites. Each mode is plotted along with a linear fit, demonstrating the linear dependence of the mode shift for small defect sizes. Experimental weights are determined by extracting the slope from the linear fit in this limit. **c)**, **d)** In the large defect limit modes with more weight at that site produce a large nonlinear shift. Additionally modes with little weight continue to shift linearly. Each curve is the expected shift based on tight binding calculations with equation 5.4. Error bars represent the propagated uncertainty in the probe position (section 5.4.3). Gaps in the data for Defect size $\sim$ 50MHz are the result of changing the probe step size from 0.8μm to 10μm. **e)**, **f)** In a frustrated Kagome lattice each flatband mode is localized within an interior hexagon. When a lattice site on one of the interior hexagons is perturbed, the flatband mode within that hexagon will shift monotonically with the defect size. Additionally, for large perturbations the flatband will shift linearly with the defect size. Here experimental evidence of the flatband mode is presented along with the expected values. The shift of the flatband due to the perturbation was an order of magnitude larger than non flatband modes, and since these modes are degenerate, there is only one expected flatband frequency is the same. Discrepancies between experimental data in **e)** is understood to be caused by random disorder in the lattice.

2μm step size. In order to extrapolate δ_r to higher z-positions, the functional form of $f(z)$ was determined from the fit results on the single resonator measurements, and a the simulation results at each site were fit using an updated expression of the form $\delta_r(z) = a_k f(b_k z)$, where a_k and b_k are fit parameters unique for each lattice site k.

The measured frequency shift for each of the three modes were plotted as a function of the simulated results for $\delta_r(z)$. Using the same $\delta_r(z)$, the equation 5.4 was diagnolized and the resulting eigenvalues were also plotted demonstrating good agreement between experiment and theory (figure 5.11). The discrepancies in the flatband data are believed to be the result of random disorder in the lattice. The flatband modes are most susceptible to disorder, and the effects are a change in the shape of the mode shift as a function of defect size.

5.5.2 The measured mode weights

At large probe heights the size of the perturbation is small, s.t. $|\delta_r/\omega_r| \ll |\delta_r/t_{i,j}| \ll 1$, and the normal modes will shift linearly with the size of the defect (figure 5.11 a,b). In this small perturbation limit a first order approximation can be used, and the mode shift δ_μ as a function of the size of the perturbation δ_r is equal to the normalized

Mode No.	S.O.W.	Percent error	M.S.E
35	0.991	0.009	0.011
36	0.996	0.016	0.010
49	0.981	0.045	0.008

Table 5.1: Error analysis for the experimentally measured weights of the three normal modes. At each lattice site the mode weight was extracted from a linear fit of data for $\delta\nu_\mu$ vs $\delta\nu_r$. The extracted weights are naturally normalized and the sum of weights (S.O.W.) should be 1. A theoretical S.O.W. was determined from a linear fit of expected values, and then used to determine the percent error in the experiment. The reported M.S.E. was determined as the average squared difference between the experimental and expected slope values at each site.

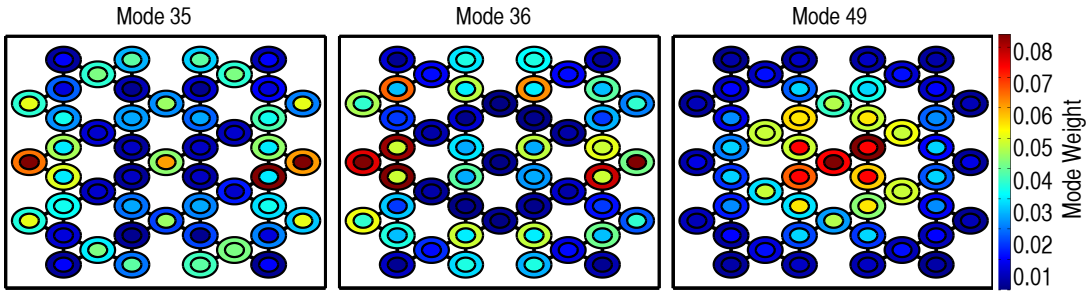

Figure 5.12: The photon distributions for the 35^{th}, 36^{th}, 49^{th} modes. Here the mode weights are plotted according to the Kagome lattice symmetry, and are quantified by the color, with red representing a larger percentage of the photon, and blue representing negligible percentage of the photon. Experimental results are represented by the larger circles and the theoretical results from tight binding calculations are represented by the interior circles. While there is some small discrepancies in the high probability regions, the low probability (regions where there shouldn't be photons) shows a very good agreement between experiment and theory.

weight of the mode,

$$\frac{\delta_{\mu,k}}{\delta_{r,k}} \simeq \langle \Psi^0_{\mu,k} | \Psi^0_{\mu,k} \rangle, \tag{5.5}$$

where μ is the mode index, k is the lattice site index and $|\Psi^0_{\mu,k}\rangle$ is the normalized normal mode eigenvector. In the linear limit the slope of the mode shift vs the defect size is equivalent to the mode weight. The experimental weight was determined by carrying out a linear fit to the data in this limit. The extracted weights were naturally normalized and the sum of weights for each mode was found to be within less than a 2% of the expected value (table 5.1).

The expected modes were determined by calculating the expected mode shift using equation 5.4 over the same range of δ_r as the experiment, and then extracting the slope from a linear fit. Both the experimental weights and the expected weights were plotted for the three different modes, illustrating the different distributions for the photons within the lattice in a 2D color plot (figure 5.12). Here the experimental weights are illustrated by larger circles, and the expected weights are illustrated by smaller circles embedded in the larger circles. Additionally a 3D plot of the mode weights was constructed to highlight the agreement between experiment and theory

(figure 5.13). The discrepancy between experiment and theory is believed to arise from systematic disorder in the lattice.

5.6 Summary

In this chapter the results from a perturbative scanning probe microscopy experiment on a 49-site Kagome lattice have been presented. By scanning a sapphire defect over the surface of each lattice site the distribution of three different photon modes was mapped throughout the lattice. In order to understand and quantify the experimental results a separate characterization experiment was conducted on a single coplanar wave-guide resonator. In this experiment, the scanning probe was scanned laterally and vertically over the surface of the resonator. By adjusting the position of the probe the resonator was shown to be tunable up to 680 MHz, often a desirable capability experimentally. The response of the resonator to the sapphire probe was analyzed, compared to a finite element simulation, and a best fit function was determined to convert the measured probe position into defect size.

Using the same finite element software the size of the perturbation caused by the probe was determined, and used to extract the weight of the photons as each site. In the limit when the size of the perturbation was small the shift in the lattice modes were observed to shift linearly with the perturbation, and the slope of the linear shift was equal to the mode weights. Experimental results were compared to theoretical calculations from a tight binding hamiltonian, and a calculated percent error was reported to be less than 5%. Additionally, a unique feature of the Kagome lattice is a dispersionless band that forms from due to the geometric frustration. Here evidence was presented that demonstrates the first frustrated flatband within a Kagome lattice. These results are represent a valuable experimental step towards the development of a cQED based quantum simulator.

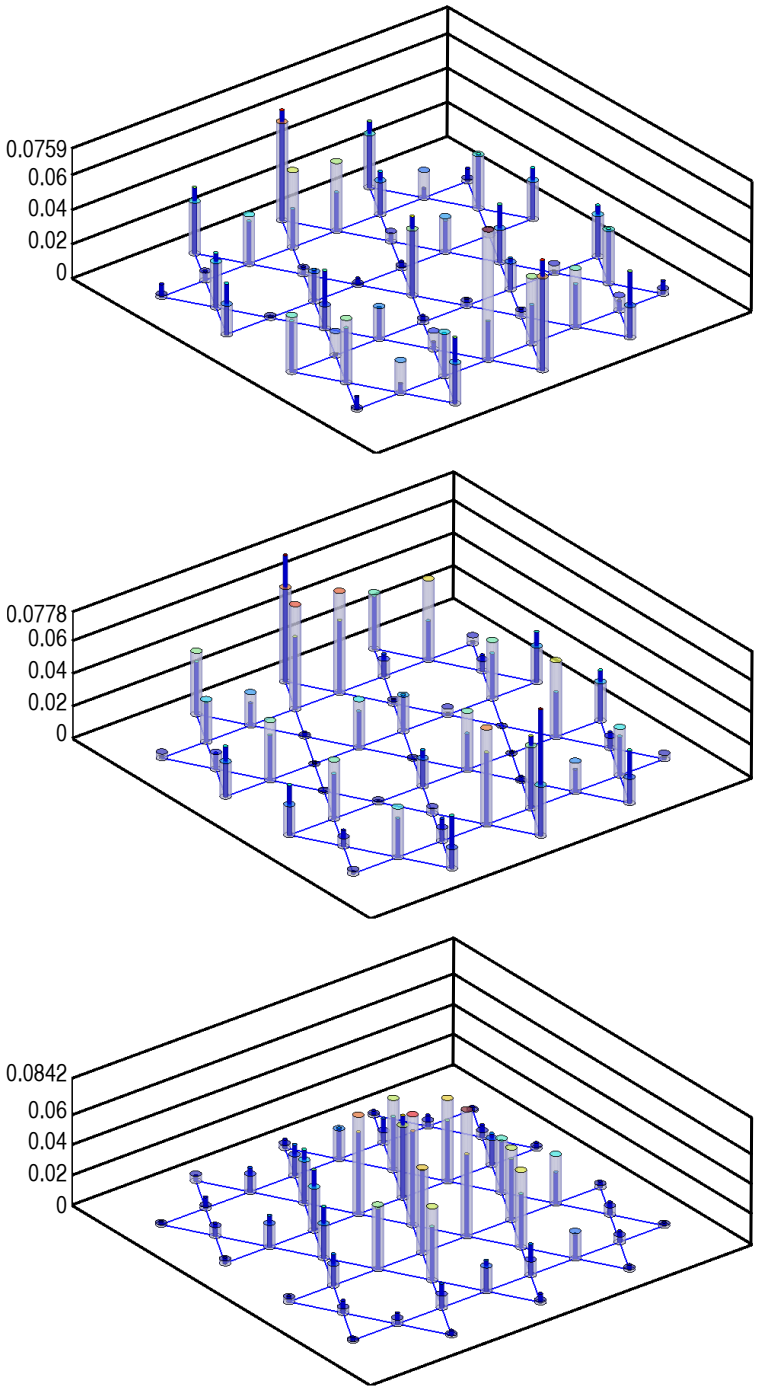

Figure 5.13: A 3D construction of the photon mode weights for the 35^{th}, 36^{th}, 49^{th} modes. Experimental results are represented by the larger semi-transparent cylinders, and theoretical results by the interior smaller dark blue cylinders. The height of each cylinder, and the color of the top of the cylinder shows the percentage of the photon at that site.

Chapter 6

Scanning circuit quantum electrodynamics

6.1 Introduction

This chapter details results for a scanning transmon qubit, strongly coupled to a transmission line resonator; this work was published in Nature Communications [94]. This qubit on a stick experiment was performed as a proof of concept, to demonstrate the potential of this tool for future applications as a local quantum probe on a lattice of transmission line resonators each coupled to a transmon qubit. Additionally such a tool would be a valuable resource for CQED characterization experiments. The chapter begins by discussing the experimental details of the scanning probe, such as the scanning stage that was constructed, the transmon qubit, and the coplanar waveguide resonator CPWR.

As a result of the uniqueness of these measurements, a detailed discussion of the measurement procedure will be provided, in addition to the analysis methods that were used. Subsequently the main result of strong coupling over a large scanning range will be presented and discussed. Additional discussions of experimental details

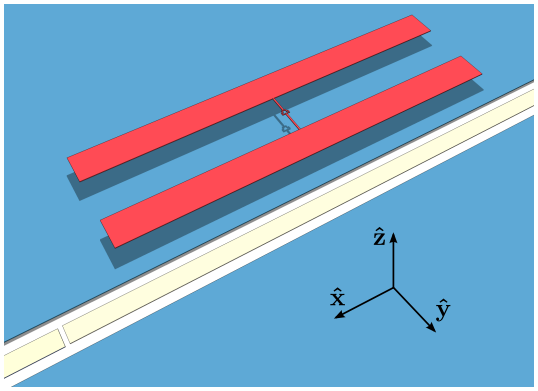

Figure 6.1: Illustration of the scanning transmon qubit.

will be presented following the main result. These details focus on parasitic modes that exist in the ground plane, and how the dependence of the resonator on the vertical position of the qubit.

6.2 Experimental setup

The qubit chip was mounted face down to a cryogenic three-axis positioning stage and positioned over a separate chip containing a $\lambda/2$ niobium CPWR (figure 6.2). In order to avoid direct contact between the resonator and the qubit, pads of photoresist 7µm thick were deposited on the corners of the qubit chip (figure 6.3). The positioners were mounted to a copper frame that was mounted to a dilution refrigerator which operated at temperatures 35mK.

6.2.1 Qubit on a stick

The scanning qubit described shown in figure 6.3 is a transmon design consisting of two aluminum islands connected by a thin aluminum wire interrupted by an aluminum oxide tunnel barrier, known as a Josephson junction [60]. The transmon design is well suited for scanning because it couples to CPWRs capacitively and requires no physical connections. The tunnel barrier provides a large nonlinear inductance which,

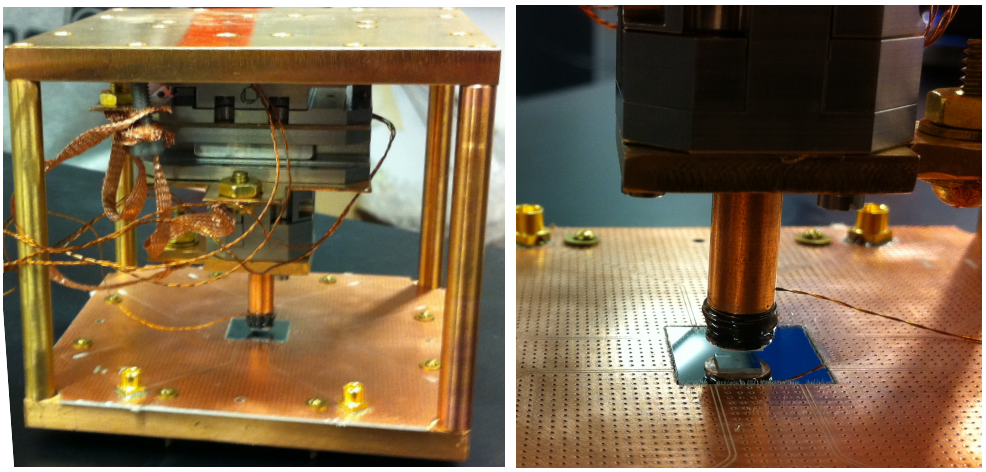

Figure 6.2: On the left a stack of three cryogenic linear nano-positioners mounted to a gold plated copper frame, that mounts to the bottom of a Bluefors dilution refrigerator. A smaller positioner (ANPz101/RES) sits at the bottom of the stack and provides Z movement with a working distance of 12 mm. Two linear positioners (Attocube ANPx340/RES) sit at the top of the stack, are mounted to the copper frame, and provide XY movement and have a working distance of 20 mm. In order to reduce the heating after movement, gold copper plates are mounted between each positioner, which is also mechanically clamped to copper braid that is then secured to the bottom of the dilution refrigerator. On the right a zoomed in picture of the qubit mounted to a copper rod positioned above the CPWR. A small solenoid is formed at the tip of the rod in order to flux tune the qubit. The magnet was coated in STYCAST 2850 FT to secure the wire.

together with the capacitance between the two islands, makes the transmon behave as a nonlinear LC oscillator whose lowest two energy states can be used as a qubit. A pair of tunnel barriers in parallel form a loop, as seen in figure 6.3, which allows for tuning the qubit energy with magnetic flux. By varying the flux through this loop with a magnet coil incorporated into the positioner, the qubit frequency ν_{q} could be varied from a maximum value of 12.1 GHz to close to zero [60]. Although here the flux loop's only purpose is to make the qubit energy tunable, such a loop can also be operated as a sensitive local magnetometer in a scanning SQUID microscope[48].

The qubit was fabricated using electron beam lithography and double-angle shadow evaporation with controlled oxidation of 30 and 100 nm layers of aluminum onto a 4×4 mm sapphire chip. The 0.5×1.0 mm crashpads on the corners of the

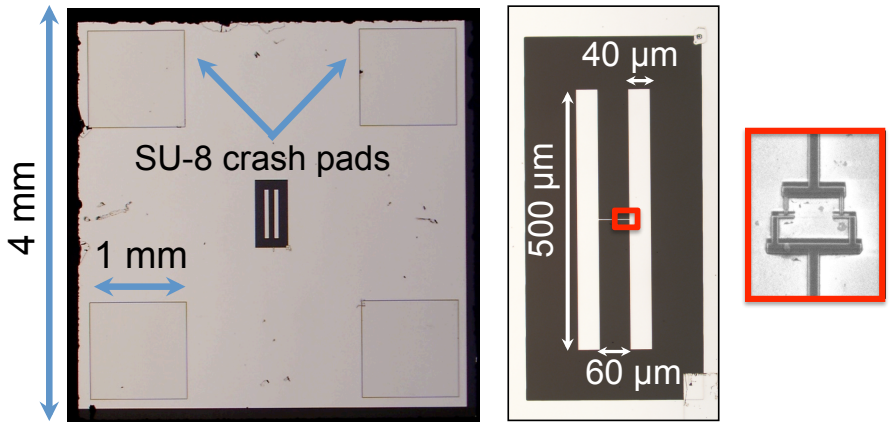

Figure 6.3: The transmon qubit chip used for scanning experiments. The qubit is surrounded by an aluminum ground plane, with SU8 crash pads on all four corners. On the far right, an SEM image shows the SQUID loop formed by the parallel junctions.

chip were made with photolithography of SU-8 2005 photoresist. The qubit chip was glued with methyl methacrylate to the tip of a highly conductive copper rod, with a magnetic tip, that is mounted to the cryogenic positioning stage. The wiring scheme of the coaxial lines was the same as that described in DiCarlo et al. [25].

6.2.2 Scanning resonator

The half-wave niobium resonator had a resonant frequency of 7.6 GHz without the presence of the qubit. The frequency ν_r of the resonator was found to increase when the qubit chip was brought into close proximity. The qubit was only scanned across the long straight section of the resonator, hence avoiding coupling the qubit to two sections of the resonator simultaneously. The resonator was defined by photolithography and acid etch (H_2O, HF, and HNO_3 in a 7.5:4:1 ratio) of a 200 nm film of niobium on a 14×14 mm sapphire chip. The resonator chip was mounted to a copper-patterned circuit board with silver paste and aluminium wire bonds, which connected the input and output transmission lines to coaxial lines. Wire bonds were only placed around the edge of the chip outside the footprint of the qubit chip.

Figure 6.4: CPWR used for strong coupling a scanning transmon qubit. Inset shows finger capacitors used to define the photon escape rate $\kappa = 10$ MHz. Subsequent qubit positions follow the x and y coordinate system shown here.

6.3 Qubit on a stick measurement procedure

Here the strength g of the coupling between the resonator and the qubit as a function of qubit position is studied. Following Koch et al. [60], the Hamiltonian $\hat{H}$ describing the coupled resonator-qubit system can be approximated by the Jaynes-Cummings Hamiltonian

$$\hat{H} = h\nu_{\mathrm{r}}\left(\hat{a}^{\dagger}\hat{a} + \frac{1}{2}\right) + \frac{h\nu_{\mathrm{q}}}{2}\hat{\sigma}_z + \frac{hg}{2}\left(\hat{a}\hat{\sigma}^{+} + \hat{a}^{\dagger}\hat{\sigma}^{-}\right) \tag{6.1}$$

with ν_{r} and ν_{q} the resonator and qubit frequencies respectively. In this expression, $\hat{a}, \hat{a}^{\dagger}$ are the creation and annihilation operators associated with photons in the resonator and $\hat{\sigma}^{+}$, $\hat{\sigma}^{-}$, and $\hat{\sigma}_z$ are the Pauli spin matrices associated with the qubit when treated as a two-level system. On resonance ($\nu_{\mathrm{q}} = \nu_{\mathrm{r}}$), the first two excited states of the system are $(|0\uparrow\rangle \pm |1\downarrow\rangle)/\sqrt{2}$ with corresponding energies $h\nu_{\mathrm{r}} \pm hg$ above that of the ground state $|0\downarrow\rangle$ where $|nq\rangle$ is the state with n photons in the resonator and the qubit in state q with $\downarrow$ ($\uparrow$) representing the qubit ground (excited) state. When driven with a microwave excitation, transitions to each of these excited states are allowed,

resulting in two peaks in the low power transmission spectrum. The coupling between the qubit and the resonator is determined by observing the frequency splitting $2g$ of these peaks, which is known as the vacuum Rabi splitting.

6.3.1 Finding resonance

The frequency ν_{r} of the resonator is dependent on the qubit's x and y positions. In order to ensure that resonance was possible at every qubit position, the qubit energy was tuned by varying the magnetic flux through the qubits' flux loop. In addition to the resonator's position dependence, changing the position of the qubit affected the threading of flux through the qubits SQUID loop. Once the SQUID loop was moved away from the gaps in the coplanar waveguide and positioned above the superconducting ground plane, the amount of flux produced by the magnet coil required to tune the qubit into resonance increased rapidly because the Meissner effect screened the magnetic field away from the superconducting ground plane.

In figure 6.5c, the coil magnetic flux that brought the qubit into resonance with the resonator is plotted for each position of figure 6.5a. The impact of the magnetic field screening could be greatly reduced by fabricating holes in the resonators ground plane. The strong dependence of the resonant magnetic flux on the qubit position as well as the steepness of the slope of qubit frequency versus magnetic flux (maximum qubit frequency $\nu_{q,max} \sim 12.1$ GHz) necessitated careful flux scanning at each qubit position in order to locate resonance. Searching for resonance by monitoring the transmission spectrum for an avoided crossing feature like the one shown in figure 6.9b would have required a long measurement time at each qubit position. Instead, only the low power transmission at the frequency ν_r of the high power transmission peak was monitored as the flux was swept. This results in a dip in transmission when the qubit is tuned into resonance (figure 6.6b).

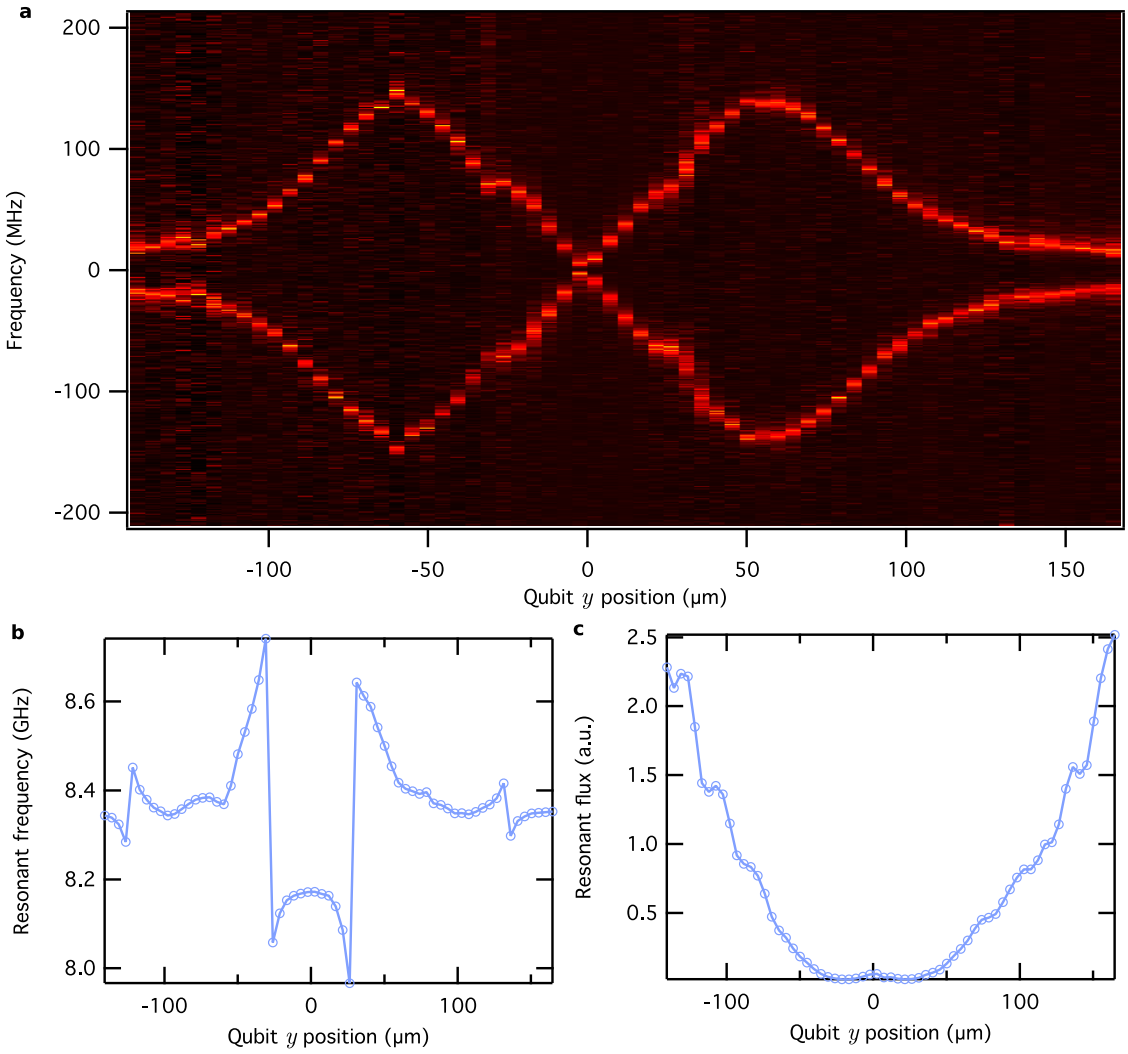

Figure 6.5: **a** The transmission spectra with the qubit tuned into resonance with the resonator is plotted for a series of qubit positions. At each position, the background is removed and the transmission is scaled so that the maximum transmission is unity. The frequency of each spectrum is offset so that the two peaks are centered around zero. The color map (in arbitrary units) is the same as that used in figure 6.8 **b**, The resonator frequency is plotted for each qubit position of figure 6.8. The frequency axis of each spectrum in figure 6.8 was offset by the frequency plotted here. **c**, The total flux (in arbitrary units) required to bring the qubit into resonance is plotted versus qubit position for the scan shown in figure 6.8.

When $|\nu_r - \nu_q| \gg g$, the coupled system is in the dispersive limit and one of the two mode frequencies $\nu_\pm$ given in Supplemental Equation (S1) differs from ν_r by $\sim g^2/(\nu_r - \nu_q)$ and is associated with a large peak in transmission. For most qubit frequencies the dispersive shift on the cavity is small compared to the resonator linewidth κ (typically 10MHz but as high as 35MHz at some qubit positions) and so transmission at ν_r is still high. However, when $\nu_q \sim \nu_r$, the mode frequencies are shifted from ν_r by $g > \kappa$ and transmission at ν_r is low. Figure 6.6a illustrates this behavior by showing transmission at ν_r versus flux and input power. Regular dips in transmission occur at low drive power where the qubit passes through resonance. Figure 6.6b plots just the low power transmission versus flux and shows that resonance can be easily identified by monitoring transmission at just one frequency value. In practice, a scan like that shown in figure 6.6b was taken at each position to identify the resonant flux range, and then a scan like that shown in figure 6.5 was taken over this flux range to obtain transmission spectra to fit for g.

Additional features are present in the crossover from the low power region to the high power region of the transmission. Figure 6.6c shows a finer scan of transmission versus power and flux at a qubit position close to that of the scan in figure 6.6a. These features are likely related to higher level qubit transitions coming into resonance with the resonator, though additional analysis is needed. While it is necessary to bring the resonator-qubit system into resonance in order to infer the coupling strength from the vacuum Rabi splitting, many CQED experiments, including the photon number measurement described in Johnson et al. [53], are performed with the qubit frequency detuned several hundred megahertz from the resonator. In this dispersive regime precise tuning of the qubit frequency is not required, and the qubit can be fabricated with a single tunnel barrier and measured without an external magnetic field.

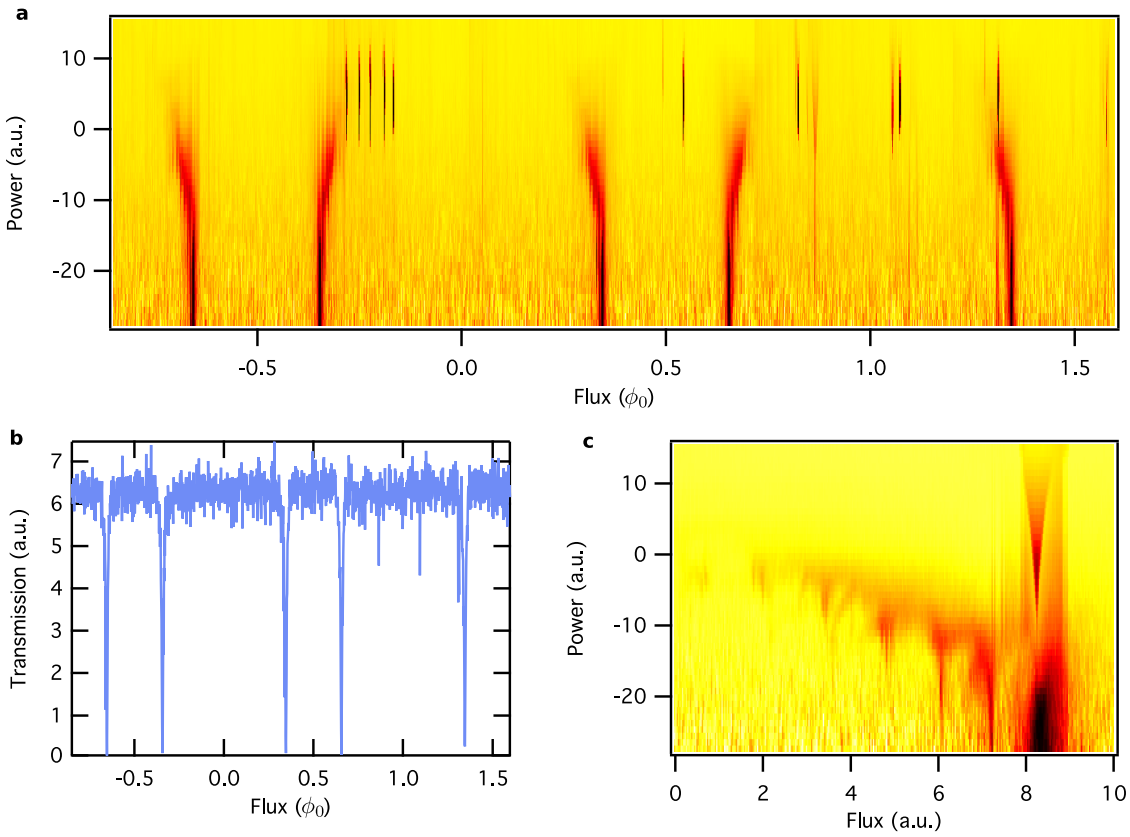

Figure 6.6: Transmission at the resonator frequency versus input power and magnetic flux. **a** The transmission at ν_r is plotted versus input microwave power on a log scale and magnetic flux threading the qubit loop. The flux axis has been scaled by the observed flux period ϕ_0. The power axis is uncalibrated, but the cross-over near -15 on resonance occurs as the photon occupation of the resonator increases from 0.1 to 10. The scan was taken at the same x position as figure 6.5 with the qubit close to the center pin and $g = 29$MHz. **b**, The average of the transmission for input powers less than -19 in panel **a** is plotted versus flux. **c**, Another scan of transmission versus power and flux like that in panel **a** is plotted for a flux region close to resonance. The flux axis is uncalibrated. The scan was taken at a position with $g = 21$ MHz, close to the position used for the scan shown in panel **a**. For panels **a** and **c**, the same color map (in arbitrary units) as that of figure 6.5 is used.

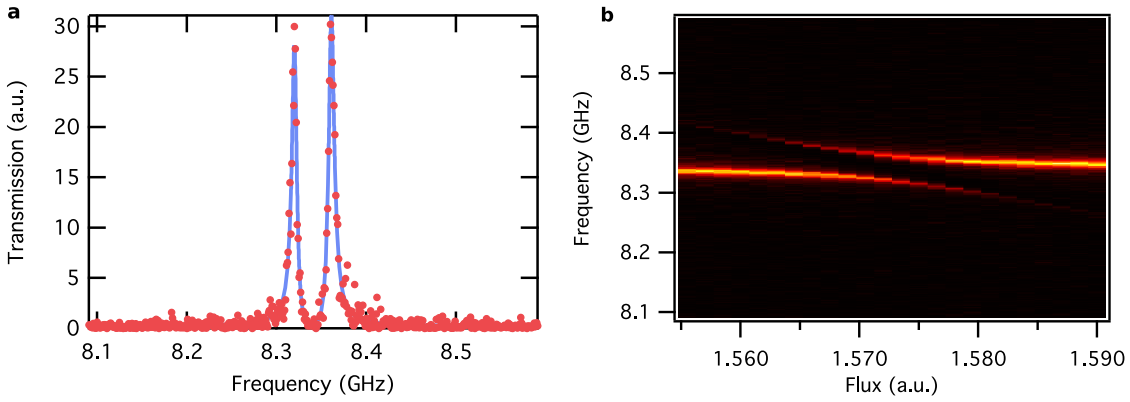

Figure 6.7: Fitting resonator transmission. **a**, The transmission at $y = 146\mu$m in figure 6.5 is plotted in arbitrary units along with a fit to equation 6.4. The fit coefficients are $A = 57$, $B = 0.2$, $g = 20$ MHz, $\kappa = 14$ MHz, $\nu_r = 8.342$ GHz, and $\nu_q = 8.339$ GHz. **b**, Transmission spectra recorded at the same position as panel **a** are plotted versus flux in arbitrary units as the qubit passes through resonance. The same color map (in arbitrary units) as that of figure 6.8 is used. Averaging the coefficients from fits to the transmission at each flux value gives $A = 59 \pm 3$, $B = 0.30 \pm 0.05$, $g = 20.4 \pm 0.3$ MHz, $\kappa = 12.8 \pm 0.8$ MHz, and $\nu_r = 8.342 \pm 0.001$ GHz where the errors represent the standard deviation of the coefficients.

6.3.2 Fitting resonance transmission

Transmission measurements were made in the low power limit for which the rate of photons entering the resonator was less than the escape rate, so that the resonator occupancy was less than one photon on average (figure 6.7). In this case, the transmission spectrum contains peaks at frequencies $\nu_\pm$ corresponding to transitions from the ground state $|0\ \downarrow\rangle$ to the states $|+\rangle$ and $|-\rangle$ which possess a $|1\ \downarrow\rangle$ component and are located at energies $h\nu_+$ and $h\nu_-$ above the ground state. The states and their frequencies are found by diagonalizing the Hamiltonian given in equation 6.1:

$$|\pm\rangle = \frac{\frac{\Delta}{2} \pm \sqrt{\left(\frac{\Delta}{2}\right)^2 + g^2}}{\sqrt{g^2 + \left(\frac{\Delta}{2} \pm \sqrt{\left(\frac{\Delta}{2}\right)^2 + g^2}\right)^2}} |0\uparrow\rangle + \frac{g}{\sqrt{g^2 + \left(\frac{\Delta}{2} \pm \sqrt{\left(\frac{\Delta}{2}\right)^2 + g^2}\right)^2}} |1\downarrow\rangle \quad (6.2)$$

and

$$\nu_{\pm} = \frac{\nu_r + \nu_q \pm \sqrt{4g^2 + \Delta^2}}{2} \tag{6.3}$$

with $\Delta = \nu_q - \nu_r$. The peak amplitudes are proportional to the probabilities $\omega_{\pm} = |\langle 1 \downarrow |\pm\rangle|^2$ of a photon being measured in the states $|\pm\rangle$. The peak line widths $\gamma_{\pm}$ are equal to the decay rates of the qubit (T_1^{-1}) and the photon (κ) weighted by the probability of measuring a qubit excitation and a photon respectively:$\gamma_{\pm} = \omega \pm \kappa + (1 - \omega_{\pm})T_1^{-1}$. The transmission peaks are taken to follow a lorentzian lineshape and the following function is used to fit the resonator transmission:

$$S_{21}(\nu) = B + A \left| \sum_{\pm} \omega_{\pm} l(\nu, \nu_{pm}, \gamma_{\pm}) \right|^2 \tag{6.4}$$

where A is the overall amplitude accounting for all attenuation and amplification in the measurement circuit, B is the background of the detector, and $l(\nu, \nu_0, \gamma)$ is the complex lorentzian centered at ν_0 with width γ:

$$l(\nu, \nu_0, \gamma) = \left(1 - i\frac{\nu - \nu_0}{\gamma/2}\right)^{-1} \tag{6.5}$$

When fitting for g, the parameters A, B, κ, ν_q, ν_r, and g were allowed to vary, while T_1 was was held fixed to the value obtained from coherence measurements. Figure 6.7 shows the result of fitting one of the transmission spectra from figure 6.8. Also shown is a plot of transmission versus flux as the qubit passes through resonance. For the coupling strength values shown in figure 6.9, similar flux scans were taken and the plotted values of coupling strength were obtained by averaging the coupling strength values obtained from fitting the transmission at each flux value.

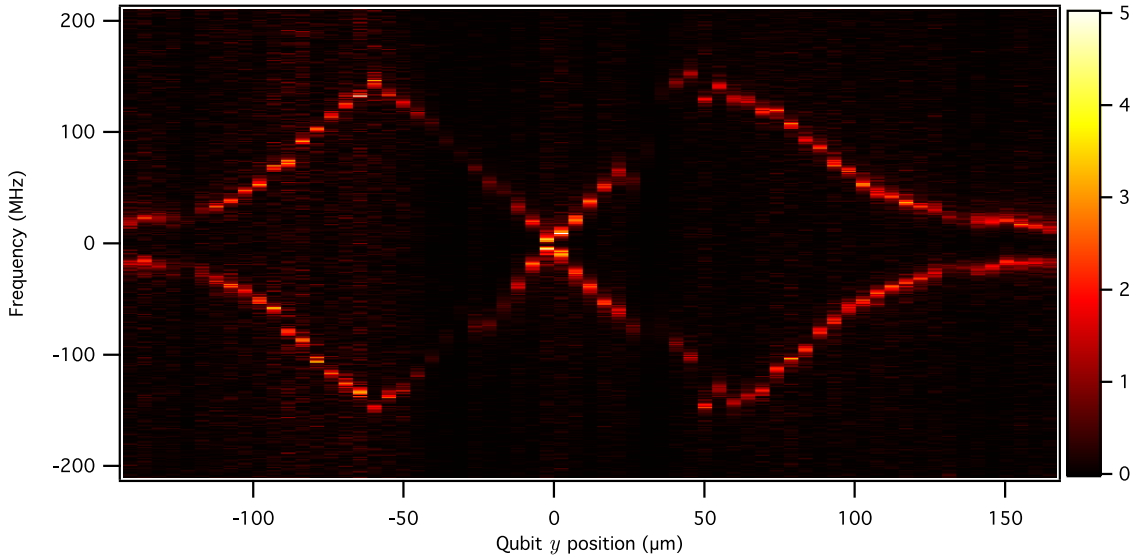

Figure 6.8: The transmission spectra with the qubit tuned into resonance with the resonator is plotted for a series of qubit positions. At each position, the background is removed and the transmission is scaled so that the maximum transmission is unity. The frequency of each spectrum is offset so that the two peaks are centered around zero. The vertical axis represents the difference between the frequency of the applied microwave drive and the resonator frequency. The shifted peak locations can also be interpreted as values of the coupling strength g, which is equal to half the peak separation. The y origin is taken to be the point of smallest peak separation, which can be interpret as the position where the qubit is centred over the resonator. The color represents the magnitude of microwave transmission and is plotted in arbitrary units, as the total gain and loss within the measurement chain has not been calibrated. The suppressed transmission at positions $y = \pm 30$ and 125μm is due to coupling between the resonator and a parasitic resonance in the metal frame of the qubit chip.

6.3.3 Resonance transmission spectra

Figure 6.8 shows the transmission spectra of the resonator for a sequence of regularly spaced qubit positions along the y axis perpendicular to the long dimension of the resonator. At each position, the current through the magnet coil was adjusted to bring the qubit into resonance (section 6.3.1), at which point the single transmission peak of the resonator was transformed into two peaks of equal height because of the vacuum Rabi splitting; clearly demonstrating strong coupling between the scanning qubit and the resonator. The position scan shows two regions of large peak separation symmetric about a position with nearly no peak separation, which was set as the origin. In

coupling to the resonator the transmon behaves as a dipole antenna. Because the two islands of the qubit are identical, by symmetry no coupling is expected when the qubit is centered above the resonator at $y = 0$. The points of maximum peak separation occur at $y \approx \pm 50\,\mu\text{m}$ where one of the two islands is centered over the resonator. At these points, the observed coupling strength $g \approx 140\,\text{MHz}$ was well into the strong coupling regime $g > \kappa, T_1^{-1}$ where the qubit relaxation time $T_1 = 3.2\,\mu\text{s}$ was determined by time-domain measurements (section 6.5) and the photon escape rate $\kappa = 10\,\text{MHz}$ was set by the resonator's output coupling capacitor which was chosen to be large in order to increase the rate of data acquisition. The photon escape rate κ, proportional to the linewidth of the transmission peak, was relatively constant as a function of position except for positions where a parasitic mode coupled to the resonator and broadened the linewidth to as much as 35 MHz (see Supplementary Note 2).

Scans of resonant transmission versus y position like figure 6.8 were repeated at five positions along the length of the resonator (the $\hat{\text{x}}$ direction) with a spacing of 600 μm. The coupling strengths g were extracted from fits to the transmission spectrum at each qubit position (section 6.3.2) are plotted in figure 6.9. The coupling strength increases as the qubit moves from the voltage node at the center of the resonator to the antinode at its end but exhibits the same shape for its y dependence at each x position. For technical reasons related to the operation of the positioning stage, measurements of the coupling strength at different z positions were not performed (section 6.4).

6.4 Position dependent coupling

The voltage profiles of the modes of a CPWR with open boundary conditions are sinusoidal along the length of the resonator with antinodes at its ends. The coupling

strength is proportional to the resonator voltage with one photon present and so should follow this sinusoid. The maximum coupling strength at each x position shown in figure 6.10a was fit to the sinusoidal form:

$$g\left(\Delta x\right) = g_{\max} \sin\left(\pi \frac{\Delta x + x_0}{l_{\mathrm{r}}}\right) \tag{6.6}$$

where $l_{\mathrm{r}} = 7,872\,\mu\mathrm{m}$ is the resonator length and $g_{\max}$ and x_0 were the fitting parameters. Here Δx is the set of displacements in x from the first x position (i.e. the values are $0\,\mu\mathrm{m}$; $600\,\mu\mathrm{m}$; $1,200\,\mu\mathrm{m}$; etc.). In figure 6.10a, the measured coupling strengths and the fit are plotted versus $x = \Delta x + x_0$.

The scan shown in figure 6.8 was taken on a separate cooldown from the scans shown in figure 6.9. The same resonator and qubit samples were used for both sets of measurements, but the sample stage was disassembled in between the cooldowns. During the cooldown in which data in figure 6.8 was taken, the qubit's x position was not varied, so the absolute x position of the data is not known. However, using the maximum value of g from figure 6.8 and the curve shown in figure 6.10a to calibrate the x position, one finds the data in figure 6.8 was taken at $x = 2,116\,\mu\mathrm{m}$.

The coupling strength as a function of the transverse position of the qubit follows an expression for the coupling strength given in Koch et al. [60]:

$$g\left(x,y,z\right) = 2\sqrt{\frac{2Z_{\mathrm{c}}}{h}} m\left(x\right) \nu_{\mathrm{r}} \beta\left(y,z\right) n_{01}\left(y,z,\nu_{\mathrm{r}}\right) \tag{6.7}$$

with the characteristic line impedance Z_{c} taken to be $50\,\Omega$ and $m(x)$ the sinusoidal mode shape factor given in equation (6.6). In order to describe the voltage division factor β and the transmon matrix element n_{01}, we first define C_{jk} to be the capacitance between components j and k and label the components of the system with a and b for the two islands of the transmon, p for the resonator center pin, and g for all other pieces of metal (the two ground planes and the metal frame on the qubit chip). The

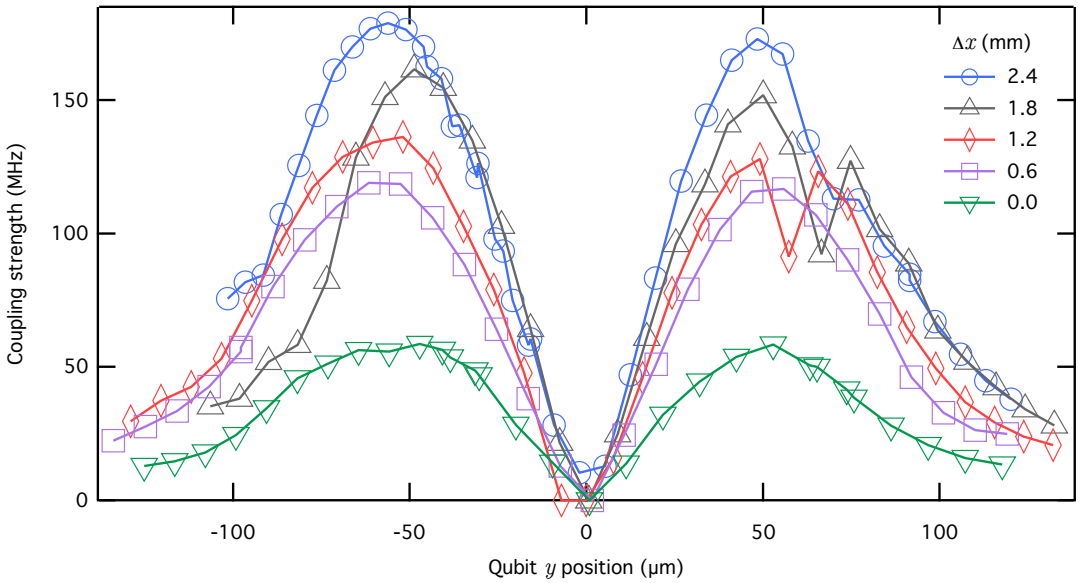

Figure 6.9: Traces of g versus qubit y position are shown for five qubit x positions spaced $\sim 600\mu$m apart from each other. The traces correspond to scans, such as the one shown in figure 6.8. Each value of g was determined by fitting several transmission spectra taken at values of magnetic flux for which the qubit frequency was close to that of the resonator. The sign of Δx is such that with increasing Δx the qubit moves from the electric field node at the center of the resonator towards the electric field antinode at its end. The individual coupling strength values between $y = 55$ and 80μm that deviate from the smooth trends of g versus y for $\Delta x \geq 1.2$ mm correspond to positions where the resonator coupled to a parasitic mode in the metal frame of the qubit chip (section 6.6).

voltage division factor β gives the fraction of the voltage drop from the resonator center pin to ground that falls across the two islands of the qubit. It can be written in terms of capacitance coefficients as

$$\beta = \frac{|C_{\mathrm{ap}}C_{\mathrm{bg}} - C_{\mathrm{bp}}C_{\mathrm{ag}}|}{C_{\mathrm{ab}}\left(C_{\Sigma,\mathrm{a}} + C_{\Sigma,\mathrm{b}}\right) + C_{\Sigma,\mathrm{a}}C_{\Sigma,\mathrm{b}}} \tag{6.8}$$

where $C_{\Sigma,x} = C_{x\mathrm{p}} + C_{x\mathrm{g}}$. The matrix element n_{01} was determined by numerically diagonalizing the transmon Hamiltonian given in Koch et al. [60]

$$\hat{H} = 4E_{\mathrm{C}}\hat{n}^2 - E_{\mathrm{J}}\cos\hat{\varphi} \tag{6.9}$$

to finds its eigenstates and eigenenergies and then evaluating $n_{01} = \langle 0|\hat{n}|1\rangle$, where $|0\rangle$ and $|1\rangle$ are the eigenstates with the two lowest energies, E_0 and E_1. The charging energy $E_\mathrm{C} = e^2/2C_\Sigma$ was calculated using the total capacitance given by

$$C_\Sigma = C_\mathrm{ab} + \left(\frac{1}{C_{\Sigma,\mathrm{a}}} + \frac{1}{C_{\Sigma,\mathrm{b}}}\right)^{-1}. \tag{6.10}$$

The qubit frequency ν_q is given by $(E_1 - E_0)/h$ and is thus a function of E_C and E_J. In calculating n_{01}, $\nu_\mathrm{q}(E_\mathrm{C}, E_\mathrm{J})$ was numerically inverted to solve for $E_\mathrm{J}(E_\mathrm{C}, \nu_\mathrm{q})$ with ν_q set equal to ν_r since measurements of the coupling strength were made with the qubit close to the resonator's frequency.

In order to produce the fit shown in figure 6.10b, the coupling strength $g(x, y, z)$ was calculated using the known values of Z_c and ν_r, the value of x obtained from the fit in figure 6.10a, and the values of the capacitances C_{jk} found by finite element analysis for a grid of y and z values with $1\,\mu\mathrm{m}$ spacing. The measured coupling strength versus y was fit to the $g(y, z)$ found by interpolating between the y and z grid points with z as the only free parameter. The finite element simulation was then repeated with the fitted value of z in order to produce the curve shown in figure 6.10b. We note that at the fitted value of $z = 11.0\,\mu m$ the charging energy $E_\mathrm{C} = 388\,\mathrm{MHz}$ is similar to values used in other CQED experiments and corresponds to a ratio of $E_\mathrm{J}/E_\mathrm{C} = 59$, within the transmon regime where the offset charge across the transmon islands (not included in the Hamiltonian given above) may be ignored. The finite element simulation included a layer of metal on the qubit chip that was not symmetric about the qubit and resulted in a asymmetry about $y = 0$ with the value of g at $-y$ being about 1% larger than the value at $+y$.

By the use of alignment marks on the resonator and qubit chips, it was possible to confirm that the misalignment between the two chips in the xy plane was $3^\circ \pm 1^\circ$. A misalignment of 3° was used in the finite element calculations for the capacitance

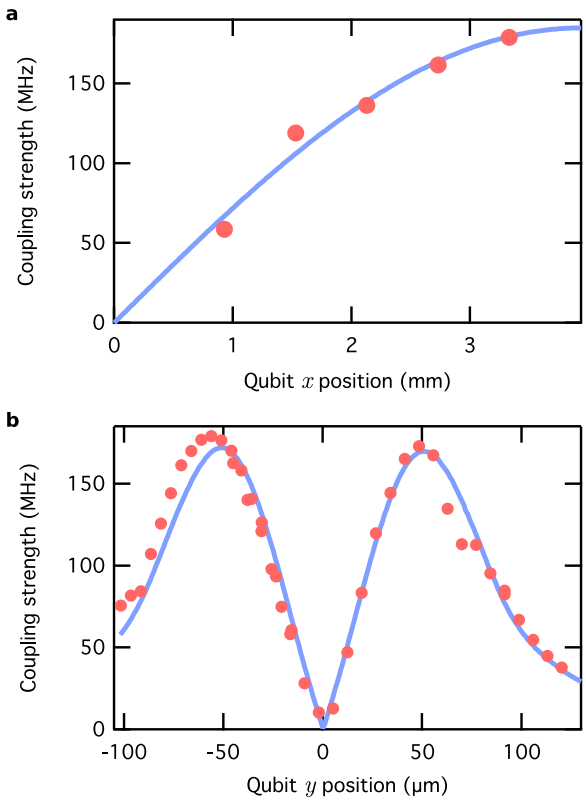

Figure 6.10: The maximum coupling strength g of each trace in figure 6.9 is plotted versus x position along with a fit to the expected sinusoidal dependence. The x origin represents the midpoint of the resonator. The offset of the data points from the resonator midpoint was determined by the fit (see Methods). The other fit parameter, the maximum coupling strength the end of the resonator, was found to be 185 MHz. (b) The largest trace of g versus y in figure 6.9 is replotted along with a fit to the form expected from finite element modeling of the qubit-resonator systems capacitance matrix (see Methods). The fitting function uses the resonator frequency ν_r, the system geometry, and the qubit x position determined in panel a as fixed inputs and treats the qubit height z, found to be 11 mm, as its only free parameter.

coefficients. Using a misalignment of 2° (4°) instead gave a the fitted height z of 11.1 μm (10.7 μm).

6.5 Coherence measurements

Qubit coherence times ($T_1 = 3.2 \pm 0.1\mu s$, $T_2^* = 0.66 \pm 0.05\mu s$, section 2.2.3) were obtained using the techniques described in Schreier et al. [90]. For T_1, the qubit was driven into the excited state by a pulse slightly detuned from the qubit frequency

with detuning $\Delta \sim 10$ MHz and then measured with a pulse at the cavity frequency at a delay time τ after the qubit pulse. The excited state probability obtained from many averages for a series of values of τ was fit to a decaying exponential with time constant T_1. For T_2^* , the qubit was excited by a pulse with half the height of the pulse that drove the qubit into the excited state and excited again with a second identical pulse after a delay time τ; commonly referred to as a Hahn Echo experiment [93]. Then the qubit state was measured. The value of T_2^* was obtained by fitting the qubit excited state probability to an exponentially decaying sinusoid with frequency Δ and decay constant T_2^*.

The measurements were made during the same cool down and at the same x position as the data shown in figure 6.8. In order to obtain consistent measurements, the measurements were made immediately after the refrigerator was warmed up to 20K and then cooled back down to its base temperature. The coherence measurements were performed at $y = -113\mu$m ($g = 31$ MHz) in figure 6.8 with the qubit frequency detuned 700 MHz below the resonator.

6.6 Parasitic modes

In figure 6.8, the transmission is suppressed near $y = \pm 30$ and $\pm 125\mu$m due to the resonators coupling to parasitic modes. Because the behavior of these modes is nearly symmetric in qubit position, we believe them to be caused by resonances between the resonator chip and a layer of metal on the qubit chip that was patterned nearly symmetrically. The extra metal on the qubit chip was deposited for technical reasons and is not needed for the functioning of the qubit. By redesigning the qubit chip or resonator chip, these modes could be eliminated.

In figure 6.5a, the data from 6.8 is replotted after removing the background and normalizing the transmission peaks to unity in order to make the peaks near $y = \pm 30$

and ±125μm more visible. In figure 6.8, the origin of the frequency axis was set to the location of the high power transmission peak and the qubit frequency was tuned to produce two peaks of equal height in transmission. For some positions near where the resonator coupled to the parasitic modes, these conditions produced two peaks not centered around zero. In 6.5a, the frequency axis at each position has been shifted to center the peaks around zero, so that the transmission peaks at neighboring positions can be more easily compared.

The parasitic modes appeared as lower and broader peaks in transmission at frequencies that varied with position and did not vary with magnetic flux. These modes were always present but only affected the measurement of the resonator-qubit system when their frequencies were close to the resonator frequency. When the frequency of one of these modes was close to the resonator frequency, the coupling between the parasitic mode and the resonator resulted in two modes with excitations partially of the resonator and partially of the parasitic mode. The narrower peak of the resulting two peaks in transmission was chosen to be the resonator peak for the purpose of coupling to the qubit. The width of this peak increased from $\kappa = 10$ MHz when the resonator was not coupled to a parasitic mode to a maximum value of 35MHz when it was most strongly coupled. Figure 6.5b shows the frequency of the chosen peak for each position in figure 6.8. Jumps in the resonator frequency due to avoided crossings with parasitic modes are visible at the y positions with low transmission in figure 6.8. Although the modes appear to affect the qubit symmetrically about $y = 0$ in figure 6.8, the modes y dependence varied with x position. In particular, for the data of figure 6.9, the resonant frequency versus qubit y position plots looked similar to that in 6.5b, but were shifted in y by 30 to 40μm.

6.7 Resonator dependence on qubit height

Results have been presented for the coupling of the qubit to the resonator as a function of lateral position (x and y). Measurements of the couplings dependence on the qubits vertical displacement z from the resonator were not possible due to misalignment between the resonator and qubit chips. Evidence of this misalignment is visible in figure 6.11a which plots the resonator frequency versus the positioners z reading denoted by z_p.

The origin of z_p was chosen to be the point at which the positioner could no longer advance due to contact with the resonator chip. Above $z_p = 40\mu m$, the resonator frequency is shifted to higher values as the qubit chip is brought closer as expected due to the modification of the resonators effective dielectric constant by the qubits presence. Below 40μm, the resonator frequencys dependence on zp weakens and disappears even as the positioner continues to move. We interpret this behavior as the qubit chip coming into first partial contact with the resonator and then nearly full contact as compliance in the sample holder allow the two chips to align. We attribute the relatively small magnitude of the discrepancy of the qubit height obtained by the fit shown in figure 6.10 from the height of the photoresist pads to this compliance in the sample holder.

The resonator frequencys dependence on the qubit chip height shown in figure 6.11a allowed the resonator to be used to measure the qubit height. Supplementary Figure S4b plots noise spectra of the transmitted phase at the resonator frequency when the qubit chip is at $z_p = 0$ and 43μm. We interpret the phase fluctuations present when the qubit chip is hovering above the resonator and not present when the qubit chip is in mechanical contact as being due to motion of the qubit chip relative to the resonator chip.

Using the resonators phase versus frequency curve to convert the phase noise into an effective resonator frequency noise and then the curve shown in figure 6.11a

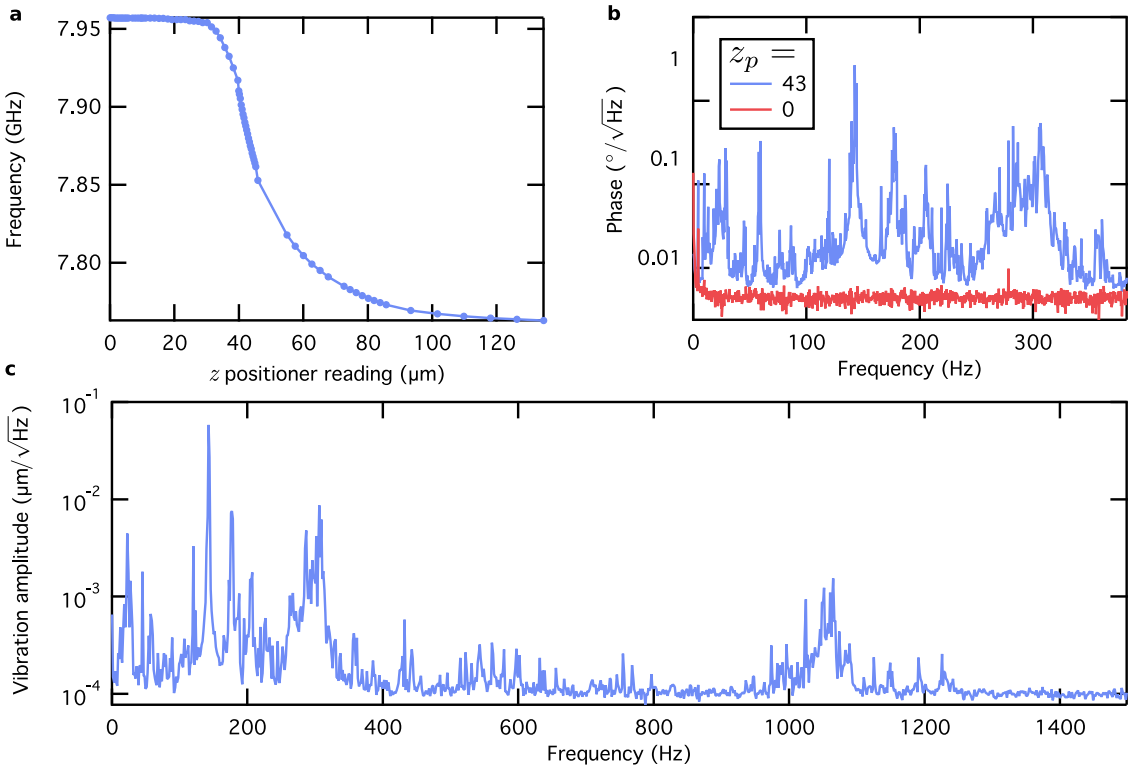

Figure 6.11: The effects of retracting the qubit from the resonator chip. **a**, The resonator frequency is plotted versus the reading z_p of the z positioner. At $z_p = 0$, the qubit chip is in hard contact with the resonator chip and can not be advanced further. **b**, The noise spectrum of the transmitted phase at the resonator frequency ν_r is plotted for the positions $z_p = 0$ and 43μm. **c**, The noise spectrum of the qubit-resonator displacement is plotted for $z_p = 43$μm using the data from panel **b**. The slope of the curve shown in panel **a** was used to convert the phase data into displacement.

to convert frequency into position, we obtain the position noise spectrum shown in figure 6.11c. Repeating this procedure at another z_p position and using the amplitude noise instead of the phase noise resulted in vibration spectra with similar features at similar magnitudes, confirming the interpretation of the features as being due to vibration of the qubit chip. The spectrum shown in figure 6.11c is typical for the mechanical response of cryogenic positioners such as those used in this experiment. The motion of the refrigerator base plate inferred from the spectrum shown in figure 6.11c agreed with measurements made with an accelerometer of another refrigerator that was the same model as that used for the measurements presented here. Because

all measurements of the qubit were made with the resonator and qubit chips in hard contact, no vibration isolation elements were included in the sample holder. In order to measure the dependence of the qubit-resonator coupling on height, such vibration isolation would need to be considered in addition to the alignment of the qubit and resonator chips.

Chapter 7

Conclusion

7.1 Future work

In this thesis I have presented the foundational experimental work for development of a photonic based quantum simulator. When reflecting on this work it is apparent that much of the research in the beginning was guided by experimental intuition, and also knowledge transferred from adjacent fields. Consequently many lessons were learned, and now hindsight can be used to improve upon future experiments. In this section I will conclude by highlighting some design suggestions for improving experiments, and then I will discuss some straightforward experiments with the scanning probe that could be used to impact not only lattice based experiments, but also the field of cQED.

7.1.1 Lattices and disorder

All lattices presented in this thesis formed a Kagome geometry. This lattice type naturally arises from symmetrically coupling three resonators together in a two dimensional geometry. One particular reason this lattice is of interest is because of the unique band structure that arises; for example the lowest energy flatband. Further-

more, for lattices with higher coordination number, it is believed that the measurements will more closely follow the theoretical mean field calculations; which are more accurate in higher dimensions. However, there are also many complications that arise in the two-dimensional architecture; most significantly the complications that arise from fabrication.

While much of the work in this thesis focused on reducing the effects of random disorder in the Kagome lattice, it is very likely that systematic disorder is still present in the larger lattices. Systematic disorder is believed to emerge because of the asymmetric resonator design necessary for the qubit fabrication process. Although a lot of effort went into engineering identical resonator, there is always room for improvement. One particular improvement could be made by designing identical resonators and fabricating the capacitive islands of the transmon in photolithography. Then during the ebeam lithography step, the josephson junctions could be fabricated such that they are either perpendicular or rotated 60^o from the islands. If the junction rotations are done properly, they will all be aligned and the double angle evaporation method could still be used for qubit fabrication.

One possible route to overcome fabrication difficulty of a two dimensional lattice would be to study one-dimensional lattices. Here each lattice site could be easily made identical; furthermore it has been shown that similar physics arises in a one-dimensional lattice [75]. Although the reduced dimensionality is further removed from mean field calculations, such experiments could provide valuable insight about the physics of open quantum systems. Such positive feedback would be invaluable for the more difficult experiments involving multi-dimensional lattices.

7.1.2 Qubit characterization experiment

The scanning probe experiments were motivated as a means to observe the internal lattice sites of a two-dimensional lattice. However, it has the potential to be a

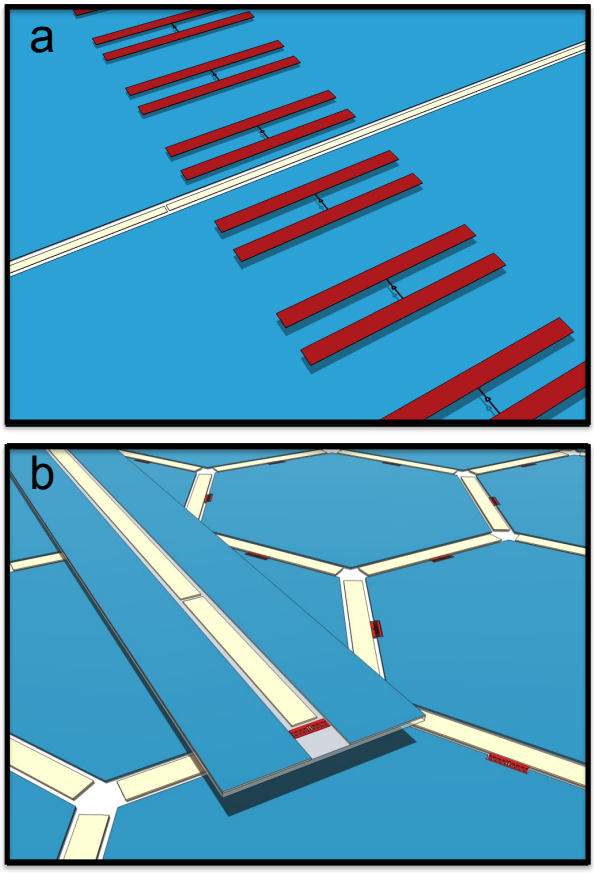

Figure 7.1: Applications of scanning CQED. **a**, In a single cool down it would be possible to measure many qubits and obtain valuable statistics on qubit properties. **b**, A scanning transmon capable of quantum measurements could be used for measurements of interior dynamics in the Jaynes Cummings lattice.

very useful tool for learning more about the qubit fabrication process. In this thesis resonator disorder has been investigated, but the effects of qubit disorder in a large lattice still remain an open question. A straight forward next experiment for the scanning probe would be to fabricate a large array of qubits on a single chip, and then scan them one by one across the resonator (figure 7.1a). This type of characterization experiment would provide useful statistics on important qubit properties such as qubit frequency disorder, and also qubit coherence times T_1 and T_2^*. Additionally, by fabricating many qubits with different geometries it would be possible to optimize the qubit fabrication process in a single cool down.

7.1.3 Probing quantum states

For experiments where the lattices have qubits, transmission measurements will be difficult to interpret the different quantum phases. For this reason a scannable qubit that is capable of doing quantum measurements of photon numbers at different lattice sites is highly desirable. This type of readout experiment has already been demonstrated to work on chip by Johnson et al. [53]; the difficulty now is getting it working on a movable probe. Once the technical details of this experiment have been ironed out, the question will be how to distinguish the proposed quantum states that exist within the lattice [61].

One possible method will be to take ensemble measurements of the photon number at different interior sites. By measuring the photon number many times, the state of the system could be inferred based on the fluctuations of the photon number. For example the polariton number is given as (keeping in mind polaritons are analogous to photons),

$$N_i = a_i^\dagger a_i + \sigma_i^+ \sigma_i^- \tag{7.1}$$

and then an ensemble measurement of this value would provide the variance of the polariton number

$$\Delta N = \langle N_i^2 \rangle - \langle N_i \rangle^2. \tag{7.2}$$

For the sought after Mott insulator state the variance is expected to be zero on a timescale $t < 1/\kappa, T_1, T_2^*$, and for a superfluid state the variance is expected to follow a Poisson distribution; the expected distribution for a coherent state. Such measurements would provide compelling evidence of the different phases.

7.2 Summary

The results in this thesis have laid the necessary experimental foundation for realizing a light based-quantum simulator. While no quantum phase transitions were actually observed, significant progress was made, and the problems that were solved were of fundamental importance for future experiments. As Isaac Newton once said, "If I have seen further, it is by standing on the shoulders of giants."

The first experiments in this thesis focused on developing a two dimensional lattice of capacitively coupled transmission line resonators without qubits. These resonators are the most basic building blocks in a circuit quantum electrodynamics architecture, and constructing a low disorder lattice of such resonators was an arduous task. Here a 12 resonator lattice that formed a Kagome star was studied, and it was discovered that small inconsistencies in the geometry of the resonator due to the fabrication process resulted in random shifts in different resonator frequencies [100]. These undesirable frequency shifts were suppressed by increasing the resonator feature sizes; no noticeable consequences from the change in geometry were observed. Furthermore calculations demonstrated that the undesirable shift was due to fluctuations in the Kinetic inductance of the superconductor.

There are still many open questions that remain about what is necessary for observing quantum phase transitions in cQED lattices, but one of the most significant questions relates to the finite size effects.The relevant theoretical proposals have all assumed the systems to be in the thermodynamic limit (infinite sized lattice) [38, 47, 61]; which raises the question how big must the lattice be in order to satisfy this assumption? While the answer to this question is still unknown, large lattices have been designed and studied. The largest lattice capable of incorporating transmon qubits contained 49 sites. It is believed that these are not large enough, but the size restriction was limited by technical constraints. Although, due to the ease of fabricating these lattices, larger sizes should be obtainable in future experiments.

One significant experimental challenge with the cQED architecture is related to the two dimensional orientation of the lattices. Consequently only exterior lattice sites are accessible by standard RF measurement techniques. In order to be able to observe the physics of interior lattice sites, a scanning probe microscopy tool was developed and two separate experiments were conducted in order to demonstrate the usefulness of such a scanning probe.

In one experiment, transmission measurements through a 49 site Kagome lattice without qubits were performed while perturbing each site with a sapphire defect. By perturbing each lattice site, it was possible to observe how photons flowed throughout the lattice, and create a map of the distribution of photons within the lattice. This experiment was primarily conducted as a "proof of concept" experiment, although such measurements could prove to be meaningful for probing exotic quantum states within a lattice with qubits. All the experimental measurements were compared to tight-binding calculations using experimental parameters, and shown to be in excellent agreement. Additionally evidence of a frustrated flatband was observed during the experiment. Such flatband modes are unique to the Kagome geometry, and are of greater interest for studying Ising model physics of interacting spins, and quantum magnetism. It is very likely that the result demonstrating the flatband will be of greater interest in future experiments.

The motivation of the scanning probe is its potential for a mobile quantum probe, capable of conducting quantum photon number detection. In the predicted quantum phases, the interesting Mott-insulator phase is defined by a fixed photon number at each site. By coupling a second superconducting qubit to an interior lattice site, it should be possible to extract the photon number from a single site, and measure the photon number variance; thereby determining the quantum state of the lattice. Here another "proof-of-concept" experiment was conducted in order to demonstrate the operation of a scannable qubit. In this experiment a separately fabricated, mobile

transmon qubit was coupled to a superconducting resonator. It was demonstrated that the superconducting qubit could obtain strong coupling to a transmission line resonator over a large scanning area [94].

The potential for superconducting circuits to be used to observe exotic states of light has motivated the work within this thesis; however, the true impact of these devices is still unknown. For example, most theoretical proposals have assumed a system well within equilibrium. This is not the case, because photonic systems area naturally dissipative, making them an ideal system to study non-equilibrium physics. Historically, systems far from equilibrium have been difficult to study, and theoretical models are generally computationally expensive. The use of cQED lattices to study non-equilibrium systems has already started to emerge, for example with a 2-site dimer, a non-equilibrium phase transition that is driven by dissipation has already been observed [84].

The true potential of cQED lattices will be subjects of future theses, but it is only by the hard work of the early pioneers that such results are possible. I am hopeful that interesting physics is on the horizon, and that future physicists are as inspired as I was.

Appendix A

Disorder Analysis

A.1 Disordered Peak Analysis

In a lattice of microwave cavities, disorder is an undesirable shift in the resonant frequency s.t. $\omega_i = \omega_r + \delta_i$ where δ_i is a random shift at site i. The total disorder in an array of resonators is the mean shift in resonant frequency $\sigma^2 = \langle 1/n \sum_i \delta_i^2 \rangle$. Here it is shown that the total disorder can be extracted from a measurement of the peak positions Ω_i^{dis}.

Some useful linear algebra relationships

$$\left\langle (x - \langle x \rangle)^2 \right\rangle = \langle x^2 \rangle - \langle x \rangle^2 \tag{A.1}$$

$$\mathrm{tr}(A) = \sum_i \lambda_i \tag{A.2}$$

$$\sum_i \sum_j A_{ij}^2 = \sum_i A_{ii}^2 + \sum_i \sum_{j \neq i} A_{ij}^2 \tag{A.3}$$

First show that the variance in disordered peak positions, from a disordered hamiltonian H is equal to the variance of of the matrix elements in that hamiltonian.

$$\begin{aligned}
\sum_i (\Omega_i^{dis} - \bar{\Omega}^{dis})^2 &= \sum_i (\Omega_i^{dis})^2 - \sum_i^n (\bar{\Omega}^{dis})^2 \\
&= \mathrm{tr}(H^2) - n(\frac{1}{n}\sum_i \Omega_i^{dis})(\frac{1}{n}\sum_i \Omega_i^{dis}) \\
&= \mathrm{tr}(H^2) - \frac{1}{n}\mathrm{Tr}(H)^2 \\
&= \sum_i \sum_j h_{ij}^2 - \frac{1}{n}\left(\sum_i h_{ij}\right)^2 \\
&= \sum_i \sum_j h_{ij}^2 - n\left(\frac{1}{n}\sum_i h_{ij}\right)^2 \\
&= \sum_i \sum_j h_{ij}^2 - n\bar{h}^2 \\
&= \sum_i \sum_j h_{ij}^2 - \sum_i \bar{h}^2
\end{aligned} \tag{A.4}$$

Now show that the variance in peak positions without disorder is related to the off diagonal matrix elements

$$\begin{aligned}
\sum_i (\Omega_i - \bar{\Omega})^2 &= \sum_i \Omega_i^2 - \sum_i^n \bar{\Omega}^2 \\
&= \sum_i \mathrm{Tr}\left([H - \mathrm{diag}(H)]^2\right) - \frac{1}{n}\mathrm{Tr}\left(H - \mathrm{diag}(H)\right)^2 \\
&= \sum_i \mathrm{Tr}\left([H - \mathrm{diag}(H)]^2\right) \\
&= \sum_i \sum_{j \neq i} h_{ij}^2
\end{aligned} \tag{A.5}$$

Combining the above results it is shown that the difference in variances is the equal to the sum of shifts in resonant frequency.

$$\begin{aligned}\sum_i (\Omega_i^{dis} - \bar{\Omega}^{dis})^2 - \sum_i (\Omega_i - \bar{\Omega})^2 &= \sum_i \sum_j h_{ij}^2 - \sum_i \bar{h}^2 - \sum_i \sum_{j \neq i} h_{ij}^2 \\ &= \sum_i h_{ii}^2 - \sum_i \bar{h}^2 \\ &= \sum_i (h_{ii} - \bar{h})^2 \\ &= \sum_i \delta_i^2 \end{aligned} \tag{A.6}$$

Appendix B

Fabrication recipes

B.1 BCB fabrication

Pre-treat substrate with O2 Plasma clean

15-20 etch with 300 Watt RF power, 180-190mT O2 chamber pressure

Spin coat BCB adhesion promoter

Spin at 3000 rpm; 20 sec.; 500 rpm/s

Bake for 30s at 100 C

Spin coat Cyclotene 4022-35

Slow ramp 500 rpm; 10 sec; 100 rpm/s

3500 rpm; 200 rpm/s; for 60s (film thickness $\sim$ 4.8 to 5um post development)

Bake for 90s at 90 C

Exposure MJB4 2.0 s

MJB4 2.0 s

Bake 5 min at 60 C; cover with glass

Develop in heated DS 3000 developer

Bring DS 3000 to 35 C on a hotplate. Use a thermometer make sure correct

temperature. (May take 20-30 min to warm developer)

Submerge into DS 300 for 10 min

Remove from heated DS 3000 and dip into room temperature bath of DS 3000 (This slows the development)

Rinse thoroughly in DI water, then N2 dry

Post exposure bake for 60s at 90 C

Cure in vacuum oven (a good cure is important for better performance!)

Pump out chamber then purge with nitrogen. Repeat many times to remove all oxygen from chamber. After finished pump out chamber and leave under vacuum.

Slowly ramp to 150 C (at least 60 min)

Hold oven temp at 150 C for 15 min

Ramp oven temp to 250 C, and hold for 2 hours

Cool to room temp

Descum to remove thin film of BCB from surface of substrate.

5 min etch with 80:20 mixture of O2:CF4 plasma.

Look at substrate under microscope to check for residue, or check film thickness with profolometer

If residue remains, repeat etch until all residue is removed.

B.2 Niobium plasma etch

A plasma etch recipe to etch 200nm of Nb in an inductively coupled plasma etcher. The etch consists of two steps, an O_2 plasma descum followed by an SF_6 plasma etch. Plasma etches are the most consistent method of etching metals, but there are often undesirable side effects on sidewalls that can be difficult to debug (figure 4.9).

O_2 plasma descum

50mTorr chamber pressure

100 Watt RF power

20 scam O_2 gas flow rate

10 sec. etch time

SF_6 plasma etch

2.0 mTorr chamber pressure

150 Watt RF power

5.0 sccm O_2 gas flow rate

50 sccm SF_6 gas flow rate

50 sec. etch time

B.3 Niobium wet etch

This wet etch recipe will etch 200 nm of Nb. Wet etches are not as isotropic as directional plasma etches, but when equipment breaks down it is a very convenient backup plan. This wet etch is a three-part acid etch of H_2O:HNO_3:HF in a ratio of 7.5 : 4 : 1. The specific recipe used is as follows:

Preparation step: pre pour all liquids into separate containers

20 ml of Hydrofluoric Acid

80 ml of Nitric Acid

150 ml of D.I. water

Etching procedure

Pour D.I. water into non-glass container

Pour Nitric Acid into D.I. water

Pour Hydrofluoric Acid into D.I.:Nitric mixture

Stir acid solution

Submerge Nb wafer into solution for 20 seconds

Immediately remove and rinse off in D.I. water

Note: for best results etch device immediately after mixing acid solution. The etch rate will change drastically if the solution is allowed to sit too long.

Appendix C

Publications

Publications that resulted from the work in this thesis.

- Underwood, D.L., Shanks, W.E., Koch, J., Houck, A.A. "Low Disorder Microwave Cavity Lattices for Quantum Simulation with Photons." Phys. Rev. A **86**, 023837 (2012)

- Shanks, W.E., Underwood, D.L., Houck, A.A. "A scanning transmon qubit for strong coupling circuit quantum electrodynamics." Nat. Comm. **4**, 1991 (2012)

Appendix D

Conference Presentations

- APS March Meeting, '*Imaging the Mode Structure of a Kagome Lattice of Superconducting Resonators with a Scanning Defect*', March 2014
- Les Houches School of Physics, '*Quantum Optics and Nano Photonics'*, August 2013
- APS March Meeting, '*Realizing a Lattice-Based Quantum Simulator Using Circuit Quantum Electrodynamics*', March 2013
- CLEO '*Low Disorder Microwave Cavity Lattices for Quantum Simulation With Photons*,' May 2012
- APS March Meeting, '*Disorder in a Kagome Lattice of Superconducting Coplanar Waveguide Resonators*', March 2012
- APS March Meeting, '*Microwave Cavity Lattices for Simulating Condensed Matter Physics*', March 2011

Bibliography

[1] M H Anderson, J R Ensher, M R Matthews, C E Wieman, and E a Cornell. Observation of bose-einstein condensation in a dilute atomic vapor. *Science*, 269(5221):198–201, July 1995.

[2] P W Anderson. Absence of Diffusion in Certain Random Lattices. *PRL*, 386(1949), 1956.

[3] D Angelakis, M Santos, and S Bose. Photon-blockade-Induced Mott Transitions and XY Spin Models in Coupled Cavity Arrays. *Physical Review A*, 76(3):3–6, September 2007.

[4] J R Anglin and W Ketterle. Bose-Einstein condensation of atomic gases. *Nature*, 416(March):211–218, 2002.

[5] A Aspuru-Guzik and P Walther. Photonic quantum simulators. *Nature Physics*, 8(4):285–291, April 2012.

[6] C M Bhat. Measurements of Higher Order Modes in 3rd Harmonic RF Cavity at Fermilab. *IEEE*, pages 787–789, 1993.

[7] L S Bishop. Circuit Quantum Electrodynamics. *PhD Thesis*, 2010.

[8] A Blais, R S Huang, A Wallraff, S M Girvin, and R J Schoelkopf. Cavity quantum electrodynamics for superconducting electrical circuits: An architecture for quantum computation. *Physical Review A*, 69(6):1–14, June 2004.

[9] R Blatt and C F Roos. Quantum simulations with trapped ions. *Nature Physics*, 8(4):277–284, April 2012.

[10] I Bloch. Ultracold quantum gases in optical lattices. *Nature Physics*, 1(October), 2005.

[11] I Bloch, J Dalibard, and S Nascimbène. Quantum simulations with ultracold quantum gases. *Nature Physics*, 8(4):267–276, April 2012.

[12] M Boissonneault, J Gambetta, and A Blais. Dispersive regime of circuit QED: Photon-dependent qubit dephasing and relaxation rates. *Physical Review A*, 79(1):013819, January 2009.

[13] D. Braak. Integrability of the Rabi Model. *Physical Review Letters*, 107(10):100401, August 2011.

[14] I Buluta and F Nori. Quantum simulators. *Science (New York, N.Y.)*, 326(5949):108–11, October 2009.

[15] E Carlsson and S Gevorgian. Conformal Mapping of the Field and Charge Distributions in Multilayered Substrate CPW s. *IEEE Trans. Microwave Theory Tech.*, 47(8):1544–1552, 1999.

[16] Z Chen, A Megrant, J Kelly, R Barends, J Bochmann, Y Chen, B Chiaro, A Dunsworth, J Y Mutus, P Malley, C Neill, P Roushan, D Sank, A Vainsencher, J Wenner, A N Cleland, and J M Martinis. Fabrication and Characterization of Aluminum Airbridges for Superconducting Microwave Circuits. *arXiv:1310.2325v1*, 2013.

[17] I J Cirac and P Zoller. Goals and opportunities in quantum simulation. *Nature Physics*, 8(4):264–266, April 2012.

[18] J Clarke and F K Wilhelm. Superconducting quantum bits. *Nature*, 453(7198):1031–42, June 2008.

[19] ATLAS Collaboration. Observation of a new particle in the search for the Standard Model Higgs boson with the ATLAS detector at the LHC. *Physics Letters B*, 716(1):1–29, September 2012.

[20] CMS Collaboration. Observation of a new boson at a mass of 125 GeV with the CMS experiment at the LHC. *Physics Letters B*, 716(1):30–61, September 2012.

[21] F Dalfovo, S Giorgini, I Povo, Lev P Pitaevskii, and S Stringari. Theory of Bose-Einstein condensation in trapped gases. *Reviews of Modern Physics*, 71(3):463–512, 1999.

[22] H Deng, H Haug, and Y Yamamoto. Exciton-polariton Bose-Einstein condensation. *Reviews of Modern Physics*, 82(2):1489–1537, May 2010.

[23] M H Devoret, S Girvin, and R Schoelkopf. Circuit-QED: How strong can the coupling between a Josephson junction atom and a transmission line resonator be? *Annalen der Physik*, 16(10-11):767–779, October 2007.

[24] M H Devoret and R J Schoelkopf. Superconducting circuits for quantum information: an outlook. *Science (New York, N.Y.)*, 339(6124):1169–74, March 2013.

[25] L Dicarlo, J M Chow, J M Gambetta, Lev S Bishop, B R Johnson, D I Schuster, J Majer, A Blais, L Frunzio, S M Girvin, and R J Schoelkopf. Demonstration of two-qubit algorithms with a superconducting quantum processor. *Nature*, 460(7252):240–244, 2009.

[26] David P. DiVincenzo. The Physical Implementation of Quantum Computation. *Fortschritte der Physik*, 48(9-11):771–783, September 2000.

[27] G J Dolan. Offset masks for lift-off photoprocessing. *Applied Physics Letters*, 31(5):337, 1977.

[28] M. a. Eriksson, R. G. Beck, M. Topinka, J. a. Katine, R. M. Westervelt, K. L. Campman, and a. C. Gossard. Cryogenic scanning probe characterization of semiconductor nanostructures. *Applied Physics Letters*, 69(5):671, 1996.

[29] G Evenbly and G Vidal. Frustrated Antiferromagnets with Entanglement Renormalization: Ground State of the Spin-1/2 Heisenberg Model on a Kagome Lattice. *Physical Review Letters*, 104(18):187203, May 2010.

[30] R P Feynman. Simulating physics with computers. *International Journal of Theoretical Physics*, 21(6-7):467–488, June 1982.

[31] M P A Fisher, P B Weichman, J Watson, and D S Fisher. Boson localization. *Physical Review B*, 40(1), 1989.

[32] A Fragner, M Baur, R Bianchetti, S Filipp, J M Fink, P J Leek, G Puebla, L Steffen, and A Wallraff. Coplanar Waveguide Resonators for Circuit Quantum Electrodynamics. *Measurement*, pages 1–8, 2008.

[33] L Frunzio, A Wallraff, D Schuster, J Majer, and R J Schoelkopf. Fabrication and Characterization of Superconducting Circuit QED Devices for Quantum Computation. *EEE Trans. Appl. Supercond.*, 15(2):860–863, 2005.

[34] J Gao, M Daal, A Vayonakis, S Kumar, J Zmuidzinas, B Sadoulet, B A Mazin, P K Day, and H G Leduc. Experimental evidence for a surface distribution of two-level systems in superconducting lithographed microwave resonators. *Applied Physics Letters*, 92(15):152505, 2008.

[35] a K Geim and K S Novoselov. The rise of graphene. *Nature materials*, 6(3):183–91, March 2007.

[36] S Giorgini and S Stringari. Theory of ultracold atomic Fermi gases. *Reviews of Modern Physics*, 80(4):1215–1274, October 2008.

[37] D A Goldberg and R A Rimmer. Measurement and Identificaiton of HOM's in RF Cavities. *IEEE*, pages 3001–3003, 1998.

[38] A D Greentree, C Tahan, J H Cole, and L C L Hollenberg. Quantum Phase Transitions of Light. *Nature Physics*, 2(12):856–861, November 2006.

[39] M Greiner, O Mandel, T Esslinger, T W Hansch, and I Bloch. Quantum phase transition from a superfluid to a Mott insulator in a gas of ultracold atoms. *Nature*, 415:39–44, 2002.

[40] Lov K Grover. Quantum Mechanics Helps in Searching for a Needle in a Haystack. *Physical Review Letters*, 79(2):325–328, 1997.

[41] M Hafezi, P Adhikari, and J M Taylor. A chemical potential for light. *arXiv:1405.5821v2*, page 7, May 2014.

[42] M J Hartmann, F G S L Brandão, and M B Plenio. Strongly interacting polaritons in coupled arrays of cavities. *Nature Physics*, 2(12):849–855, November 2006.

[43] A L C Hayward, A M Martin, and A D Greentree. Fractional Quantum Hall Physics in Jaynes-Cummings-Hubbard Lattices. *Physical Review Letters*, 108(223602):1–5, 2012.

[44] Peter W Higgs. Broken symmetries and the masses gauge bosons. *Physical Review Letters*, 13(16):508–509, 1964.

[45] A J Hoffman, S Srinivasan, S Schmidt, L Spietz, J Aumentado, H Türeci, and A A Houck. Dispersive Photon Blockade in a Superconducting Circuit. *Physical Review Letters*, 107(5):1–4, July 2011.

[46] J M Hornibrook, E E Mitchell, and D J Reilly. Superconducting Resonators with Parasitic Electromagnetic Environments. *arXiv:1203.4442v1*, 2012.

[47] A A Houck, J Koch, and H E Türeci. On-chip quantum simulation with superconducting circuits. *Nature Physics*, 8(4):292–299, April 2012.

[48] M E Huber, N C Koshnick, H Bluhm, L J Archuleta, T Azua, P G Björnsson, B W Gardner, S T Halloran, E A Lucero, and K A Moler. Gradiometric micro-SQUID susceptometer for scanning measurements of mesoscopic samples. *The Review of scientific instruments*, 79(5):053704, May 2008.

[49] S D Huber and E Altman. Bose condensation in flat bands. *Physical Review B*, 82(18):184502, November 2010.

[50] W M Itano, J C Bergquist, J J Bollinger, and D J Wineland. Cooling methods in ion traps. *Physica Scripta*, T59:106–120, January 1995.

[51] E Jaynes and F Cummings. Comparison of Quantum and Semiclassical Radiation Theories with Application to the Beam Maser*. *Proceedings of the IEEE*, 1963.

[52] Michael Johanning, Andrés F Varón, and Christof Wunderlich. Quantum simulations with cold trapped ions. *Journal of Physics B: Atomic, Molecular and Optical Physics*, 42(15):154009, August 2009.

[53] B R Johnson, M D Reed, A A Houck, D I Schuster, Lev S Bishop, E Ginossar, J M Gambetta, L DiCarlo, L Frunzio, S M Girvin, and R J Schoelkopf. Quantum non-demolition detection of single microwave photons in a circuit. *Nature Physics*, 6(9):663–667, June 2010.

[54] P Jurcevic, B P Lanyon, P Hauke, C Hempel, P Zoller, R Blatt, and C F Roos. Quasiparticle engineering and entanglement propagation in a quantum many-body system. *Nature*, 511(7508):202–205, July 2014.

[55] J Kasprzak, M Richard, S Kundermann, A Baas, P Jeambrun, J M J Keeling, F M Marchetti, M H Szymaska, R André, J L Staehli, V Savona, P B Littlewood, B Deveaud, and L S Dang. Bose-Einstein condensation of exciton polaritons. *Nature*, 443(7110):409–14, September 2006.

[56] K Kim, S Korenblit, R Islam, E E Edwards, M S Chang, C Noh, H Carmichael, G D Lin, L M Duan, C C Joseph Wang, J K Freericks, and C Monroe. Quantum simulation of the transverse Ising model with trapped ions. *New Journal of Physics*, 13(10):105003, October 2011.

[57] T Kitagawa, M A Broome, A Fedrizzi, M S Rudner, E Berg, I Kassal, A Aspuru-Guzik, E Demler, and A G White. Observation of topologically protected bound states in photonic quantum walks. *Nature communications*, 3:882, January 2012.

[58] E Knill, R Laflamme, and G J Milburn. A scheme for efficient quantum computation with linear optics. *Nature*, 409(6816):46–52, January 2001.

[59] J Koch, A A Houck, K L Hur, and S M Girvin. Time-reversal-symmetry breaking in circuit-QED-based photon lattices. *Physical Review A*, 82(4):043811, October 2010.

[60] J Koch, T M Yu, J Gambetta, A A Houck, D I Schuster, A Blais, M H Devoret, S M Girvin, and R J Schoelkopf. Charge insensitive qubit design derived from the Cooper pair box. *Physical Review A*, 76(042319):1–21, 2007.

[61] Jens Koch and K Le Hur. SuperfluidMott-Insulator Transition of Light in the Jaynes-Cummings Lattice. *Physical Review A*, 80(2):1–13, August 2009.

[62] E Kogan. Why Dirac points in graphene are where they are? *arXiv:1112.3826v7*, 2012.

[63] B P Lanyon, J D Whitfield, G G Gillett, M E Goggin, M P Almeida, I Kassal, J D Biamonte, M Mohseni, B J Powell, M Barbieri, A Aspuru-Guzik, and a G White. Towards quantum chemistry on a quantum computer. *Nature chemistry*, 2(2):106–11, March 2010.

[64] S Lloyd. Universal Quantum Simulators. *Science*, 273(5278), 1996.

[65] X S Ma, T Herbst, T Scheidl, D Wang, S Kropatschek, W Naylor, B Wittmann, A Mech, J Kofler, E Anisimova, V Makarov, T Jennewein, R Ursin, and A Zeilinger. Quantum teleportation over 143 kilometres using active feed-forward. *Nature*, 489(7415):269–73, September 2012.

[66] Xiao-song Ma, Borivoje Dakic, William Naylor, Anton Zeilinger, and Philip Walther. Quantum simulation of the wavefunction to probe frustrated Heisenberg spin systems. *Nature Physics*, 7(5):399–405, February 2011.

[67] L C Maier and J C Slater. Field Strength Measurements in Resonant Cavities. *Journal of Applied Physics*, 23(1):68, 1952.

[68] G D Massa, S Costanzo, A Borgia, F Venneri, and I Venneri. Innovative dielectric materials at millimeter-frequencies. *ICECom Conference Proceedings*, pages 1–4, 2010.

[69] Mielke. Exact ground states for the hubbard model on the Kagome lattice. *J. Phys. A.*, 25:4335–4345, 1992.

[70] A Mielke. Ferromagnetic ground states for the Hubbard model on line graphs. *J. Phys. A.*, 24:73, 1991.

[71] A Mielke and H Tasaki. Ferromagnetism in the Hubbard model. Examples from models with degenerate single-electron ground states. *Commun. Math. Phys.*, 158:341, 1993.

[72] K. W. Murch, U. Vool, D. Zhou, S. J. Weber, S. M. Girvin, and I. Siddiqi. Cavity-Assisted Quantum Bath Engineering. *Physical Review Letters*, 109(18):183602, October 2012.

[73] T Niemczyk, F Deppe, H Huebl, E P Menzel, F Hocke, M J Schwarz, J J Garcia-Ripoll, D Zueco, T Hümmer, E Solano, A Marx, and R Gross. Circuit quantum electrodynamics in the ultrastrong-coupling regime. *Nature Physics*, 6(10):772–776, July 2010.

[74] C Nietner. Quantum Phase Transition of Light in the Jaynes-Cummings Lattice. *Thesis*, 2010.

[75] F Nissen, S Schmidt, M Biondi, G Blatter, H Tureci, and J Keeling. Nonequilibrium Dynamics of Coupled Qubit-Cavity Arrays, 2012.

[76] K S Novoselov, A K Geim, S V Morozov, D Jiang, Y Zhang, S V Dubonos, I V Grigorieva, and A A Firsov. Electric field effect in atomically thin carbon films. *Science (New York, N.Y.)*, 306(5696):666–9, October 2004.

[77] A Nunnenkamp, Jens Koch, and S M Girvin. Synthetic gauge fields and homodyne transmission in Jaynes-Cummings lattices. *New Journal of Physics*, 13, 2011.

[78] H Paik, D I Schuster, Lev S Bishop, G Kirchmair, G Catelani, A P Sears, B R Johnson, M J Reagor, L Frunzio, L I Glazman, S M Girvin, M H Devoret, and R J Schoelkopf. Observation of High Coherence in Josephson Junction Qubits Measured in a Three-Dimensional Circuit QED Architecture. *Physical Review Letters*, 107(24):240501, December 2011.

[79] A Peruzzo, M Lobino, J C F Matthews, N Matsuda, A Politi, K Poulios, X Q Zhou, Y Lahini, N Ismail, K Wörhoff, Y Bromberg, Y Silberberg, M G Thompson, and J L OBrien. Quantum walks of correlated photons. *Science (New York, N.Y.)*, 329(5998):1500–3, September 2010.

[80] A Petrescu, A A Houck, and K Le Hur. Anomalous Hall effects of light and chiral edge modes on the Kagomé lattice. *Physical Review A*, 86(5):053804, November 2012.

[81] J M Pitarke, V M Silkin, E V Chulkov, and P M Echenique. Theory of surface plasmons and surface-plasmon polaritons. *Reports on Progress in Physics*, 70(1):1–87, January 2007.

[82] D Porras and J I Cirac. Effective Quantum Spin Systems with Trapped Ions. *Physical Review Letters*, 92(20):207901, May 2004.

[83] Lewis Pyenson. *Quantum Generations: A History of Physics in the Twentieth Century*, volume 42. Princeton University Press, 2001.

[84] J Raftery, D Sadri, S Schmidt, H E Türeci, and A A Houck. Observation of a Dissipation-Induced Classical to Quantum Transition. *Physical Review X*, 4(3):031043, September 2014.

[85] M D Reed, B R Johnson, A A Houck, L DiCarlo, J M Chow, D I Schuster, L Frunzio, and R J Schoelkopf. Fast reset and suppressing spontaneous emission of a superconducting qubit. *Applied Physics Letters*, 96(20):203110, 2010.

[86] R L Rivest, A Shamir, and L Adleman. A Method for Obtaining Digital Signatures and Public- Key Cryptosystems. *Communications of the ACM*, 21(2):120–126, February 1978.

[87] S. Schmidt, D. Gerace, A A Houck, G. Blatter, and H Türeci. Nonequilibrium delocalization-localization transition of photons in circuit quantum electrodynamics. *Physical Review B*, 82(10):2–5, September 2010.

[88] S Schmidt and Jens Koch. Circuit QED lattices: Towards quantum simulation with superconducting circuits. *Annalen der Physik*, 525(6):395–412, June 2013.

[89] R J Schoelkopf and S M Girvin. Wiring up quantum systems. *Nature*, 451(7179):664–9, February 2008.

[90] J Schreier, A A Houck, Jens Koch, D I Schuster, B R Johnson, J Chow, J Gambetta, J Majer, L Frunzio, M Devoret, S M Girvin, and R J Schoelkopf. Suppressing charge noise decoherence in superconducting charge qubits. *Physical Review B*, 77(18):180502, May 2008.

[91] D I Schuster. Circuit Quantum Electrodynamics. *PhD Thesis*, 2007.

[92] T Schwartz, G Bartal, S Fishman, and M Segev. Transport and Anderson localization in disordered two-dimensional photonic lattices. *Nature*, 446(7131):52–5, March 2007.

[93] A P Sears, A Petrenko, G Catelani, L Sun, Hanhee Paik, G Kirchmair, L Frunzio, L I Glazman, S M Girvin, and R J Schoelkopf. Photon shot noise dephasing in the strong-dispersive limit of circuit QED. *Physical Review B*, 86(18):180504, November 2012.

[94] W E Shanks, D L Underwood, and A A Houck. A scanning transmon qubit for strong coupling circuit quantum electrodynamics. *Nature communications*, 4(May):1991, January 2013.

[95] K Sheshadri, H R Krishnamurthy, R Pandit, and T V Ramakrishnan. Superfluid and insulating phases in an interacting-boson model : mean-field theory and the RPA. *Europhys. Lett.*, 22(4), 1993.

[96] P W Shor. Algorithms for Quantum Computation : Discrete Logarithms and Factoring. *Proceedings of the 35th Annual Symposium on Foundations of Computer Science*, pages 124–134, 1994.

[97] R N Simons. *Coplanar Waveguide Circuits, Components, and Systems*. John Wiley & Sons, 2001.

[98] D T Smithey, M Beck, J Cooper, and M G Raymer. Measurement of number-phase uncertainty relations of optical fields. *Physical Review A*, 48(4), 1993.

[99] M. a. Topinka. Imaging Coherent Electron Flow from a Quantum Point Contact. *Science*, 289(5488):2323–2326, September 2000.

[100] D L Underwood, W E Shanks, Jens Koch, and A A Houck. Low-disorder microwave cavity lattices for quantum simulation with photons. *Physical Review A*, 86(2):023837, August 2012.

[101] D van Oosten, P van der Straten, and H Stoof. Quantum phases in an optical lattice. *Physical Review A*, 63(5):053601, April 2001.

[102] D van Oosten, P van der Straten, and H Stoof. Mott insulators in an optical lattice with high filling factors. *Physical Review A*, 67(3):033606, March 2003.

[103] A Wallraff, D I Schuster, A Blais, L Frunzio, R S Huang, J Majer, S Kumar, S M Girvin, and R J Schoelkopf. Strong coupling of a single photon to a superconducting qubit using circuit quantum electrodynamics. *Nature*, 431(7005):162–7, September 2004.

[104] K Watanabe, K Yoshida, T Aoki, and S Kohjiro. Kinetic Inductance of Superconducting Coplanar Waveguides. *Japanese Journal of Applied Physics*, 33:5708–5712, 1994.

[105] J Wenner, M Neeley, R C Bialczak, M Lenander, E Lucero, A D OConnell, D Sank, H Wang, M Weides, A N Cleland, and J M Martinis. Wirebond crosstalk and cavity modes in large chip mounts for superconducting qubits. *Superconductor Science and Technology*, 24(6):065001, June 2011.

[106] Yi Z You, Z Chen, X Qi Sun, and H Zhai. Superfluidity of Bosons in Kagome Lattices with Frustration. *Physical Review Letters*, 109(26):265302, December 2012.

[107] J Zhang, L Zhang, and W Xu. Surface plasmon polaritons: physics and applications. *Journal of Physics D: Applied Physics*, 45(11):113001, March 2012.